Distinct roles for inhibitory neuron subtypes in cortical circuits: An examination of their structure, function, and connectivity

by

Caroline A. Runyan

B.S. Neuroscience

Allegheny College, 2004

SUBMITTED TO THE DEPARTMENT OF BRAIN AND COGNITIVE SCIENCES IN PARTIAL FULFILLMENT OF THE REQUIREMENTS FOR THE DEGREE OF

DOCTOR OF PHILOSOPHY IN NEUROSCIENCE

AT THE

MASSACHUSETTS INSTITUTE OF TECHNOLOGY

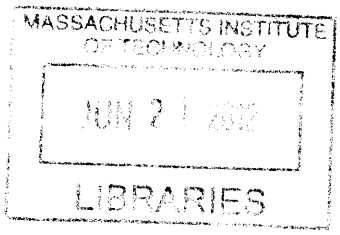

ARCHIVES

JUNE 2012

Signature of Author: _____

Department of Brain and Cognitive Sciences
April 20, 2012

Certified by: _____

Mriganka Sur, PhD
Paul E. Newton Professor of Neuroscience
Thesis Supervisor

Accepted by: _____

Earl K. Miller, PhD
Picower Professor of Neuroscience
Director, Department Graduate Program

Distinct roles for inhibitory neuron subtypes in cortical circuits: An examination of their structure, function, and connectivity

by

Caroline A. Runyan

Submitted to the Department of Brain and Cognitive Sciences on April 20, in Partial Fulfillment of the Requirements for the Degree of Doctor of Philosophy in Neuroscience

ABSTRACT

Parvalbumin-containing (PV+) neurons and somatostatin-containing (SOM+) neurons are two key cortical inhibitory cell classes that are poised to play distinct computational roles in cortical circuits: PV+ neurons form synapses on the perisomatic region near the spike initiation zone of target cells, while SOM+ neurons form synapses on distal dendrites. The goals of this thesis are to better understand the functional roles of these two cell types with four major lines of questioning. 1) When and how do PV+ and SOM+ neurons respond to visual stimuli? 2) How do inhibitory neurons obtain their response selectivity? 3) How do PV+ and SOM+ neurons affect the responses of their targets? and 4) What are the targets of PV+ and SOM+ neurons? We used Cre-lox recombination to introduce either fluorescent protein or channelrhodopsin to PV+ or SOM+ neurons, targeting these cells for two-photon targeted physiological recording and morphological reconstruction, or selectively stimulating the population of PV+ or SOM+ neurons or stimulating single PV+ or SOM+ neurons. We find diverse response properties within both groups, suggesting that further functional subclasses of PV+ and SOM+ neurons may exist. Furthermore, orientation selectivity was strongly correlated to dendritic length in PV+ neurons, whose orientation preferences matched the preferences of neighboring cells, implying that inhibitory neurons may obtain selectivity by spatially limiting their sampling of the local network. When we stimulated PV+ and SOM+ neurons, we found that they perform distinct inhibitory operations on their targets: PV+ neurons divide responses while SOM+ neurons subtract. Even single PV+ and SOM+ neurons were capable of suppressing responses of other cells in the local network, but their functional targeting was sparse and followed different rules of wiring: PV+ neurons functionally suppressed a higher percentage of cells that shared their own tuning, while SOM+ neurons seemed to target other neurons independently of their preferred orientations. By studying the response properties and functional impacts of PV+ and SOM+ neurons in the intact primary visual cortex, we have gained insight into what information these cells are carrying and how they contribute to the response properties of other cells, which apply to cortical circuits in general.

Thesis Supervisor: Mriganka Sur, PhD
Title: Paul E. Newton Professor of Neuroscience

Acknowledgments

Chris Baker, for his unwavering encouragement, support, humor, patience, and positivity – it's impossible to imagine the last six years without him. My parents, Charles and Diane, for their loving support; they always ensured I had every opportunity to pursue science and math. My brothers: Albert, John-Paul, and Simon. My huge, loving, extended family, especially my godparents Hal and Ann. My friends, especially Kaylin and Liz, and BCS 2006 classmates. The members of the Sur laboratory, past and present, particularly Travis Emery and the outstanding scientists I was lucky enough to closely collaborate with and learn from: James Schummers, Audra Van Wart, and especially Nathan Wilson, whose fresh perspective, incredible engineering skills and amazing optimism made our long experiments fun. My committee members: Chris Moore, as colleague in the field and caring mentor within the BCS program; Emery Brown, who has made himself easily available anytime I needed help with my analyses; and Ann Graybiel, whose mentorship, encouragement, and discussions have been invaluable. And last but certainly not least, my advisor Mriganka Sur, whose enthusiasm, open-mindedness, intellect, support, and true kindness enable outstanding work to go on in his laboratory everyday, and have shown me the ideal on which to model my own career.

Table of Contents

Chapter 1: Introduction

1.1 Background

Inhibitory interneurons, which are primarily local circuit neurons that release GABA upon firing, comprise roughly 30% of the neuronal population of the cerebral cortex (DeFelipe and Fariñas, 1992). Many critical roles have been proposed for inhibition in cortical circuits, falling within two general categories: (1) balancing excitation and (2) controlling the timing of spiking in other neurons. Maintaining excitation levels within the proper dynamic range for information transfer is a delicate process – runaway excitation leading to saturation of signals and even seizure must be prevented, but also excitation must not be overly suppressed so that smaller yet relevant signals do not pass through. Therefore, inhibition may be involved in setting the response threshold in its targets, determining which stimulus strengths elicit supratheshold responses (sharpening the response selectivity of target cells). Indeed, blocking $GABA_A$ receptors decreases stimulus selectivity of cells at many levels of sensory processing (Sillito, 1979; Tsumoto et al., 1979; Sato et al., 1996; Crook et al., 1997; Chen and Jen, 2000; Wang et al., 2000a; 2000b). Inhibition also maintains the proper dynamic range of activity (response gain), allowing target cells to maintain sensitivity across varying levels of drive (Katzner et al., 2011). Regarding timing, inhibition can prevent prolonged responses or precisely control the timing of spikes (Pouille and Scanziani, 2001; Berger, 2003; Pouille et al., 2009), or through rhythmic behavior synchronize the spiking within local areas or even across brain regions (Whittington et al., 1995; Whittington and Traub, 2003; Cardin et al., 2009). The results presented in this thesis are primarily related to the first category of inhibitory functions, the role of inhibition in balancing excitation.

The cortical inhibitory neuron population includes a vast diversity of cell types that vary across many dimensions, including axon targeting, dendritic span, firing pattern, and neurochemical composition (Gonchar and Burkhalter, 1997; Kawaguchi and Kondo, 2002; Markram et al., 2004; Burkhalter, 2008; Helmstaedter et al., 2009a; 2009b). For instance, inhibitory neurons that express the calcium-binding protein parvalbumin (PV) are

predominantly fast-spiking, responding to intracellular current injection with a barrage of narrow spikes (Kawaguchi and Kubota, 1997; 1998). Morphologically, they include basket cells that preferentially form synapses on the perisomatic region of their targets and chandelier cells that target synapses to the axon initial segment (Markram et al., 2004). On the other hand, inhibitory neurons that express the neuropeptide somatostatin (SOM) never express PV (Gonchar and Burkhalter, 1997; Gonchar et al., 2007; Xu et al., 2010), and include Martinotti cells and bipolar cells that target their synapses to the dendrites (Kubota et al., 1994; Kawaguchi and Kondo, 2002; McGarry et al., 2010). PV+ and SOM+ neurons can be further subdivided based on their physiological properties and their expression of other calcium binding proteins, neuropeptides, ion channel subunits, and neuromodulators and their receptors (Kubota et al., 1994; Kawaguchi and Kubota, 1996; 1997; Chow et al., 1999; Gonchar et al., 2002; Ma et al., 2006; Gonchar et al., 2007; McGarry et al., 2010). Still other subclasses can be defined that express neither PV nor SOM (Gonchar et al., 2007; Xu et al., 2010). These highly specialized subtypes have probably developed to perform unique functions.

However, in order to further our understanding of what functional roles different inhibitory cell classes might play, it is important to focus on subclasses defined in computationally relevant terms. Dendrite-targeted inhibition and soma-targeted inhibition, such as that provided by SOM+ and PV+ neurons, respectively, are likely to have unique impacts on the firing of the postsynaptic cell, as compartment-dependent distributions of GABAergic currents exist in many pyramidal cells (Connors et al., 1988; Gonchar et al., 2001), and the relative distances between the inhibitory synapses, excitatory synapses and the spike-initiation zone affect the impact of inhibition – determining whether it directly affects the efficacy of single excitatory synapses, or defines the size of the temporal window of input integration (Pouille and Scanziani, 2001; Berger, 2003; Spruston, 2008; Kanemoto et al., 2011).

The work described in this thesis attempts to determine the potential roles played by subtypes of inhibitory neurons in cortical circuits, in the context of the mouse primary visual cortex (V1). V1 is an ideal system in which to study the contributions of subtypes of neurons to computations performed by cortical circuits. It is there that orientation selectivity emerges, as the circular receptive fields encoded by thalamic inputs are

transformed to the receptive fields of V1 neurons that respond to edges of light and darkness. Each cell's characteristic orientation tuning curve, contrast response function, and spatial receptive field can be measured with a simple stimulus set, allowing for the rapid characterization of cells' response properties under normal conditions, and when inhibition is being manipulated. The mechanisms underlying the generation of orientation tuning and its contrast invariance have been hotly contested (Somers et al., 1995; Troyer et al., 1998; Ferster and Miller, 2000; Priebe and Ferster, 2008) in the several decades since they were first described by Hubel and Wiesel (1959), and it remains unclear whether inhibition plays any role in shaping response selectivity.

The mouse provides an ideal system in which to probe the properties of genetically-defined cell types, such as PV+ and SOM+ inhibitory neurons, as well as to selectively manipulate them. Cell-type-specific Cre-driver knock-in mouse lines combined with floxed viral constructs allow us to easily introduce fluorescing proteins such as red fluorescent protein (RFP) and optogenetic proteins such as channelrhodopsin-2, a light-sensitive cation channel, to any cell type that can be genetically defined in order to label it or manipulate it *in vivo* (Kuhlman and Huang, 2008; Cardin et al., 2009; Taniguchi et al., 2011). Such tools are not yet readily available in animal models that have been more traditionally used in visual neuroscience, and the mouse had been historically ignored by the field, being commonly assumed to be inferior due to its lack of well-defined functional maps of orientation preference in V1 (Ohki and Reid, 2007). However, although mice have lower visual acuity, neurons in mouse V1 develop orientation selectivity rivaling that of the cat and primate (Niell and Stryker, 2008), and thus the mechanisms underlying the generation of orientation selectivity may be the same.

All of the experiments in this thesis rely on the genetic capabilities of the mouse model, that have only recently allowed the targeted recording of genetically defined cell classes. In Chapters 2-3, PV+ and SOM+ neurons in mouse V1 are genetically labeled with RFP, and two-photon imaging is used to target these cell classes for cell-attached recordings or calcium imaging. Cell-attached recordings are used for high quality single cell response characterization, while calcium imaging is used to spatially relate the response properties of labeled inhibitory neurons and neighboring neurons. In Chapters 4-

5, ChR2 is expressed in PV+ or SOM+ neurons, allowing us to use a blue laser to optically control the firing of these neurons, while measuring the impacts on nearby cells.

1.2 Organization of thesis

In chapter 2, the response properties of two subtypes of inhibitory neurons, soma-targeting PV+ neurons and dendrite-targeting SOM+ neurons, are described. Both cell types show a range of tuning properties. PV+ cells can be either highly selective or broadly tuned for orientation, suggesting that further functional subclasses of PV+ neurons exist, while SOM+ neurons tend to be more highly selective for orientation, but to respond with a delay at lower firing rates. In chapter 3, the relationship between the response selectivity of PV+ neurons and their dendritic morphology is described, giving clues as to how inhibitory neurons may obtain their response properties. Highly tuned PV+ neurons have shorter, less tortuous dendritic processes, while untuned PV+ neurons have longer dendrites, though not wider dendritic fields. Furthermore, tuned PV+ neurons tend to share the orientation preference of the nearest neighboring cells, suggesting that these cells could obtain selectivity by spatially restricting the number of inputs they receive. In chapter 4, PV+ and SOM+ neurons are selectively activated, while measuring the effects on the visual processing of neighboring V1 neurons. The results show that PV+ soma-targeting inhibition divisively normalizes responses of target cells, while SOM+ dendrite-targeting inhibition subtracts responses. In chapter 5, single PV+ or SOM+ inhibitory neurons are activated while monitoring the activity of neighboring cells. These experiments suggest that PV+ and SOM+ neurons may select specific synaptic targets rather than blanketing neighboring cells with uniform inhibition. In chapter 6, the findings of the preceding chapters are integrated and discussed.

1.3 References

Berger T (2003) Timing and Precision of Spike Initiation in Layer V Pyramidal Cells of the Rat Somatosensory Cortex. Cerebral Cortex 13:274–281.

Burkhalter A (2008) Many specialists for suppressing cortical excitation. Front Neurosci

2:155–167.
Cardin JA, Carlén M, Meletis K, Knoblich U, Zhang F, Deisseroth K, Tsai L-H, Moore CI (2009) Driving fast-spiking cells induces gamma rhythm and controls sensory responses. Nature 459:663–667.
Chen QC, Jen PH (2000) Bicuculline application affects discharge patterns, rate-intensity functions, and frequency tuning characteristics of bat auditory cortical neurons. Hear Res 150:161–174.
Chow A, Erisir A, Farb C, Nadal MS, Ozaita A, Lau D, Welker E, Rudy B (1999) K(+) channel expression distinguishes subpopulations of parvalbumin- and somatostatin-containing neocortical interneurons. J Neurosci 19:9332–9345.
Connors BW, Malenka RC, Silva LR (1988) Two inhibitory postsynaptic potentials, and GABAA and GABAB receptor-mediated responses in neocortex of rat and cat. J Physiol (Lond) 406:443–468.
Crook JM, Kisvárday ZF, Eysel UT (1997) GABA-induced inactivation of functionally characterized sites in cat striate cortex: effects on orientation tuning and direction selectivity. Visual Neuroscience 14:141–158.
DeFelipe J, Fariñas I (1992) The pyramidal neuron of the cerebral cortex: morphological and chemical characteristics of the synaptic inputs. Prog Neurobiol 39:563–607.
Ferster D, Miller KD (2000) Neural mechanisms of orientation selectivity in the visual cortex. Annu Rev Neurosci 23:441–471.
Gonchar Y, Burkhalter A (1997) Three distinct families of GABAergic neurons in rat visual cortex. Cereb Cortex 7:347–358.
Gonchar Y, Pang L, Malitschek B, Bettler B, Burkhalter A (2001) Subcellular localization of GABA(B) receptor subunits in rat visual cortex. J Comp Neurol 431:182–197.
Gonchar Y, Turney S, Price JL, Burkhalter A (2002) Axo-axonic synapses formed by somatostatin-expressing GABAergic neurons in rat and monkey visual cortex. J Comp Neurol 443:1–14.
Gonchar Y, Wang Q, Burkhalter A (2007) Multiple distinct subtypes of GABAergic neurons in mouse visual cortex identified by triple immunostaining. Frontiers in neuroanatomy 1:3.
Helmstaedter M, Sakmann B, Feldmeyer D (2009a) L2/3 interneuron groups defined by multiparameter analysis of axonal projection, dendritic geometry, and electrical excitability. Cereb Cortex 19:951–962.
Helmstaedter M, Sakmann B, Feldmeyer D (2009b) The relation between dendritic geometry, electrical excitability, and axonal projections of L2/3 interneurons in rat barrel cortex. Cereb Cortex 19:938–950.
Hubel DH, Wiesel TN (1959) Receptive fields of single neurones in the cat's striate cortex. J Physiol (Lond) 148:574–591.
Kanemoto Y, Matsuzaki M, Morita S, Hayama T, Noguchi J, Senda N, Momotake A, Arai T, Kasai H (2011) Spatial Distributions of GABA Receptors and Local Inhibition of Ca2+ Transients Studied with GABA Uncaging in the Dendrites of CA1 Pyramidal Neurons Tell F, ed. PLoS ONE 6:e22652.
Katzner S, Busse L, Carandini M (2011) GABAA Inhibition Controls Response Gain in Visual Cortex. J Neurosci 31:5931–5941.
Kawaguchi Y, Kondo S (2002) Parvalbumin, somatostatin and cholecystokinin as chemical markers for specific GABAergic interneuron types in the rat frontal cortex. J Neurocytol

31:277–287.
Kawaguchi Y, Kubota Y (1996) Physiological and morphological identification of somatostatin- or vasoactive intestinal polypeptide-containing cells among GABAergic cell subtypes in rat frontal cortex. J Neurosci 16:2701–2715.
Kawaguchi Y, Kubota Y (1997) GABAergic cell subtypes and their synaptic connections in rat frontal cortex. Cereb Cortex 7:476–486.
Kawaguchi Y, Kubota Y (1998) Neurochemical features and synaptic connections of large physiologically-identified GABAergic cells in the rat frontal cortex. Neuroscience 85:677–701.
Kubota Y, Hattori R, Yui Y (1994) Three distinct subpopulations of GABAergic neurons in rat frontal agranular cortex. Brain Res 649:159–173.
Kuhlman SJ, Huang ZJ (2008) High-resolution labeling and functional manipulation of specific neuron types in mouse brain by Cre-activated viral gene expression. PLoS ONE 3:e2005.
Ma Y, Hu H, Berrebi AS, Mathers PH, Agmon A (2006) Distinct subtypes of somatostatin-containing neocortical interneurons revealed in transgenic mice. J Neurosci 26:5069–5082.
Markram H, Toledo-Rodriguez M, Wang Y, Gupta A, Silberberg G, Wu C (2004) Interneurons of the neocortical inhibitory system. Nat Rev Neurosci 5:793–807.
McGarry LM, Packer AM, Fino E, Nikolenko V, Sippy T, Yuste R (2010) Quantitative classification of somatostatin-positive neocortical interneurons identifies three interneuron subtypes. Front Neural Circuits 4:12.
Niell CM, Stryker MP (2008) Highly Selective Receptive Fields in Mouse Visual Cortex. J Neurosci 28:7520–7536.
Ohki K, Reid RC (2007) Specificity and randomness in the visual cortex. Curr Opin Neurobiol 17:401–407.
Pouille F, Marin-Burgin A, Adesnik H, Atallah BV, Scanziani M (2009) Input normalization by global feedforward inhibition expands cortical dynamic range. Nat Neurosci 12:1577–1585.
Pouille F, Scanziani M (2001) Enforcement of temporal fidelity in pyramidal cells by somatic feed-forward inhibition. Science 293:1159–1163.
Priebe NJ, Ferster D (2008) Inhibition, spike threshold, and stimulus selectivity in primary visual cortex. Neuron 57:482–497.
Sato H, Katsuyama N, Tamura H, Hata Y, Tsumoto T (1996) Mechanisms underlying orientation selectivity of neurons in the primary visual cortex of the macaque. J Physiol (Lond) 494 (Pt 3):757–771.
Sillito AM (1979) Inhibitory mechanisms influencing complex cell orientation selectivity and their modification at high resting discharge levels. J Physiol (Lond) 289:33–53.
Somers DC, Nelson SB, Sur M (1995) An emergent model of orientation selectivity in cat visual cortical simple cells. J Neurosci 15:5448–5465.
Spruston N (2008) Pyramidal neurons: dendritic structure and synaptic integration. Nat Rev Neurosci 9:206–221.
Taniguchi H, He M, Wu P, Kim S, Paik R, Sugino K, Kvitsani D, Fu Y, Lu J, Lin Y, Miyoshi G, Shima Y, Fishell G, Nelson SB, Huang ZJ (2011) A Resource of Cre Driver Lines for Genetic Targeting of GABAergic Neurons in Cerebral Cortex. Neuron 71:995–1013.
Troyer TW, Krukowski AE, Priebe NJ, Miller KD (1998) Contrast-invariant orientation

tuning in cat visual cortex: thalamocortical input tuning and correlation-based intracortical connectivity. J Neurosci 18:5908–5927.
Tsumoto T, Eckart W, Creutzfeldt OD (1979) Modification of orientation sensitivity of cat visual cortex neurons by removal of GABA-mediated inhibition. Exp Brain Res 34:351–363.
Wang J, Caspary D, Salvi RJ (2000a) GABA-A antagonist causes dramatic expansion of tuning in primary auditory cortex. Neuroreport 11:1137–1140.
Wang Y, Fujita I, Murayama Y (2000b) Neuronal mechanisms of selectivity for object features revealed by blocking inhibition in inferotemporal cortex. Nature Publishing Group 3:807–813.
Whittington MA, Traub RD (2003) Interneuron diversity series: inhibitory interneurons and network oscillations in vitro. Trends Neurosci 26:676–682.
Whittington MA, Traub RD, Jefferys JG (1995) Synchronized oscillations in interneuron networks driven by metabotropic glutamate receptor activation. Nature 373:612–615.
Xu X, Roby KD, Callaway EM (2010) Immunochemical characterization of inhibitory mouse cortical neurons: three chemically distinct classes of inhibitory cells. J Comp Neurol 518:389–404.

Chapter 2: Response features of parvalbumin-expressing and somatostatin-expressing interneurons suggest precise roles for subtypes of inhibition in visual cortex.[1]

2.1 Summary

Inhibitory interneurons in the cerebral cortex include a vast array of subtypes, varying in their molecular signatures, electrophysiological properties, and connectivity patterns. This diversity suggests that individual inhibitory classes have unique roles in cortical circuits; however, their characterization to date has been limited to broad classifications including many subtypes. We used the Cre/LoxP system, specifically labeling parvalbumin (PV) or somatostatin (SOM) expressing interneurons in visual cortex of PV-Cre or SOM-Cre mice with red fluorescent protein (RFP), followed by targeted cell-attached recordings and two-photon imaging of calcium responses *in vivo* to characterize the visual receptive field properties of these cells. Despite their relative molecular and morphological homogeneity, we find that PV+ neurons have a diversity of feature-specific visual responses that include sharp orientation and direction-selectivity, small receptive fields, and bandpass spatial frequency tuning. SOM+ neurons had weak and delayed but highly selective visual responses. These results suggest that subsets of parvalbumin and somatostatin interneurons are components of specific cortical networks, and that perisomatic inhibition contributes to the generation of precise response properties.

2.2 Introduction

The balance between excitation and inhibition is critical for normal brain development and function. Indeed, disruptions in this balance are associated with a variety of brain disorders, including autism and schizophrenia (Rubenstein and Merzenich, 2003; Hensch, 2005; Lewis et al., 2005). Intracortical inhibition is thought to be important not only for

[1] The bulk of the findings presented in this chapter appeared in Runyan et al., 2010

maintaining an appropriate dynamic range of cortical excitation, but also for shaping the response properties of cells and circuits in sensory cortices (Ferster and Miller, 2000; Monier et al., 2003; Wehr and Zador, 2003; Zhang et al., 2003; Mariño et al., 2005; Poo and Isaacson, 2009). The precise ways in which this is achieved remain unclear, however.

The elucidation of the roles for inhibition in cortical function is complicated by the vast diversity of inhibitory cell types. These cells can be distinguished based on their electrophysiological profiles, their morphologies, and their molecular signatures, suggesting that individual inhibitory cell classes may provide specific forms of inhibition and thus subserve unique functions (Markram et al., 2004; Burkhalter, 2008). For instance, the axons of some inhibitory neuron subtypes, such as calretinin- and somatostatin-positive cells, preferentially target neuron dendrites, while axons of others, such as parvalbumin-positive (PV+) basket cells and chandelier cells target the soma and axon initial segment, respectively (Kisvárday and Eysel, 1993; DeFelipe, 1997; DeFelipe et al., 1999; Markram et al., 2004). PV+ cells thus represent a distinct morphological subclass of inhibitory neurons, which are in an ideal position to efficiently suppress the output of their synaptic partners, while dendrite-targeting cells may have more subtle effects on neuronal responses and computations. Based on their wide dendritic geometry and extensive lateral axonal arbors (Kisvárday and Eysel, 1993; Wang et al., 2002; Stepanyants et al., 2009), and role in driving cortical synchrony (Cardin et al., 2009), a reasonable hypothesis is that PV+ cells have large integration fields resulting in relatively unselective responses that act generally to balance excitation. In contrast, based on their radial geometry and intracolumnar connectivity, dendrite-targeting somatostatin-positive (SOM+) interneurons may have small integration fields with feature-selective responses.

An ideal system for dissecting cell-specific roles in cortical information processing is the primary visual cortex (V1), where clear signatures of circuitry such as orientation and spatial frequency tuning arise and can be used to probe the function of specific cell types *in vivo*. A number of studies have addressed the general role of inhibition in orientation tuning, by either measuring the net inhibition impinging on excitatory cells (Ferster, 1986; Ferster et al., 1996; Anderson et al., 2000; Monier et al., 2003; Mariño et al., 2005), or by manipulating inhibition pharmacologically (Sillito, 1975; Nelson et al., 1994), or electrically (Ferster et al., 1996; Chung and Ferster, 1998). However, to unravel the precise

contributions of inhibitory interneurons and understand the specific roles played by different inhibitory cell types, direct measurement of the tuning properties of each cell type is necessary.

Physiologically identified fast-spiking cells or genetically identified inhibitory interneurons have been characterized in the visual cortex of cats, rabbits, and rodents, but direct measurements of the receptive field selectivity of presumed or confirmed inhibitory neurons have yielded somewhat conflicting results (Hirsch et al., 2003; Swadlow, 2003; Cardin et al., 2007; Sohya et al., 2007; Niell and Stryker, 2008; Nowak et al., 2008; Liu et al., 2009a; Kerlin et al., 2010; Ma et al., 2010; Runyan et al., 2010; Zariwala et al., 2011). Importantly, although fast-spiking behavior has been closely associated with PV+ inhibitory interneurons, the relationship is not one-to-one. Fast-spiking cells can also be somatostatin-positive (SOM+) and PV-, and can include a diverse array of morphologies (Markram et al., 2004; Burkhalter, 2008). Likewise, not all PV+ neurons are fast-spiking (Blatow et al., 2003). Furthermore, excitatory fast-spiking cells have been reported in sensory cortex (Dykes et al., 1988; Gray and Mccormick, 1996), so that the precise nature of blindly recorded cell types often remains unclear. Thus, more definitive experimental approaches were needed to characterize the physiological properties of specific cell classes.

Several recent studies, using knock-in mice expressing the GAD67-GFP (Δneo) transgene, have characterized the orientation tuning of inhibitory neurons (Sohya et al., 2007), and inhibitory neurons subclassified electrophysiologically into fast-spiking and regular-spiking inhibitory neurons (Liu et al., 2009a), or immunohistochemically into PV, SOM or vasoactive intestinal peptide (VIP) containing neurons (Kerlin et al., 2010). These studies found that inhibitory cells of all subtypes are broadly tuned for orientation, contradicting the findings of many studies in higher mammals (Hirsch et al., 2003; Cardin et al., 2007; Nowak et al., 2008), as well as more recent studies using other genetic methods to target inhibitory subtypes for recordings in mice (Ma et al., 2010; Runyan et al., 2010; Zariwala et al., 2011), which have shown the existence of inhibitory neurons that are as sharply tuned as excitatory neurons. Importantly, the GAD67-GFP (Δneo) knock-in mice develop with significant deficits in GABA production (Tamamaki et al., 2003), which is known to affect inhibitory circuitry (Chattopadhyaya et al., 2007). These unexpected

findings thus need to be verified in mice with wild-type inhibitory circuitry, where the properties of subclasses of inhibitory neurons would be more faithfully expressed, before it is concluded that the properties of inhibitory neurons are different between mice and higher mammals.

We have used recently developed genetic-labeling techniques combined with *in vivo* two-photon guided cell-attached recording and calcium imaging to reveal the visual response properties of the PV+ soma/axon-targeting inhibitory neurons in layers 2/3 of visual cortex. Our measurements demonstrate that PV+ interneurons have a range of response features, and include a significant proportion of cells with precisely tuned responses, small receptive fields and bandpass spatial frequency tuning characteristics. We suggest that these cells are components of, and contributors to, highly specific networks that shape the selectivity of neuronal responses. Furthermore, we have compared the orientation selectivity and response latency of PV+ and SOM+ subtypes, finding that SOM+ neuron responses are weak and delayed, but that both cell types include highly tuned neurons.

2.3 Experimental Procedures

2.3.1 Mice

Experiments were carried out in mice under protocols approved by MIT's Animal Care and Use Committee and conformed to NIH guidelines. Heterozygous PV-Cre knock-in driver mice, which express Cre in over 90% of PV+ neurons, and SOM-Cre knock-in mice were backcrossed into a C57BL/6 line (Hippenmeyer et al., 2005; Taniguchi et al., 2011). Mice heterozygous for the GAD67-GFP (Δneo) allele (Tamamaki et al., 2003) were maintained on a C57BL/6 background; only mice older than 8 weeks were used.

2.3.2 Viral Construct and Injection

RFP was expressed specifically in Parvalbumin+ (PV+) or Somatostatin+ (SOM+) interneurons in the visual cortex of PV-Cre or SOM-Cre mice by infection of the viral

construct shown in Figure 2.1A. The LS_2L-RFP construct (Figure 2.1A) was packaged into adeno-associated virus (AAV, serotype 2/9) as described previously (Kuhlman and Huang, 2008). Six-week old PV-Cre mice were initially anesthetized with 4% isoflurane in oxygen, and maintained on 2% isoflurane. The skull was thinned along a 1mm line at the rostral edge of V1, and the remaining skull and dura were carefully punctured using a glass micropipette filled with the virus. Two injections were made at each site, one at 500μm below the cortical surface, and one at a depth of 250μm. A volume of 0.25μl of virus was injected at 10μl/min at each depth. After each injection, the pipette was held in place for five minutes prior to retraction to prevent leakage.

2.3.3 Animal Preparation

Two weeks post-injection, mice were anesthetized with a cocktail containing Fentanyl (0.05mg/kg), Midazolam (5mg/kg), and Medetomidine (0.5mg/kg), supplemented with isoflurane. The eyes were protected with ophthalmic ointment during the surgery, and moistened afterward with saline. A metal headplate was attached to the skull using superglue and dental acrylic, and a 2mm x 2mm craniotomy was performed over the primary visual cortex region (area 17). The exposed area was then covered with a thin layer of 2% agarose in ACSF (140mM NaCl, 5mM KCl, 2mM $CaCl_2$, 1mM $MgCl_2$, .01mM EDTA, 10mM HEPES, 10mM Glucose, pH 7.4).

Mice were then transferred to a custom-built two-photon microscope (Majewska et al., 2000), where the headplate was screwed into a moveable stage, and 0.5% isoflurane in oxygen was supplied through a tube, and Fentanyl/Medetomidine was injected every hour. The body temperature was maintained at 37.5ºC with heating pads. The recording phase of physiology experiments typically lasted for 4-6 hours in calcium imaging experiments, and 8-12 hours in electrophysiology experiments.

2.3.4 Two-photon Microscopy

The microscope was made from a modified Fluoview confocal scanhead (Olympus Optical) and a titanium/sapphire laser providing 100fs pulses at 80MHz (Tsunami; Spectra-Physics, Menlo Park, CA) pumped by a 10W solid-state source (Millenia; Spectra-

Physics). Emitted fluorescence was detected using photomultiplier tubes (HC125-02; Hamamatsu, Shizouka, Japan). Imaging was performed through a 20x, 0.95 NA lens (IR2, Olympus Optical) using Fluoview software. We collected images at a 1Hz frame-rate, at depths between 130 and 300μm below the cortical surface.

2.3.5 Targeted Cell-attached Recording

Glass pipettes with ~1.5μm tip size and 3-7MΩ resistance were filled with Alexa Fluor 488 (5μM, in saline, Molecular Probes, Eugene, OR) and introduced to the pia above the viral injection site at a 21-degree angle using a micromanipulator (Sutter, MP-285) under visual guidance with epifluorescence. Upon entering the brain, the pipette was guided toward RFP+ cells in superficial layer 2/3 of primary visual cortex under two-photon guidance. The laser was tuned to 920nm, which allowed excitation of both the Alexa 488 and RFP fluorophores simultaneously. The pipette was targeted to RFP+ cells while applying constant positive pressure (0.2 psi), which was monitored with a digital pressure gauge (General Tools). When the pipette was just touching the cell surface, positive pressure was released, and sustained negative pressure immediately applied (0.2-0.6 psi) to obtain a loose seal (Joshi and Hawken, 2006). If well-isolated spikes were detected during the display of a drifting grating that randomly changed orientation and direction at 8 Hz, then the cell's receptive field was assessed. Subsequently, current pulses (35 ms, 900-2000 nA) were delivered at 15 Hz for 30-60 seconds to fill the recorded cell. Only RFP+ cells that were distinctly filled during this procedure were included for analysis. In the same experiments, RFP- cells were targeted blindly. As the tip was slowly advanced through the cortex, -0.5 nA current pulses were delivered for 6.3 ms at .55 Hz, and the tip resistance was monitored. When the tip resistance increased substantially, positive pressure was released, and negative pressure immediately applied, as above. The location of the tip was still monitored under two-photon guidance; all RFP- cells were located within the injection site and were filled after recording. Recordings from GFP+ and GFP- neurons in GAD67-GFP mice were carried out similarly. Recordings were made with an Axoclamp-2A amplifier (Axon Instruments) using Clampex software (Axon Instruments, v8.1) at a sampling rate of 30 KHz and filtered between 300 Hz and 10 KHz.

2.3.6 Calcium Imaging

A glass pipette filled with Oregon Green Bapta-1 AM (OGB1-AM, 1.0mM, Molecular Probes, Eugene, OR) and Alexa Fluor 594 (100μM, Molecular Probes, Eugene, OR) was visually guided into the brain and lowered to a depth between 100 and 200μm below the pial surface, and a small amount of dye was released using a picospritzer. The laser was tuned to 810nm, and one hour later, fluorescence changes in response to visual stimulation were monitored.

2.3.7 Visual Stimulation

Visual stimuli were displayed on a 17-inch LCD monitor placed 15cm from the eyes. Stimuli were generated in Matlab (Mathworks, Natick, MA) using the PsychoPhysics Toolbox (Brainard, 1997). Square wave drifting gratings with 100% contrast were used to test orientation, direction and spatial frequency tuning. Test stimuli were episodically presented, equally alternating with a blank gray screen with 8 or 16 second cycles. For calcium imaging experiments, orientation and direction selectivity was measured with oriented gratings presented at a spatial frequency of 0.05 cycles per degree (cpd), and a temporal frequency of 3 cycles per second (cps). Spatial frequency selectivity was measured at several random orientations (changing at 4Hz) and temporal frequency of 3 cps. For cell-attached recordings, attempts were made to optimize the spatial frequency and temporal frequency parameters of the oriented gratings for each cell's preference, ranging in spatial frequency from 0.01 to 0.05 cpd and in temporal frequency from 1 to 3 cps. Receptive field locations were determined with vertical and horizontal bars that drifted periodically across the screen at 18-second intervals; each bar was 5.1 degrees wide, moved in steps of 1.7 degrees, and contained a checkerboard pattern of white and black squares that reversed sign at 10Hz.

2.3.8 Data Analysis

Analysis of electrophysiological data was carried out with custom-written Matlab scripts. Time traces were imported into Matlab, smoothed with a Gaussian kernel, and spikes were detected offline with custom routines. Spikes were identified by detection of events based on the derivative of the voltage traces. The spontaneous firing rate of each

neuron was measured for 10 seconds preceding visual stimulation for each trial. A neuron was considered visually responsive if its firing rate at the preferred orientation was significantly higher than its spontaneous firing rate, determined with a t-test. The spontaneous firing rate was then subtracted from the response to each orientation, the mean firing rate across the entire 4-second stimulus interval.

Calcium imaging data were also imported into Matlab, where the change in fluorescence from baseline was calculated for each pixel. First, the unstimulated PMT fluorescence intensity was subtracted from the image series, the fluorescence time series was smoothed with a Gaussian kernel, and the change in fluorescence normalized by the baseline fluorescence ($\Delta F/F$) was calculated for each pixel. The baseline fluorescence was defined as the pixel's fluorescence intensity during the previous blank frame, so that the $\Delta F/F$ for a particular trial was equal to the mean fluorescence intensity during the stimulus presentation minus the baseline, divided by the baseline. This method is thus insensitive to changes in baseline fluorescence intensity that may occur through the course of a particular experiment. For receptive field mapping, stimuli were not episodically presented, and a fixed percentile of fluorescence intensity rather than the baseline intensity was subtracted. Individual neurons were circled manually, and astrocytes were not included. Astrocytes can be easily recognized from neurons in calcium images by their bright, irregular cell bodies, which we have confirmed in other experiments by labeling with the marker Sulforhodamine 101 (data not shown). The ΔF of the surrounding neuropil was subtracted from the ΔF of each neuron. The $\Delta F/F$ was then calculated as the mean $\Delta F/F$ within each neuron. Only neurons that were visually responsive, defined as having response values above the surrounding neuropil response for at least 50% of trials, were further considered.

The responses, firing rates or $\Delta F/F$, were then fit to Gaussian functions (orientation, receptive field size) or a Difference of Gaussians (DOG, spatial frequency). Two measures of orientation selectivity were used: the orientation selectivity index (OSI) was calculated from the $\Delta F/F$ responses or firing rates as the vector average in the preferred direction, and the tuning width was taken as the half-width at half-height from the Gaussian fit (untuned cells that could not be fit with a Gaussian were assigned tuning widths of 90 degrees). The direction selectivity index (DSI) was also calculated from the Gaussian fit as

the difference of the response amplitude in each direction of the preferred orientation, divided by their sum. The half-width at half-height of the receptive field Gaussian was used as a measure of receptive field size. Finally, the preferred spatial frequency and spatial frequency tuning bandwidth were determined from the DOG function. The bandwidth was defined as the ratio of spatial frequencies yielding the half-maximal response (Niell and Stryker, 2008). The inverse Fourier transform of the excitatory and inhibitory components of the DOG then provided an estimate of the relationship between the center excitation and surround inhibition, as shown in the supplementary information (Enroth-Cugell and Robson, 1966, 1984; Shapley and Lennie, 1985).

Statistical comparisons were carried out using the Wilcoxon test, two-tailed t-test, and the Kolmogorov-Smirnoff test and yielded indistinguishable results. Values from the Wilcoxon test are reported under Results.

2.3.9 Immunohistochemistry

Immediately after physiology experiments were completed, mice were overdosed with pentobarbitol, and perfused transcardially with saline followed by 4% paraformaldehyde. The brains were then postfixed in 4% paraformaldehyde, cryoprotected in 30% sucrose, and 40μm sections were thaw-mounted and then immunostained for PV or GABA. Sections were blocked in 10% normal goat serum with 0.1% triton in PBS for 1 hour, incubated overnight in either mouse anti-PV (1:250, Chemicon, MAB1572), or guinea pig anti-GABA (1:250, Millipore, AB175), then incubated in Alexa Fluor 633 goat anti-mouse or Alexa Fluor 488 goat anti-guinea-pig (1:200, Molecular Probes, A21052, A11073), and coverslipped with Vectashield Hardset mounting media with DAPI (Vector Labs). Using a confocal microscope (Zeiss LSM 5 Pascal Exciter), z-stacks were obtained through the extent of RFP-labeled cells on sections that had been stained for PV or GABA respectively and these cells were then analyzed for colocalization with either marker. Counts of RFP+/PV+, RFP+/PV-, RFP-/PV+, RFP+/GABA+, RFP+/GABA-, and RFP-/GABA+ cells were made from these image stacks using ImageJ software (National Institutes of Health).

2.4 Results

In order to better understand the role of inhibition provided by PV+ cells in visual cortical circuits, we characterized their visual response properties, including orientation and direction tuning, spatial frequency tuning, and receptive field size. We accomplished this by specifically expressing red fluorescent protein (RFP) in PV+ cells and then performing *in vivo* two-photon-guided cell-attached recordings, and in parallel experiments, two-photon imaging of calcium responses. We then compared the orientation selectivity of PV+ and SOM+ neurons.

2.4.1 Neurons labeled with RFP are PV+ GABAergic interneurons

We used the Cre/loxP system to selectively label PV+ cells with RFP (Kuhlman and Huang, 2008), by injecting an adenoassociated virus (serotype 2/9) containing a loxpSTOPloxp-RFP construct (Figure 2.1A) into the primary visual cortex (V1) of PV-Cre knock-in mice (Hippenmeyer et al., 2005). To examine the specificity of RFP expression to the PV+ inhibitory population, we perfused the mice and harvested their brains, staining alternate sections for PV or GABA after *in vivo* functional imaging. Immunostains for PV and GABA (Figure 2.1B,C) demonstrated qualitatively that RFP+ cells are PV+ and GABA+ (though all PV+ cells need not be RFP+, particularly away from the center of the RFP labeled zone). Quantitative analysis of z-stacks of confocal images, through 453 RFP+ cells on sections that had been stained for PV, and 434 RFP+ cells on sections that had been stained for GABA, showed that 97.7% of RFP+ cells were PV+, and 97.9% of RFP+ cells were GABA+. Overall, up to 10% of GABA+ cells at the center of the viral injection site in PV-Cre mice were RFP+, a proportion consistent with estimates of PV+ interneurons in the cerebral cortex (Markram et al., 2004). In addition, we injected the virus into wild-type mice and did not observe RFP+ cells two weeks later, either *in vivo* or histologically (data not shown). Thus, RFP+ neurons targeted for *in vivo* recordings are PV+ GABAergic interneurons.

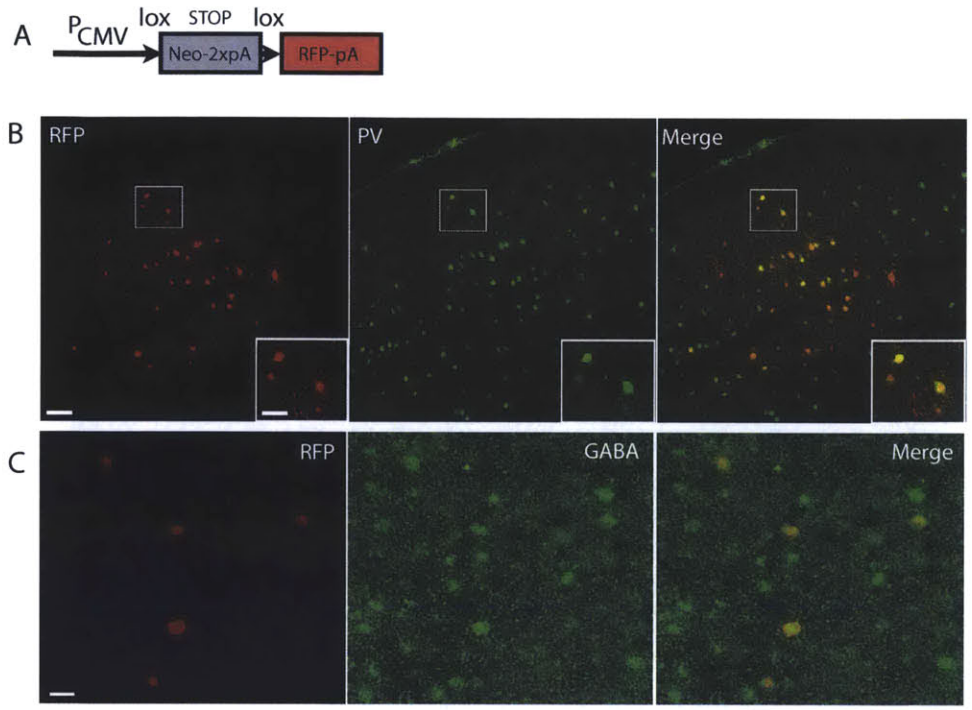

Figure 2.1. Specific labeling of PV+ inhibitory interneurons in visual cortex of PV-Cre mice. (A) The viral construct contained a floxed-STOP codon followed by RFP under control of the CMV promoter (Kuhlman and Huang, 2008). (B, C) Immunohistochemical verification of RFP expression. Sections containing virally-infected cells were immunostained for either (B) PV, or (C) GABA. Virtually all RFP+ cells were both PV+ and GABA+. Inset in (B) and images in (C) were taken from the depth at which in vivo recordings were performed (~130-300μm). Scalebars: (B) 100μm, inset: 50μm, (C) 25μm.

2.4.2 Orientation and direction selectivity of RFP+ and RFP- neurons is similar

A large proportion of PV+ neurons includes large basket cells, whose axonal arbors can stretch across many cortical layers and across multiple cortical columns, and preferentially innervate the somata of their targets (Kisvárday and Eysel, 1993; Gupta et al., 2000; Wang et al., 2002). Because of this wide-reaching geometry and soma-targeting output, we expected them to have broadly tuned responses and large receptive fields. However, we were surprised to find a diversity of orientation tuning characteristics in these cells, ranging from cells that responded to a broad range of orientations to others with highly selective responses, that responded only to one orientation (Figure 2.2).

2.4.2.1 Cell-attached Recordings

Under two-photon guidance, we targeted a dye-filled patch pipette to RFP+ and RFP- neurons. After characterizing the receptive field of each neuron, we ensured the identity of the recorded neuron by filling the cell (i.e., its soma and proximal dendrites) at the end of recording. Only RFP+ cells that were successfully and unambiguously filled (Figure 2.2A) were included in this study.

We recorded from 74 visually responsive RFP+ neurons and 34 visually responsive RFP- neurons in 27 PV-Cre mice. The spike shapes of the RFP+ and RFP- neurons were highly distinguishable (Figure 2.2B); the RFP+ neurons had narrower spike widths (RFP+: 3.0msec $\pm$ 0.018 s.d.; RFP-: 3.3msec $\pm$ 0.011 s.d.; $p < 0.05$, two-tailed two-sample t-test here and below), smaller peak:valley amplitudes (RFP+: 7.91 $\pm$ 16.81; RFP-: 21.52 $\pm$ 20.08; $p < 0.05$), and a nonsignificant trend toward sharper repolarization rates (RFP+: 107.27V/sec $\pm$ 69.39; RFP-: 105.45V/sec $\pm$ 75.45, $p = 0.76$) (see Figure 2.2C). The spontaneous firing rate was higher in the RFP+ PV+ neurons (RFP+: 1.3Hz $\pm$ 2.2; RFP-: 0.4Hz $\pm$ 0.9; $p<0.05$), and there was a nonsignificant trend toward higher evoked firing rates in RFP+ PV+ neurons (RFP+: 7.5Hz $\pm$ 7.5; RFP-: 5.3 $\pm$ 8.1; $p = 0.13$).

Although the spike shapes of the RFP+ neurons are on average different from those of the RFP- neurons, the variability in these waveform characteristics (Figure 2.2C) suggest that PV+ cells are a somewhat diverse electrophysiological population, and possibly include multiple functional subtypes. The measures that best distinguished RFP+ and RFP- cells,

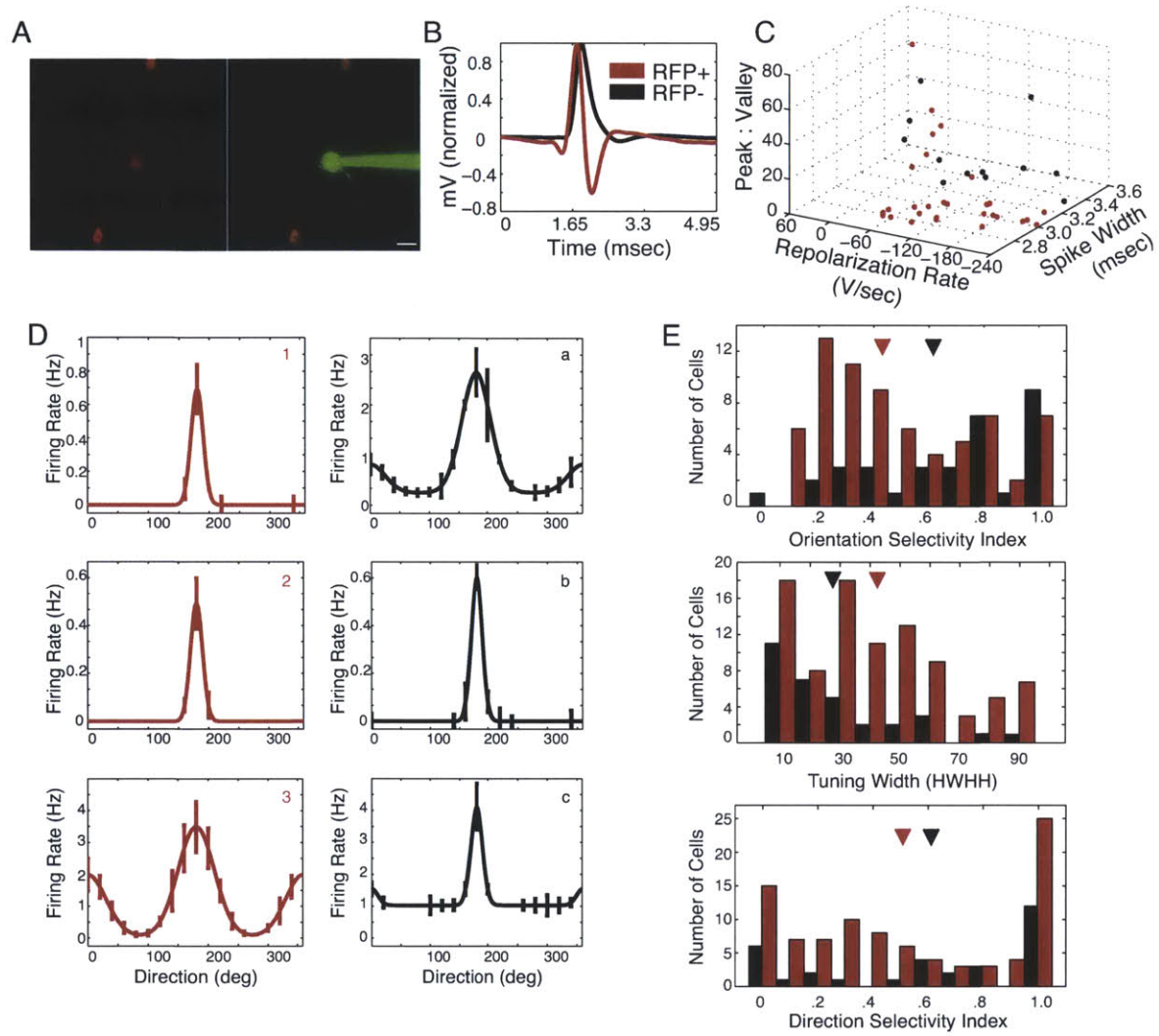

Figure 2.2. Two-photon guided cell-attached recordings of PV+ interneurons reveal sharp orientation tuning in a subset of PV+ neurons. (A) RFP+ cells (red) were targeted with a patch pipette containing Alexa 488 dye (green). After the visual responses of each neuron were characterized, the cell was filled to confirm its identity. (B) The spikes recorded from RFP+ neurons and RFP- neurons were averaged and normalized by their maximum voltage. Spikes recorded from the RFP+ neurons show the characteristic shape of fast-spiking PV+ neurons. (C) The spike shapes of RFP+ neurons and RFP- neurons are distinct. The ratio of peak amplitude and valley amplitude ($p<.05$), repolarization rate ($p>.1$), and spike width ($p<.01$) are plotted for RFP+ and RFP- neurons. (D) Examples of orientation tuning curves from three RFP+ and three RFP- cells. The preferred direction was set to 180 degrees for ease of comparison of the tuning among cells. (1) OSI = 1.0, tuning width = 15.8 deg, DSI = 0.8. (2) OSI = 1.0, tuning width = 16.7 deg, DSI = 0.9. (3) OSI = 0.7, tuning width = 30.1 deg, DSI = 0.6. (a) OSI = 0.8, tuning width = 15.0 deg, DSI = 0.7. (b) OSI = 0.8, tuning width = 16.2 deg, DSI = 0.7. (c) OSI = 0.6, tuning width = 10.0 deg, DSI = 0.6. Error bars indicate SEM. (E) Population histograms of the OSI, tuning width, and DSI of RFP+ (red) and RFP- (black) cells. Arrowheads indicate the population means.

the spike width, repolarization rate and the peak:valley amplitude, probably reflect the strong colocalization of the Kv3.1 and PV proteins (Chow et al., 1999). The overlap between spike shape measures may additionally reflect the known diversity in expression of potassium channel subtypes in PV+ cells (Chow et al., 1999).

We used two separate measures, the orientation selectivity index (OSI) and the orientation tuning width, to characterize the orientation preference of each neuron. We recorded from low-firing but highly selective cells in both populations that responded to only one orientation in one direction (Figure 2.2D-E). The OSIs of RFP+ and RFP- neurons were statistically different (RFP+: 0.48 $\pm$ 0.29; RFP-: 0.67 $\pm$ 0.27; $p < 0.01$); however, both populations included highly selective neurons with OSIs equal to 1, and the distribution appears bimodal for the RFP+ population (Figure 2.2E). The orientation tuning width, calculated as the half-width at half-height of the best-fit Gaussian function, was also significantly different between the two populations (RFP+: 42.90 degrees $\pm$ 30.0; RFP-: 30.20 degrees $\pm$ 28.30; $p < 0.05$), though again both populations included sharply tuned cells. The direction selectivity index (DSI), computed by dividing the difference in the responses to the preferred orientation in two directions by the sum of the responses (Figure 2.2E), was not statistically different between the RFP+ and RFP- populations (RFP+: 0.51 $\pm$ 0.38; RFP-: 0.61 $\pm$ 0.39; $p = 0.22$).

Given the diversity of tuning characteristics in RFP+ cells, we considered whether waveform characteristics, which are known to vary in different types of basket cells and other PV+ inhibitory interneurons (Wang et al., 2002; Blatow et al., 2003), might correlate with orientation selectivity (Figure 2.3). However, high OSIs were found in cells with all waveform characteristics, and there was no significant relationship between any of the spike shape parameters and OSI, within the RFP+ population (Peak:Valley and OSI: $r = 0.13$, $p = 0.49$; Spike Width and OSI: $r = 0.04$, $p = 0.85$; Repolarization Rate and OSI: $r = 0.26$, $p = 0.16$) or the RFP- population (Peak:Valley and OSI: 0.23, $p = 0.47$; Spike Width and OSI: $r = -0.30$, $p = 0.34$; Repolarization Rate and OSI: $r = 0.26$, $p = 0.41$).

In separate experiments, we used two-photon guided cell-attached recording to assess the orientation tuning of GFP+ (GABAergic) neurons and GFP- (non-GABAergic)

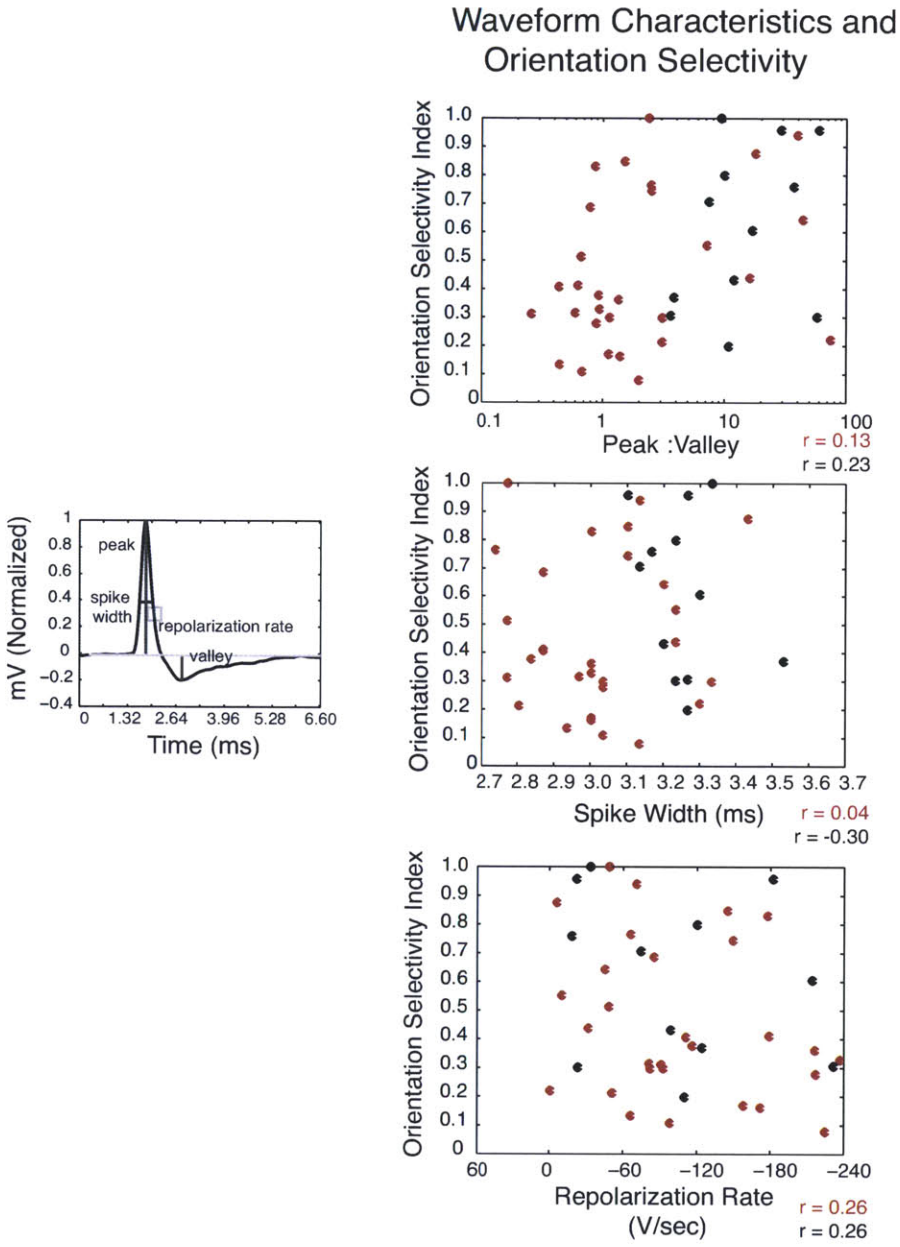

Figure 2.3. Diversity of spike shape is not related to orientation tuning selectivity in RFP+ and RFP- neurons. The waveform is plotted against the orientation selectivity index (OSI) for each visually-responsive RFP+ and each RFP- neuron. None of these parameters predicted the strength of tuning, as neurons with the strongest selectivity could be found with nearly every spike shape.

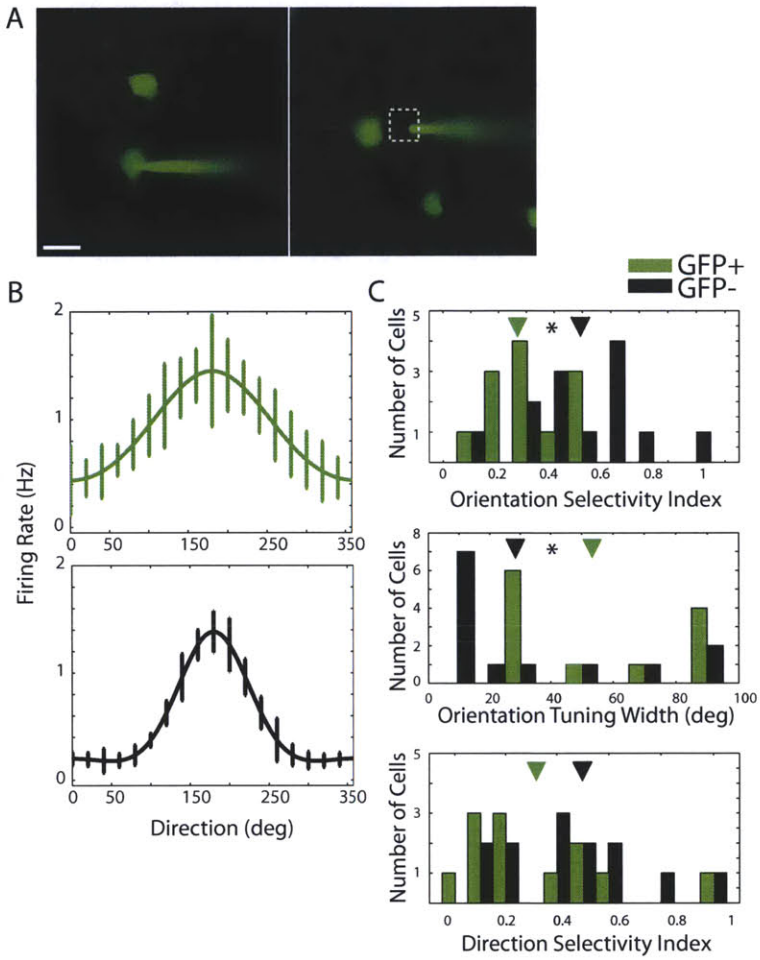

Figure 2.4. GFP+ (GABAergic) neurons are significantly less tuned than GFP- (non-GABAergic) neurons in the GAD67-GFP (Δneo) knock-in mouse line. (A) A patch pipette was targeted to GFP+ neurons (Left) and GFP- neurons (Right) under two-photon guidance, at depths between 100 and 300μm below the pial surface. After the visual response of each neuron shown was characterized, the cell was filled to confirm its identity. Scalebar = 20 μm (B) Tuning curves of a representative GFP+ neuron (green, OSI = 0.22, tuning width = 87.5 degrees, DSI = 0.54) and GFP- neuron (black, OSI = 0.73, tuning width = 12.2 degrees, DSI = 0.77). Error bars indicate the SEM. (C) Population histograms of the orientation selectivity index (Top), orientation tuning width (Middle), and direction selectivity index (Bottom). Asterisks indicate significant differences ($p < 0.05$), which were found between GFP+ and GFP- neurons for orientation selectivity index and tuning width. Arrowheads indicate the mean of each population.

neurons in adult mice heterozygous for the GAD67-GFP (Δneo) allele (Tamamaki et al., 2003). Replicating earlier findings in these mice (cf. Sohya et al., 2007; Liu et al., 2009a), we found that GFP+ neurons were significantly more broadly tuned than GFP- cells (Figure 2.4), as assessed with OSI (GFP+: 0.33 ± 0.13, n=12 cells; GFP-: 0.51 ± 0.21, n=13 cells; $p < 0.05$) and with tuning width (GFP+: 55.19 degrees ± 25.94; GFP-: 33.19 degrees ± 31.51; $p < 0.05$). Furthermore, the OSI range of GFP+ neurons (0.1-0.5) were not only different from the OSI range of GFP- neurons (0.1-1) in the same mice but also from that of PV+ neurons in PV-Cre mice (0.1-1; Figure 2.2E) and of fast-spiking neurons in wild-type mice (0.1 - 1.0 Niell and Stryker, 2008). That is, inhibitory neurons with the highest orientation selectivity are absent in GAD67-GFP mice, suggesting that the tuning properties of these neurons develop abnormally.

2.4.2.2 Calcium Imaging

To compare responses in a larger sample of cells, we assessed the orientation tuning properties of RFP+ and RFP- neurons with two-photon calcium imaging (typically 20-30 RFP- neurons and 2-4 RFP+ neurons were recorded simultaneously, Figure 2.5A,B).

We imaged 26 RFP+ and 173 RFP- visually responsive cells. The mean OSI in the two populations did not differ significantly (RFP+: 0.25 ± 0.12; RFP-: 0.25 ± 0.11; $p = 0.72$) (Figure 2.5C). In addition, the mean orientation tuning width was not significantly different in the two populations (RFP+: 36.02 degrees ± 31.89; RFP-: 39.23 degrees ± 31.44; $p = 0.84$). Thus PV+ interneurons displayed a range of orientation selectivity preferences, which was comparable to the rest of the visually responsive population of cells. RFP+ and RFP- cells with comparably sharp tuning were distributed among all animals and at all imaging depths. The mean DSI of the RFP+ cells (0.26 ± 0.11) also did not differ from that of the RFP- cells (0.27 ± 0.13; $p = 0.72$), although the highest DSIs of the RFP- cells were higher than those of the RFP+ cells.

2.4.3 Spatial frequency tuning and receptive field sizes are comparable in the RFP+ and RFP- populations

To further characterize the receptive fields of PV+ interneurons, we measured their spatial frequency tuning and receptive field sizes. The spatial frequency tuning

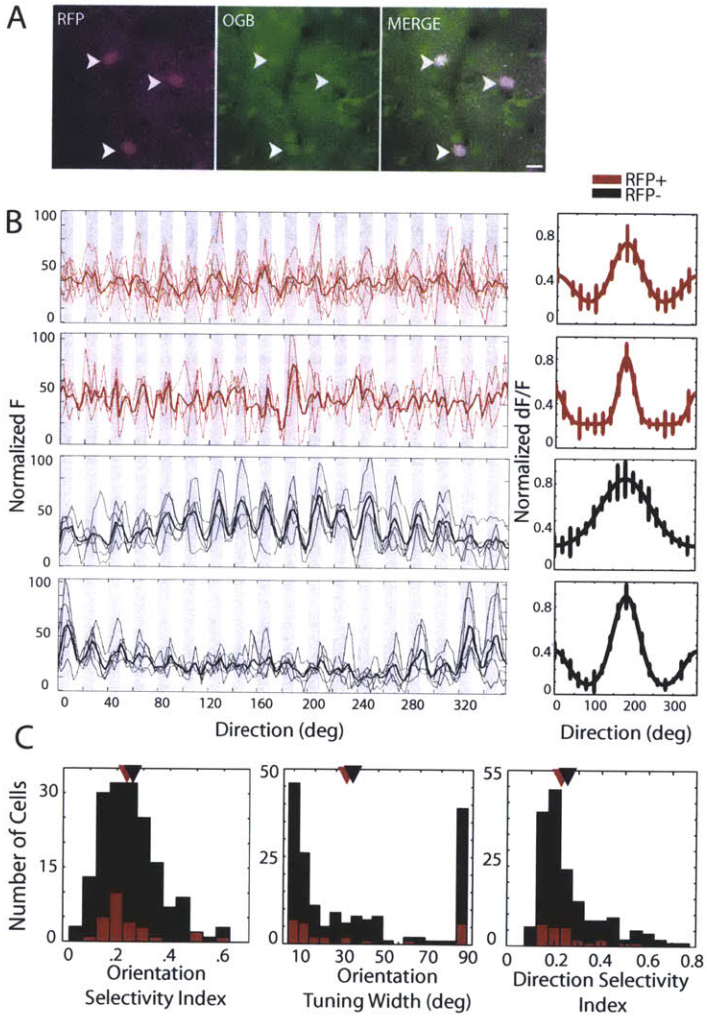

Figure 2.5. In vivo two-photon calcium imaging of RFP+ and RFP- neurons reveals extensive overlap in the orientation tuning properties of PV+ interneurons and the unlabeled population. (A) Two weeks after viral infection, the calcium indicator OGB was injected into the infected site. The RFP alone, OGB alone, and merged images are shown. Arrowheads point to the same cells in each image. Scalebar = 10μm. (B) (Left) Calcium indicator responses of representative RFP+ cells (red traces) and RFP- cells (black traces) to episodically-presented oriented gratings at 20-degree intervals; each grating was drifted in a direction orthogonal to the grating orientation (gray shading: ON periods of stimulus presentation, white: OFF). Raw single-trial traces (thin lines) and mean response trace (thick lines) are shown. (Right) Gaussian tuning curves were fitted to the calculated ΔF/F responses for each stimulus, as described in Methods. The peak response is set to 180 deg for ease of comparison. Top RFP+ cell: OSI = 0.23, tuning width = 32 deg, DSI = 0.3. Bottom RFP+ cell: OSI = 0.53, tuning width = 19 deg, DSI = 0.5. Top RFP- cell: OSI = 0.13, tuning width = 81 deg, DSI = 0.5. Bottom RFP- cell: OSI = 0.48, tuning width = 12 deg, DSI = 0.5. Error bars denote SEM. (C) Population histograms of the orientation and direction tuning properties of RFP+ (red) and RFP- (black) populations show the extensive overlap between the two cell populations in OSI, tuning width, and DSI. Arrowheads on histograms mark the mean of each population.

characteristics of cells in the visual pathway, starting with retinal ganglion cells, reflect the spatial extent and magnitude of receptive field 'centers' and 'surrounds' (Enroth-Cugell and Robson, 1966). Responses to different spatial frequencies were recorded either by calcium imaging or cell-attached electrophysiology (Figure 2.6), and then fit to a Difference of Gaussians (DOG) model (Enroth-Cugell and Robson, 1966; 1984; Shapley and Lennie, 1985).

The preferred spatial frequency of cells measured with calcium imaging (Figure 2.6A) did not differ significantly between the RFP+ and RFP- populations (RFP+: 0.031 cpd $\pm$ 0.019; RFP-: 0.033 cpd $\pm$ 0.024; $p = 0.81$). The tuning bandwidth was defined as the ratio of spatial frequencies with half-maximal responses. The mean bandwidths of the two populations were also similar (RFP+: 5.70 octaves$\pm$ 0.67; RFP-: 5.55 octaves $\pm$ 0.92; $p=0.97$). The presence of a low frequency roll-off in the spatial frequency tuning curves is consistent with a suppressive receptive field surround mechanism. The demonstration of this roll-off in some PV+ inhibitory neurons indicates that at least some inhibitory cells have suppressive receptive field components (Figure 2.7).

In fact, the spatial frequency tuning curve of a neuron can be interpreted as the Fourier transform of its spatial receptive field (Enroth-Cugell and Robson, 1966). In V1 cells, for instance, significant low spatial frequency roll-offs likely indicate suppressive 'surrounds' to their receptive field 'centers' (Sceniak et al., 1999), consistent with lateral inhibition impinging on these cells or in input pathways to these cells. We were surprised to find that many PV+ cells did in fact have significant suppressive 'surrounds' (Figures 2.6, 2.7).

Although the DOG model is most applicable to circular receptive fields with concentric center and surround regions, we essentially assessed the spatial frequency tuning at the preferred orientation of each neuron, measuring the spatial frequency tuning orthogonal to the long axis of the oriented receptive field. Thus the DOG fit allowed us to estimate the extent of 'center' and 'surround' of each cell orthogonal to the orientation axis (Figure 2.6). The 'surround' inhibition could be supplied by either the subfield antagonism of the OFF flank of a simple cell, or the suppressive surround of a complex cell. We found considerable heterogeneity in the extent of surround inhibition in both the RFP+ and RFP- populations, ranging from cells with minimal or no suppressive surrounds to others with

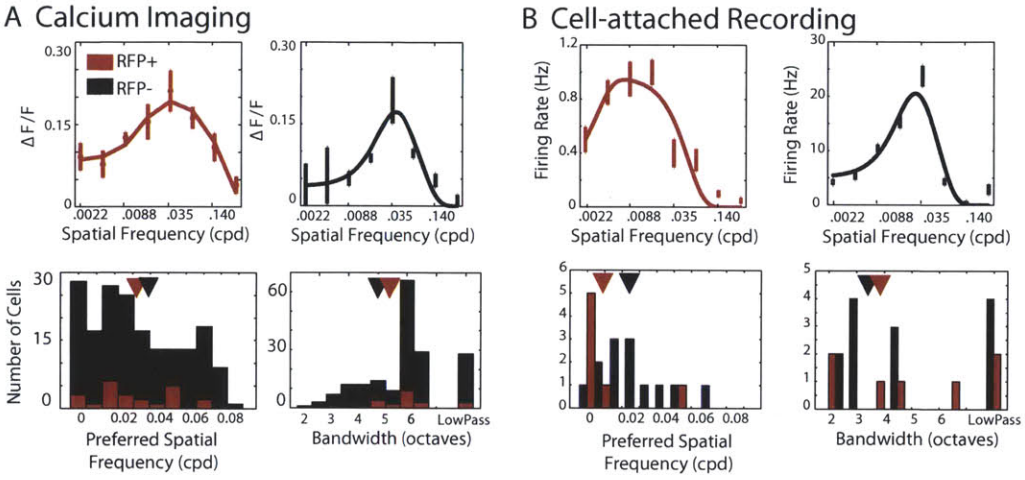

Figure 2.6. Spatial frequency tuning is similar in the RFP+ and RFP- populations when measured with in vivo two-photon calcium imaging and cell-attached electrophysiological recordings. (A) Calcium imaging data. (Top) The best Difference of Gaussians fit to the dF/F responses for two representative cells (see Figure S3 for raw traces of the data). RFP+ cell: Preferred spatial frequency (PSF) = 0.04 cpd, bandwidth = 5.1 octaves. RFP- cell: PSF = 0.04 cpd, bandwidth = 2.7 octaves. Error bars indicate SEM. (Bottom) Population histograms of the preferred spatial frequency and spatial frequency tuning bandwidth are shown for the RFP+ and RFP- populations. The low-pass bin denotes cells with no low spatial frequency roll-off. Arrowheads denote the mean of each distribution. (B) Cell-attached recording data. (Top) The best Difference of Gaussians fit to the spike responses of representative RFP+ and RFP- cells. RFP+ cell: PSF = 0.007 cpd, bandwidth = 4.7 octaves, RFP- cell: PSF = 0.03 cpd, bandwidth = 2.6 octaves. (Bottom) Population histograms of the preferred spatial frequency and spatial frequency tuning bandwidth.

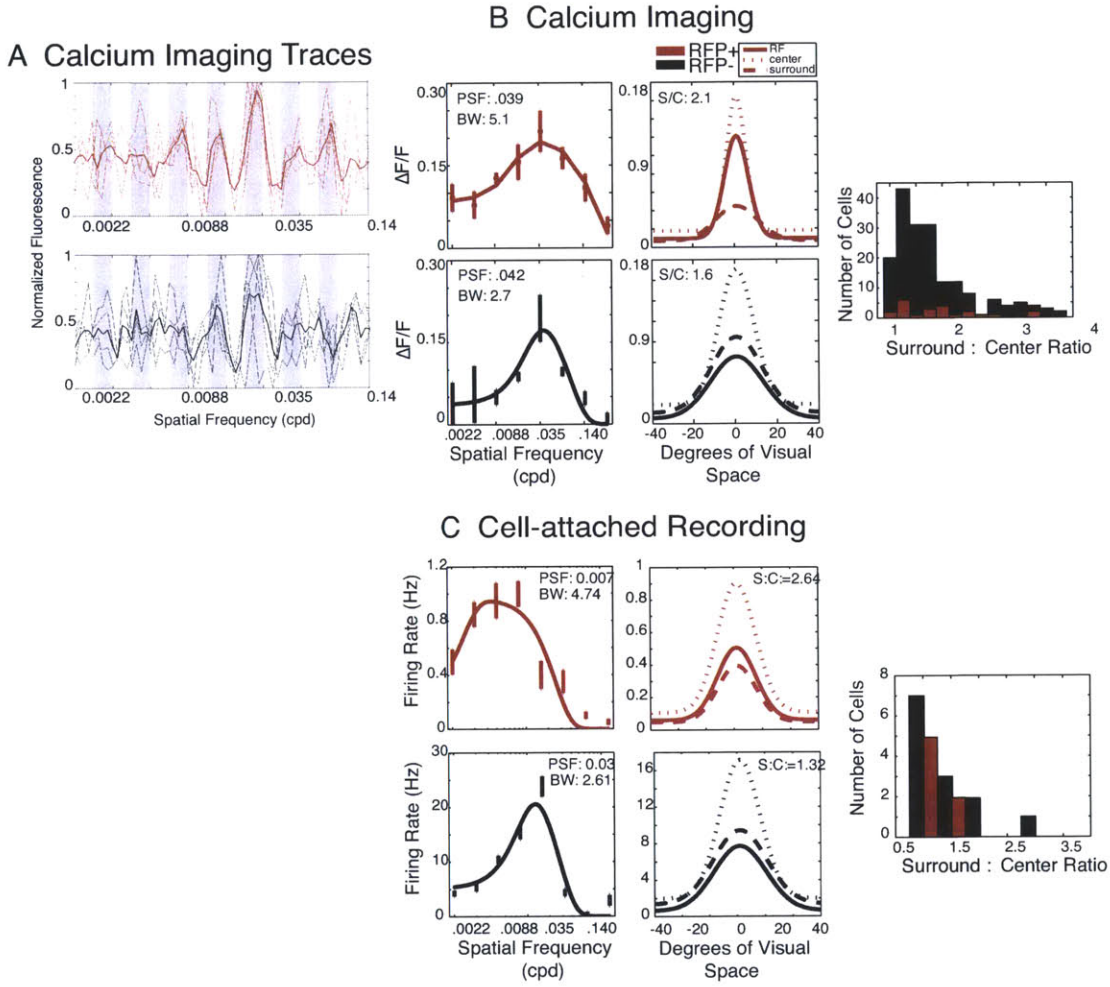

Figure 2.7. Difference of Gaussians model of spatial frequency tuning reveals surround suppression in RFP+ neurons. (A) The raw calcium indicator traces for the RFP+ (red) and RFP- (black) neurons shown in Figure 2.6 in response to 7 episodically presented spatial frequencies (gray-ON, white-OFF), are overlaid with the mean of these traces. (B) (Left) The Difference of Gaussians model fit to the dF/F responses from the neurons in (A) are shown on the left. Error bars indicate the SEM. (Middle) The inverse Fourier transforms of the excitatory and inhibitory components are plotted. (Right) Population histograms of the ratio of the inhibitory surround: excitatory center sizes. PSF, preferred spatial frequency; BW, bandwidth; S/C, surround/center size. (C) As in B, showing data from an RFP+ and an RFP- neuron obtained with cell-attached electrophysiological recording. The surround:center sizes are similar to those obtained with calcium imaging.

strong surround components in their responses (Figures 2.6A-B, 2.7B-C). The mean ratio of the estimated surround to the center radius of the receptive field was 1.93 (± 0.80) in the RFP+ and 1.82 (± 0.77) in the RFP- population. These distributions were not significantly different from one another ($p = 0.45$). In a subset of visually responsive RFP+ neurons (n=7) and RFP- neurons (n=13), we measured the spatial frequency tuning with cell-attached electrophysiological recordings (Figure 2.6B). The mean preferred spatial frequency of the RFP+ cells (0.03 cpd ± 0.01) and of the RFP- cells (0.06 cpd ± 0.01) did not differ significantly ($p = 0.16$). Similarly, the mean tuning bandwidth of the two populations also did not differ (RFP+: 3.88 octaves ± 2.03; RFP-: 3.13 octaves ± 1.90; $p = 0.58$).

Measurement of the 'classical center' of a receptive field provides an estimate of the spatial spread of inputs to a cell and of the influence of the cell's activity within the visual cortex. Because recent work has shown that inhibitory cells in general may have larger receptive fields than excitatory cells (Niell and Stryker, 2008; Liu et al., 2009a), we expected PV+ cells to follow this trend and even have some of the largest receptive fields of all cells.

We estimated receptive field 'center' size in both the azimuth and elevation axes by measuring the calcium response to a bar (containing a contrast-reversing checkerboard) that was moved progressively across each axis, and fitting a Gaussian function to the calcium response (Figure 2.8). The half-width at half height (HWHH) of this function was used as an estimate of receptive field size. The RFP+ and RFP- cell populations had similar distributions of receptive field size: for RFP- cells, the mean HWHH was 19.84 degrees (± 7.37) in the elevation axis and 21.80 degrees (± 10.02) in the azimuth axis, whereas for RFP+ cells, the mean HWHH was 21.38 degrees (± 8.00) in the elevation axis and 23.43 degrees (± 7.54) in the azimuth axis. Although the RFP+ cells tended to have larger receptive field sizes in both dimensions, the trend was not significant (Azimuth: $p = 0.36$; Elevation: $p = 0.54$). These receptive field features suggest that PV+ cells are likely involved in spatially local processing, despite their potentially large area of cortical influence (Somogyi et al., 1983; Kisvárday and Eysel, 1993; Stepanyants et al., 2009).

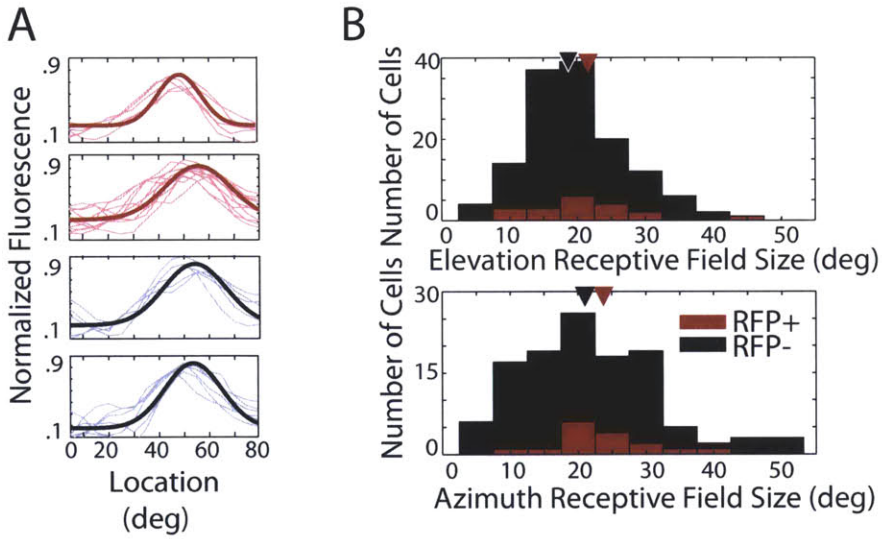

Figure 2.8. The spatial receptive field sizes of the RFP+ and RFP- populations overlap significantly when measured with in vivo two-photon calcium imaging. (A) The raw calcium indicator fluorescence response to each presentation of a periodically drifting checkered bar in the elevation axis (light traces), overlaid with the best-fit Gaussian (dark traces) for two representative RFP+ (red) and RFP- (black) cells. (B) Population histograms of the receptive field size (half width at half height) in the elevation and azimuth axes. Arrowheads indicate the mean of each distribution.

2.4.4 High response specificity is associated with low firing rates

The cell-attached recordings of RFP+ and RFP- cells revealed an inverse relationship between orientation selectivity and peak response rate. The cells with the highest OSIs had low response rates (Figure 2.9A); this is also evident in the individual representative cells with high OSIs (Figure 2.2D). Since the calcium imaging was performed at a frame rate of 1Hz, we suspected that some of the most selective cells would be missed, because at this frame rate calcium signals generated by the few spikes emitted by low-firing cells would lie near the threshold for detection. Indeed, while the calcium imaging data confirmed an inverse relationship between OSI and peak response (Figure 2.9B), cells with the highest OSIs were not included (see also Sohya et al., 2007 for a similar range of OSIs recorded with traditional calcium imaging). Thus, the OSIs of the RFP+ cells measured with calcium imaging were lower than those measured with cell-attached recording ($p<0.05$), as were the OSIs of RFP- cells ($p<0.05$), though the orientation tuning widths of RFP+ or RFP- populations were not different when measured with the two methods ($p>0.1$). However, new fast-scan methods of rapidly assessing calcium responses along arbitrary scan paths that sample selected cells reveal as high OSIs of RFP+ and RFP- cells with calcium imaging as with electrophysiological recording, importantly including cells with low firing rates (Figure 2.9C,D).

2.4.5 Comparison of PV+ and SOM+ response properties

In similar experiments, we used the same viral injection procedure to label Somatostatin-expressing (SOM+) inhibitory interneurons in SOM-Cre mice, and then targeted these RFP+ SOM+ neurons for cell-attached recordings under two-photon guidance (n = 13). Most of these neurons were highly selective for orientation (Figure 2.10). The response properties of SOM+ neurons as they compare to PV+ and unlabeled neurons (RFP-) are shown in Figure 2.11. Similar to the PV+ population described above, the spontaneous firing rate of SOM+ neurons was higher than the unlabeled neurons (SOM = 0.99 $\pm$ 2.5 Hz, PV = 1.06 $\pm$ 1.92 Hz, RFP- = 0.09 $\pm$ 0.5 Hz; SOM vs PV: $p = 0.92$, SOM vs RFP-: $p < 0.01$; PV vs RFP-: $p < 0.001$). However, visually evoked firing rates in the SOM+ population were lower than both the PV+ and the RFP- cell firing rates (SOM = 1.31 $\pm$ 1.44, PV = 7.37 $\pm$ 7.47, RFP- = 5.62 $\pm$ 8.40; SOM vs PV: $p < 0.01$, SOM vs RFP-: $p = 0.07$, PV vs RFP-

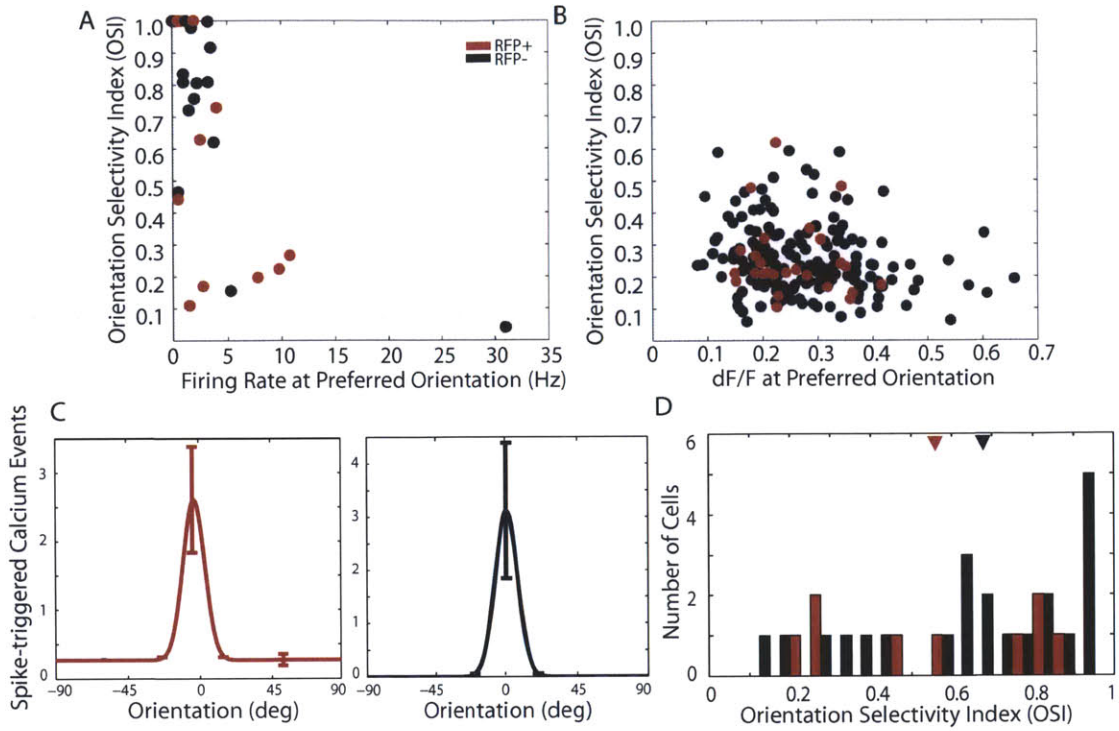

Figure 2.9. High orientation selectivity is associated with low firing rates, but can be captured with fast scan calcium imaging. (A) Cell-attached recordings. The orientation selectivity index (OSI) is negatively correlated to the mean firing rate at the preferred orientation for all neurons recorded in PV-Cre mice ($r = -0.58$, $p<0.05$; red: RFP+, black: RFP-). Many of the cells with the highest orientation selectivity (OSI ~1.0) fire at rates less than 2Hz at the preferred orientation. (B) Calcium imaging. The OSI is plotted against the calcium response (dF/F) at the preferred orientation for each visually-responsive cell (red: RFP+, black: RFP-). A similar negative correlation between OSI and response rate is evident ($r = -0.18$, $p<0.05$). The lower maximal OSIs suggest that the threshold of detection with traditional slow-scan two-photon imaging does not capture the population of low-firing but highly selective cells. (C) The tuning curve of a highly selective RFP+ neuron (red, OSI = 0.87), and RFP- neuron (black, OSI = 0.91), whose calcium responses were imaged with fast two-photon imaging. Briefly, calcium indicator (OGB) responses to oriented gratings were imaged using a custom arbitrary scan path algorithm (Lillis et al., 2008), which guided the laser preferentially from neuron to neuron, allowing us to sample each neuron at 50Hz, up to 50 times faster than the traditional frame-wide scanning. Fluorescence responses were smoothed and deconvolved with a kernel that corresponded to the time course of the calcium indicator that associated with a single spike, to estimate instantaneous firing rates (Yaksi and Friedrich, 2006). These derived firing rates were converted to weighted spike-evoked events (Rothschild et al., 2010) by thresholding at 1Hz, which were used to calculate the tuning curves. Error bars indicate the SEM. (D) The population histogram of OSIs of RFP+ (red bars) and RFP- (black bars) neurons measured with fast calcium imaging shows that fast imaging allows the detection of the highly selective but low firing neurons that we observed with cell-attached recordings. (OSIs: RFP+: 0.55 + .26, RFP-: 0.67 + 0.25, $p > 0.2$).

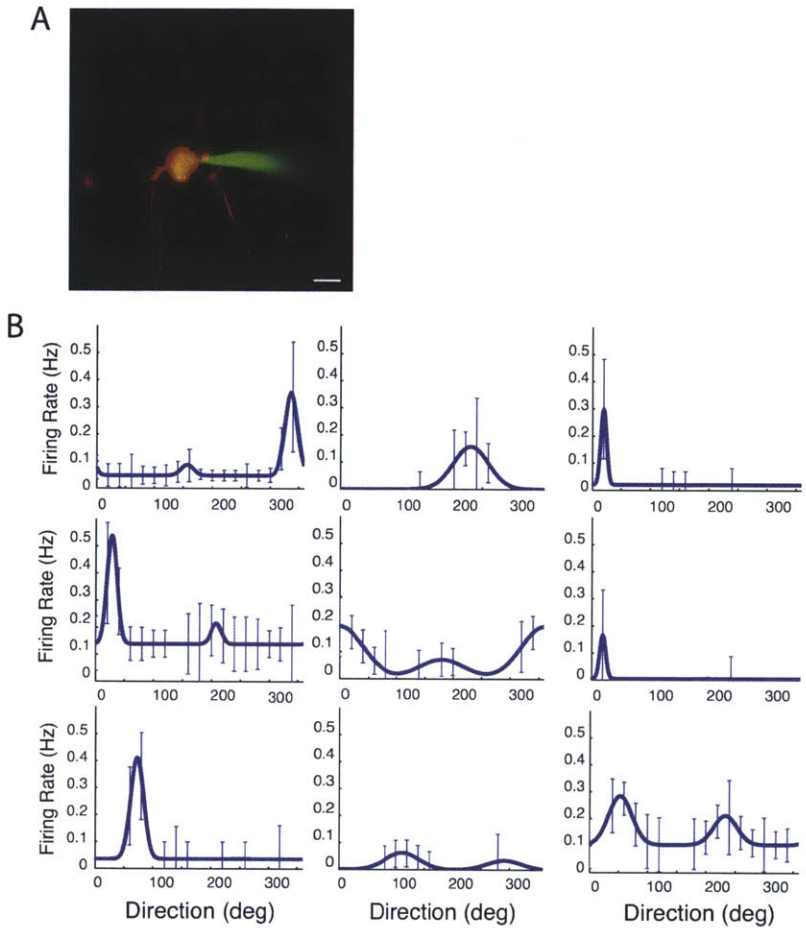

Figure 2.10. Orientation and direction tuning was measured in SOM+ neurons through two-photon targeted cell-attached recordings. (A) RFP-expressing SOM+ neurons were targeted with a patch-pipette filled with green dye (Alexa 488). Scalebar = 25μm. (B) Orientation/direction tuning of 9 example SOM+ neurons are shown. Most SOM+ neurons recorded in this set of experiments were highly selective for orientation.

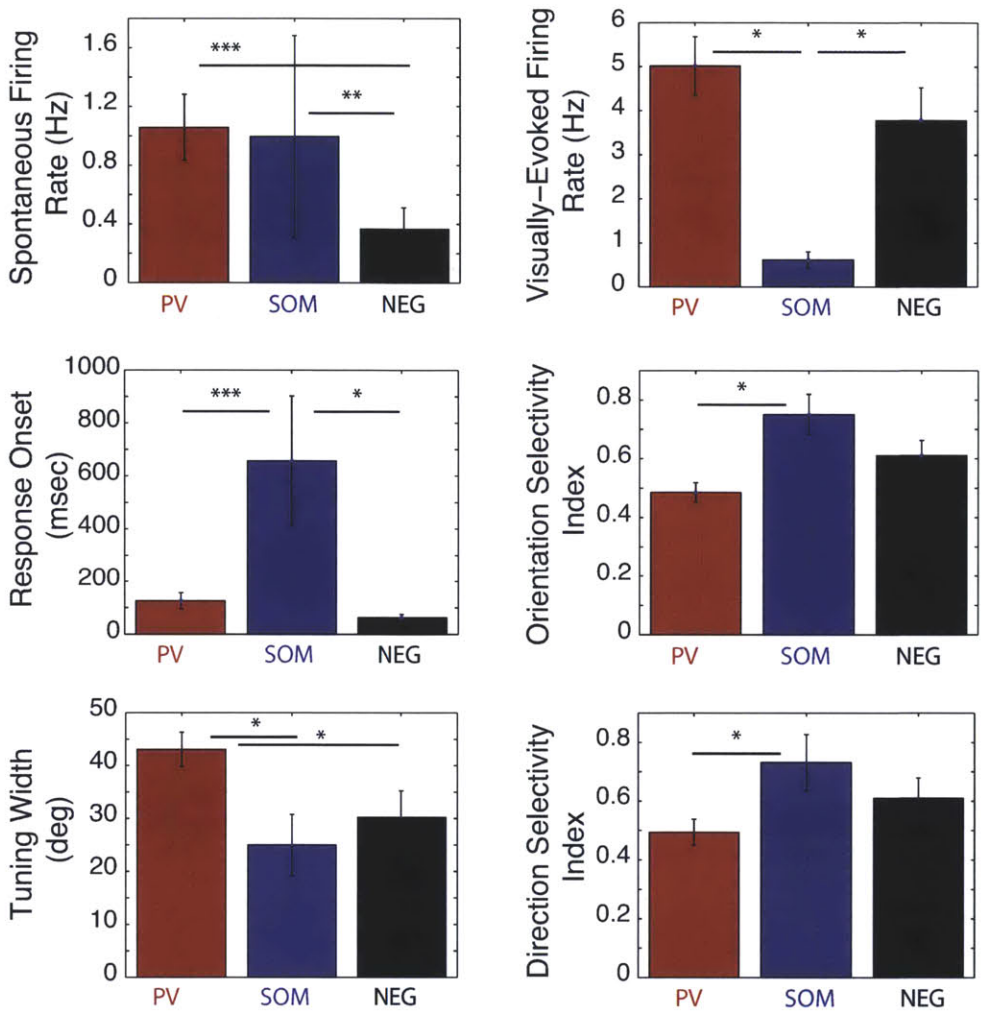

Figure 2.11. Comparison of the visual response properties of Parvalbumin-expressing (PV+) and Somatostatin-expressing (SOM+) neurons. SOM+ neurons (n = 13) were labeled in vivo using the SOM-Cre mouse line and the same floxed RFP virus used for the PV labeling in earlier experiments. SOM+ neurons tend to respond with lower firing rates and delayed response onsets, compared to PV+ and unlabeled neurons. The orientation selectivity of these responses is sharper in SOM+ neurons. Asterisks denote significant differences: * p<.05, ** p<.01, *** p<.001, + p<.15.

: $p = 0.29$). Furthermore, the onset of visual responses was delayed in SOM+ neurons (SOM = 0.61 ± 0.91 sec, PV = 0.05 ± 0.11 sec, RFP-: 0.07 sec $\pm$ 0.09 sec; SOM vs PV: $p < 0.001$, SOM vs RFP-: $p < 0.05$, PV vs RFP-: $p = 0.18$). These responses in SOM+ neurons tend to be highly selective for orientation. The orientation selectivity index (OSI) was significantly higher in SOM+ neurons than in PV+ neurons, but similar to the RFP- population (SOM = 0.77 ± 0.25, PV = 0.49 ± 0.28, RFP- = 0.67 ± 0.29; SOM vs PV: $p < 0.001$, SOM vs RFP-: $p = 0.27$, PV vs RFP-: $p < 0.01$). Similarly, the tuning width, calculated as the half-width at half-height of the best Gaussian fit of the orientation responses, was significantly narrower in the SOM+ neurons than in the PV+ cells, and similar to the unlabeled cells. (SOM = 25.0 ± 20.8 deg, PV = 43.0 ± 28.1 deg, RFP-: 30.2 ± 28.3 deg; SOM vs PV: $p < 0.05$, SOM vs RFP-: $p = 0.55$, PV vs RFP-: $p < 0.05$). Finally, SOM+ cells tended to be more direction selective than PV+ cells, as quantified with the direction selectivity index (DSI), but SOM+ DSIs did not differ from those of the RFP- population (SOM = 0.73 ± 0.35, PV = 0.49 ± 0.38, RFP- = 0.61 ± 0.39; SOM vs PV: $p < 0.05$, SOM vs RFP-: $p = 0.34$, PV vs RFP-: 0.16). To summarize, preliminary recordings from a small number of SOM+ neurons ($n = 13$) suggest that these cells respond to visual stimuli very weakly, they have low visually-evoked firing rates with delayed onsets, but with very high selectivity.

2.5 Discussion

We have shown that the receptive field properties of PV+ cells are diverse, and even match the range of properties expressed in the general neuronal population in the primary visual cortex. However, more PV+ cells respond broadly to all orientations, while a smaller number of PV+ neurons have sharp orientation selectivity. Their receptive field sizes are similar to those of the general population, and they prefer a similar range of spatial frequencies. A Difference of Gaussians model characterizing their spatial frequency responses shows that many PV+ cells have bandpass spatial frequency tuning characteristics. Furthermore, we have compared PV+ responses to SOM+ responses, and

preliminary recordings suggest that the SOM+ population tends to have weak, delayed visual responses that are highly selective for orientation.

2.5.1 Visual response properties of PV+ neurons and their roles in cortical circuits

PV+ neurons provide inhibition to the soma and proximal dendrites, allowing them to strongly suppress postsynaptic activity; in addition, certain PV+ cell axonal fields extend for hundreds of microns, allowing them to supply long-range lateral inhibition (Kisvárday et al., 2002; Wang et al., 2002). Since cortical PV+ cells include several subtypes of basket cells and chandelier cells (Wang et al., 2002; Markram et al., 2004; Burkhalter, 2008), and are neurochemically heterogeneous (Chow et al., 1999; Vruwink et al., 2001), it is perhaps not surprising that we have found diverse response properties and narrow as well as broad tuning in this cell population. In future studies, it would be informative to determine whether the individual gene expression patterns of PV+ cells correlate with unique response features (Wang et al., 2002).

The high response specificity of many PV+ cells indicates that they acquire this specificity in the same manner as do other, excitatory, cells. It has been argued that feature-selective responses in visual cortex, including orientation selectivity, may be explained by feedforward excitatory drive from thalamic neurons combined with membrane nonlinearities such as the spike threshold (Priebe and Ferster, 2008). In this view, excitatory and inhibitory neurons in cortex generate their orientation (and other) selectivity in similar ways, with precise feedforward connections from aligned geniculocortical afferents as the principal source of specificity (Ferster et al., 1996; Chung and Ferster, 1998).

Even in feedforward models, intracortical inhibition has been proposed to have two roles (Ferster and Miller, 2000; Lauritzen and Miller, 2003; Palmer and Miller, 2007). Feedforward push-pull models postulate the existence of inhibitory "pull" of opposing polarity to complement the excitatory "push" generated by thalamocortical projections in simple excitatory cells, which would further sharpen their stimulus selectivity. Sharp tuning of a subset of PV+ cells, as demonstrated here, is consistent with this proposal. In addition, broadly tuned inhibitory complex cells are proposed to be important for contrast-

invariant orientation tuning (but see Finn et al., 2007). Another subset of the PV+ population is broadly tuned and well suited to provide such inhibition.

Models of cortical circuits that combine feedforward thalamocortical excitation with intracortical excitation and inhibition (Douglas et al., 1995; Somers et al., 1995; Sompolinsky and Shapley, 1997) also predict a range of orientation selectivity for inhibitory interneurons. Importantly, inhibitory conductances need to precisely balance excitatory conductances in order to generate sharp orientation tuning, particularly within orientation representations with diverse local neighborhoods (Mariño et al., 2005). It is parsimonious to suggest that selective PV+ cells generate their response specificity via precise thalamocortical and intracortical connections and themselves contribute to the sharpening of selectivity of other neurons in the local network.

Our demonstration that many PV+ neurons have highly selective responses suggests that rather than simply dampening activity non-specifically (Wang et al., 2004), perisomatic inhibition provided by these cells encodes specific visual information that may sharpen representations within the network. Indeed, not only the inputs but also the targets of individual PV+ cells seem to be highly specific. Despite the huge axonal fields of some PV+ cells, their targeting is nonrandom (DeFelipe and Fariñas, 1992), and in cat visual cortex, they specifically target postsynaptic partners with iso-orientation preferences locally and cross-orientation preferences distally (Kisvárday et al., 2002; Wang et al., 2002). Individual layer 2/3 fast-spiking cells belong to precise micro-networks, where they interconnect preferentially with specific pyramidal cells with which they share common inputs (Yoshimura and Callaway, 2005). Our data provide additional evidence of this highly specific interconnectivity, the computational utility of which is particularly striking in mouse V1, where large domains devoted to single orientations do not exist and adjacent cells frequently vary widely in orientation preference (as at pinwheel centers in cat or ferret V1). Here, orientation-specific connections cannot simply rely on map-based spatial relationships (Ohki and Reid, 2007), though inhibitory and excitatory inputs have tightly matched tuning in mouse V1 (Tan et al., 2011). The functional heterogeneity of PV+ neurons may result from a unique cell-specific connectivity, including the possibility that sharply tuned inhibitory neurons coexist in local networks with other cells with sharp tuning. An important future goal will be to understand how the properties of these cortical

interneurons correspond with their connectivity profiles and the properties of the cells whose outputs they modulate.

2.5.2 Properties of SOM+ neurons and their roles in cortical circuits

Neurons expressing the neuropeptide somatostatin (SOM) constitute a distinct population of inhibitory interneurons: in the rodent cortex, PV is not expressed in SOM+ neurons, and vice versa (Kubota et al., 1994; Gonchar and Burkhalter, 1997; Kawaguchi and Kubota, 1997; Gonchar et al., 2007; Xu et al., 2010). The features that distinguish PV+ and SOM+ neurons have important computational implications. In contrast to PV+ neurons that form a large proportion of their synapses on the perisomatic region of their targets, most synapses from SOM+ neurons are located on the dendrites of target cells; Martinotti cells are the largest morphological subclass of SOM+ cells, though bitufted cells and, more rarely, basket cells can also express SOM (Kawaguchi and Kubota, 1997; Gonchar et al., 2002; Ma et al., 2006; McGarry et al., 2010).

The weak, delayed visual responses of SOM+ cells recorded here and by others (Ma et al., 2010) are consistent with the synaptic properties of these cells recorded *in vitro*. The excitatory synaptic inputs to SOM+ neurons are weak, with slow rise times and low frequencies of recorded mini EPSPs, but are dramatically facilitating with sustained excitatory drive (Dumitriu et al., 2006; Fanselow et al., 2008; Tan et al., 2008). These response patterns suggest that SOM+ cells are probably not involved in the initial shaping of response selectivity of other cells, but rather that they may be involved in adaptation responses, or in suppressing over-excitation, as they may mediate mutual inhibition between pairs of cortical excitatory neurons (Kapfer et al., 2007; Silberberg and Markram, 2007).

2.5.3 Comparison with other studies

The present study is not the first attempt to measure the visual receptive field properties of subclasses of inhibitory interneurons, but important contradictions have been found across species. In the superficial layers of V1 in cats, studies using intracellular recording to classify electrophysiological profiles have revealed inhibitory cells with a broad range of receptive field properties similar to those of excitatory cells, including

sharply tuned inhibitory cells with simple receptive fields, and broadly tuned inhibitory cells with complex receptive fields (Hirsch et al., 2003; Cardin et al., 2007; Nowak et al., 2008). In mouse V1, however, despite the fact that the receptive field selectivity in excitatory cells rivals those of higher mammals (Niell and Stryker, 2008), genetically marked GAD67+ cells in GAD67-GFP (Δneo) knock-in mice show poor selectivity for orientation (Sohya et al., 2007; Liu et al., 2009b; Kerlin et al., 2010) a finding that we have replicated (Figure 2.4). Importantly, the GAD67-GFP (Δneo) knock-in mice develop with lower expression levels of GABA (Tamamaki et al., 2003), and even such a partial knockdown of GAD67 expression in PV+ cells has been shown to drastically alter their connectivity, reducing the number of perisomatic boutons and the number of axonal branches (Chattopadhyaya et al., 2007). This deficiency in the construction of inhibitory circuits would be expected to have significant effects on the development and plasticity of cortical neuron properties (Hensch, 2004; Yazaki-Sugiyama et al., 2009). Furthermore, specific alterations in GABA-mediated transmission in the hippocampus of GAD67-GFP (Δneo) mice have been described (Lu et al., 2010). Still, functional differences in the GAD67-GFP (Δneo) mice could be more pronounced in visual cortex than elsewhere (Gentet et al., 2010). Another possibility is that GFP is not expressed uniformly in all inhibitory cells in GAD67-GFP (Δneo) mice. Indeed, some cells are considerably brighter than other nearby GFP+ cells (data not shown). If the highly tuned population of PV+ cells that we have recorded expresses lower levels of GFP, they may be overlooked in visually-targeted recording methods.

Another study in the mouse visual cortex found that a portion of fast-spiking (presumed inhibitory) cells were highly orientation selective, but that the proportion of such cells was lower than for neurons with larger spike widths (Niell and Stryker, 2008). At first glance, this study might appear to contradict our present results. However, it is likely that the populations of neurons sampled with these two approaches do not completely overlap – not all fast-spiking neurons are inhibitory, not all fast-spiking neurons are PV+, and not all PV+ cells are fast-spiking (reviewed by Markram et al., 2004). Furthermore, our recordings were targeted to layers 2/3. By focusing on a very specific population – superficial PV+ inhibitory interneurons – we have been able to draw attention to a subtype of PV+ neurons with the highest response selectivity. Further, since this work

was originally published (Runyan et al., 2010), several studies using similar genetic methods have described the existence of sharply tuned PV+ neurons (Hofer et al., 2011; Zariwala et al., 2011).

Similar to the findings presented here, a recent study used a mouse line that expresses GFP specifically in a subset of SOM+ neurons, and found that SOM+ neurons have highly selective yet weak and delayed responses (Ma et al., 2010), in contrast to the calcium imaging study described above (Kerlin et al., 2010). Perhaps only a subset of SOM+ neurons display this behavior; we only recorded from a small number of SOM+ neurons in our preliminary study, and the Ma et al. study recorded from a genetically defined subclass of SOM+ neurons (2010). Such highly selective but weak responses of some SOM+ neurons may be difficult to detect using traditional raster scanning calcium imaging methods, which may explain the discrepancy with the earlier study (Kerlin et al., 2010). Further, the activity patterns of SOM+ neurons may be particularly sensitive to different brain states; they are strongly excited by acetylcholine application *in vitro* (Fanselow et al., 2008), and in the awake somatosensory cortex, are depolarized during a quiet state, yet hyperpolarized by both voluntary and external whisker stimulation (Gentet et al., 2012). Peak firing rates of excitatory neurons are affected by brain state (Niell and Stryker, 2010) – a simple increase peak excitatory firing rate could have very different effects on PV+ neurons, whose excitatory inputs are depressing, and SOM+ neurons, whose excitatory inputs are facilitating (Dumitriu et al., 2006; Tan et al., 2008).

Furthermore, because mu-opioid receptors are not expressed in the cortex, the cortical effects of fentanyl anesthesia on the cortex are indirect (Mansour et al., 1995). Still, its direct effects are on widely targeting brain areas; for instance, fentanyl reduces cortical acetylcholine release by binding mu-opioid receptors in the midbrain and brainstem, which may further reduce the activity of SOM+ neurons in particular (Brown et al., 2010). This could mean that although we recorded PV+ and SOM+ neurons under identical anesthetic conditions and brain states, these cell classes could have been differentially affected by the anesthetic. Therefore, it remains important to study both PV+ and SOM+ properties in a variety of brain states, including the awake brain in different behavioral conditions. Inhibitory neurons, especially SOM+ neurons, are likely to respond differently across brain states, which may be a key aspect of their functional roles within cortical circuits.

2.5.4 Lumping or splitting subclasses of inhibitory interneurons

Our results highlight the issues with defining inhibitory neuronal subclasses along single dimensions, even by the expression of a specific protein marker. The idea of PV expression defining a homogeneous cell class was enticing: a large proportion of these cells are fast-spiking, they primarily include basket cells, they do not express other interneuron marker proteins such as somatostatin or calretinin, and, importantly, they primarily provide perisomatic inhibition (Markram et al., 2004; Zaitsev et al., 2005; Gonchar et al., 2007). However, recent studies have revealed diversity in gene expression, morphology and postsynaptic type within the PV+ population (Gupta et al., 2000; Wang et al., 2002; Markram et al., 2004; Burkhalter, 2008), and additional subtypes of PV+ inhibitory interneurons have also been reported, including multipolar bursting cells, a superficial population with regular spiking properties and non-basket morphology (Blatow et al., 2003). These overlapping layers of diversity suggest that PV+ neurons are multidimensional, and need to be defined by a combination of features including structure, connections, gene expression profiles, electrophysiological properties and response patterns (Parra et al., 1998).

Similarly, morphological, chemical, and electrophysiological diversity is strong within the SOM+ inhibitory neuron population. While SOM+ neurons and Martinotti cells are often considered equivalent cell classes, only 50% of SOM+ neurons are layer 1 targeting Martinotti cells (Ma et al., 2006; McGarry et al., 2010). Multipolar and bipolar morphologies can also express SOM (Gonchar et al., 2002; Ma et al., 2006; McGarry et al., 2010), and these neurons can differ in their expression of calcium binding proteins and neuropeptides (Kawaguchi and Kubota, 1996; Ma et al., 2006), and in their membrane and firing properties (Kawaguchi and Kubota, 1996; 1997; McGarry et al., 2010).

Still, many insights into the function of cortical circuits will result from comparing PV+ neurons to SOM+ neurons, despite their own diversity, and we should be cautious in endlessly splitting cell types into ever more distinct subclasses. Every cell in the brain is unique, given its unique set of connections, activity history, and gene expression patterns. The proximally targeted, rapid, yet shortlived inhibition provided by PV+ neurons and the distal, building inhibition provided by SOM+ neurons must have critical and

complementary roles in shaping the responses of their targets, as future studies manipulating their activity will show.

2.6 References

Anderson JS, Carandini M, Ferster D (2000) Orientation tuning of input conductance, excitation, and inhibition in cat primary visual cortex. J Neurophysiol 84:909–926.

Blatow M, Rozov A, Katona I, Hormuzdi SG, Meyer AH, Whittington MA, Caputi A, Monyer H (2003) A Novel Network of Multipolar Bursting Interneurons Generates Theta Frequency Oscillations in Neocortex. Neuron 38:805–817.

Brown EN, Lydic R, Schiff ND (2010) General anesthesia, sleep, and coma. N Engl J Med 363:2638–2650.

Burkhalter A (2008) Many specialists for suppressing cortical excitation. Front Neurosci 2:155–167.

Cardin JA, Carlén M, Meletis K, Knoblich U, Zhang F, Deisseroth K, Tsai L-H, Moore CI (2009) Driving fast-spiking cells induces gamma rhythm and controls sensory responses. Nature 459:663–667.

Cardin JA, Palmer LA, Contreras D (2007) Stimulus feature selectivity in excitatory and inhibitory neurons in primary visual cortex. J Neurosci 27:10333–10344.

Chattopadhyaya B, Di Cristo G, Wu CZ, Knott G, Kuhlman S, Fu Y, Palmiter RD, Huang ZJ (2007) GAD67-mediated GABA synthesis and signaling regulate inhibitory synaptic innervation in the visual cortex. Neuron 54:889–903.

Chow A, Erisir A, Farb C, Nadal MS, Ozaita A, Lau D, Welker E, Rudy B (1999) K(+) channel expression distinguishes subpopulations of parvalbumin- and somatostatin-containing neocortical interneurons. J Neurosci 19:9332–9345.

Chung S, Ferster D (1998) Strength and orientation tuning of the thalamic input to simple cells revealed by electrically evoked cortical suppression. Neuron 20:1177–1189.

DeFelipe J (1997) Types of neurons, synaptic connections and chemical characteristics of cells immunoreactive for calbindin-D28K, parvalbumin and calretinin in the neocortex. J Chem Neuroanat 14:1–19.

DeFelipe J, Fariñas I (1992) The pyramidal neuron of the cerebral cortex: morphological and chemical characteristics of the synaptic inputs. Prog Neurobiol 39:563–607.

DeFelipe J, González-Albo MC, Del Río MR, Elston GN (1999) Distribution and patterns of connectivity of interneurons containing calbindin, calretinin, and parvalbumin in visual areas of the occipital and temporal lobes of the macaque monkey. J Comp Neurol 412:515–526.

Douglas RJ, Koch C, Mahowald M, Martin KA, Suarez HH (1995) Recurrent excitation in neocortical circuits. Science 269:981–985.

Dumitriu D, Cossart R, Huang J, Yuste R (2006) Correlation Between Axonal Morphologies and Synaptic Input Kinetics of Interneurons from Mouse Visual Cortex. Cerebral Cortex 17:81–91.

Dykes RW, Lamour Y, Diadori P, Landry P, Dutar P (1988) Somatosensory cortical neurons with an identifiable electrophysiological signature. Brain Res 441:45–58.

Enroth-Cugell C, Robson JG (1966) The contrast sensitivity of retinal ganglion cells of the cat. J Physiol (Lond) 187:517–552.
Enroth-Cugell C, Robson JG (1984) Functional characteristics and diversity of cat retinal ganglion cells. Basic characteristics and quantitative description. Invest Ophthalmol Vis Sci 25:250–267.
Fanselow EE, Richardson KA, Connors BW (2008) Selective, state-dependent activation of somatostatin-expressing inhibitory interneurons in mouse neocortex. J Neurophysiol 100:2640–2652.
Ferster D (1986) Orientation selectivity of synaptic potentials in neurons of cat primary visual cortex. J Neurosci 6:1284–1301.
Ferster D, Chung S, Wheat H (1996) Orientation selectivity of thalamic input to simple cells of cat visual cortex. Nature 380:249–252.
Ferster D, Miller KD (2000) Neural mechanisms of orientation selectivity in the visual cortex. Annu Rev Neurosci 23:441–471.
Finn IM, Priebe NJ, Ferster D (2007) The emergence of contrast-invariant orientation tuning in simple cells of cat visual cortex. Neuron 54:137–152.
Gentet LJ, Avermann M, Matyas F, Staiger JF, Petersen CCH (2010) Membrane potential dynamics of GABAergic neurons in the barrel cortex of behaving mice. Neuron 65:422–435.
Gentet LJ, Kremer Y, Taniguchi H, Huang ZJ, Staiger JF, Petersen CCH (2012) Unique functional properties of somatostatin-expressing GABAergic neurons in mouse barrel cortex. Nat Neurosci.
Gonchar Y, Burkhalter A (1997) Three distinct families of GABAergic neurons in rat visual cortex. Cereb Cortex 7:347–358.
Gonchar Y, Turney S, Price JL, Burkhalter A (2002) Axo-axonic synapses formed by somatostatin-expressing GABAergic neurons in rat and monkey visual cortex. J Comp Neurol 443:1–14.
Gonchar Y, Wang Q, Burkhalter A (2007) Multiple distinct subtypes of GABAergic neurons in mouse visual cortex identified by triple immunostaining. Frontiers in neuroanatomy 1:3.
Gray CM, Mccormick DA (1996) Chattering cells: superficial pyramidal neurons contributing to the generation of synchronous oscillations in the visual cortex. Science 274:109–113.
Gupta A, Wang Y, Markram H (2000) Organizing principles for a diversity of GABAergic interneurons and synapses in the neocortex. Science 287:273–278.
Hensch TK (2004) CRITICAL PERIOD REGULATION. Annu Rev Neurosci 27:549–579.
Hensch TK (2005) Critical period plasticity in local cortical circuits. Nat Rev Neurosci 6:877–888.
Hippenmeyer S, Vrieseling E, Sigrist M, Portmann T, Laengle C, Ladle DR, Arber S (2005) A developmental switch in the response of DRG neurons to ETS transcription factor signaling. PLoS Biol 3:e159.
Hirsch JA, Martinez LM, Pillai C, Alonso J-M, Wang Q, Sommer FT (2003) Functionally distinct inhibitory neurons at the first stage of visual cortical processing. Nat Neurosci 6:1300–1308.
Hofer SB, Ko H, Pichler B, Vogelstein J, Ros H, Zeng H, Lein E, Lesica NA, Mrsic-Flogel TD (2011) Differential connectivity and response dynamics of excitatory and inhibitory

neurons in visual cortex. Nat Neurosci 14:1045–1052.
Joshi S, Hawken MJ (2006) Loose-patch-juxtacellular recording in vivo--a method for functional characterization and labeling of neurons in macaque V1. J Neurosci Methods 156:37–49.
Kapfer C, Glickfeld LL, Atallah BV, Scanziani M (2007) Supralinear increase of recurrent inhibition during sparse activity in the somatosensory cortex. Nature Publishing Group 10:743–753.
Kawaguchi Y, Kubota Y (1996) Physiological and morphological identification of somatostatin- or vasoactive intestinal polypeptide-containing cells among GABAergic cell subtypes in rat frontal cortex. J Neurosci 16:2701–2715.
Kawaguchi Y, Kubota Y (1997) GABAergic cell subtypes and their synaptic connections in rat frontal cortex. Cereb Cortex 7:476–486.
Kerlin AM, Andermann ML, Berezovskii VK, Reid RC (2010) Broadly tuned response properties of diverse inhibitory neuron subtypes in mouse visual cortex. Neuron 67:858–871.
Kisvárday ZF, Eysel UT (1993) Functional and structural topography of horizontal inhibitory connections in cat visual cortex. Eur J Neurosci 5:1558–1572.
Kisvárday ZF, Ferecskó AS, Kovács K, Buzás P, Budd JML, Eysel UT (2002) One axon-multiple functions: specificity of lateral inhibitory connections by large basket cells. J Neurocytol 31:255–264.
Kubota Y, Hattori R, Yui Y (1994) Three distinct subpopulations of GABAergic neurons in rat frontal agranular cortex. Brain Res 649:159–173.
Kuhlman SJ, Huang ZJ (2008) High-resolution labeling and functional manipulation of specific neuron types in mouse brain by Cre-activated viral gene expression. PLoS ONE 3:e2005.
Lauritzen TZ, Miller KD (2003) Different Roles for Simple-Cell and Complex-Cell Inhibition in V1. J Neurosci 23:10201*10213.
Lewis DA, Hashimoto T, Volk DW (2005) Cortical inhibitory neurons and schizophrenia. Nat Rev Neurosci 6:312–324.
Liu B-H, Li P, Li Y-T, Sun YJ, Yanagawa Y, Obata K, Zhang LI, Tao HW (2009a) Visual receptive field structure of cortical inhibitory neurons revealed by two-photon imaging guided recording. J Neurosci 29:10520–10532.
Liu B-H, Li P, Li Y-T, Sun YJ, Yanagawa Y, Obata K, Zhang LI, Tao HW (2009b) Visual receptive field structure of cortical inhibitory neurons revealed by two-photon imaging guided recording. J Neurosci 29:10520–10532.
Lu CB, Yanagawa Y, Henderson Z (2010) Properties of gamma frequency oscillatory activity induced in hippocampal slices from the adult GAD67-GFP (Deltaneo) mouse. Brain Res 1323:65–73.
Ma W-P, Liu B-H, Li Y-T, Huang ZJ, Zhang LI, Tao HW (2010) Visual representations by cortical somatostatin inhibitory neurons--selective but with weak and delayed responses. J Neurosci 30:14371–14379.
Ma Y, Hu H, Berrebi AS, Mathers PH, Agmon A (2006) Distinct subtypes of somatostatin-containing neocortical interneurons revealed in transgenic mice. J Neurosci 26:5069–5082.
Majewska A, Yiu G, Yuste R (2000) A custom-made two-photon microscope and deconvolution system. Pflugers Arch 441:398–408.

Mansour A, Fox CA, Akil H, Watson SJ (1995) Opioid-receptor mRNA expression in the rat CNS: anatomical and functional implications. Trends Neurosci 18:22–29.
Mariño J, Schummers J, Lyon DC, Schwabe L, Beck O, Wiesing P, Obermayer K, Sur M (2005) Invariant computations in local cortical networks with balanced excitation and inhibition. Nat Neurosci 8:194–201.
Markram H, Toledo-Rodriguez M, Wang Y, Gupta A, Silberberg G, Wu C (2004) Interneurons of the neocortical inhibitory system. Nat Rev Neurosci 5:793–807.
McGarry LM, Packer AM, Fino E, Nikolenko V, Sippy T, Yuste R (2010) Quantitative classification of somatostatin-positive neocortical interneurons identifies three interneuron subtypes. Front Neural Circuits 4:12.
Monier C, Chavane F, Baudot P, Graham LJ, Fregnac Y (2003) Orientation and direction selectivity of synaptic inputs in visual cortical neurons: A diversity of combinations produces spike tuning. Neuron 37:663–680.
Nelson S, Toth L, Sheth B, Sur M (1994) Orientation selectivity of cortical neurons during intracellular blockade of inhibition. Science 265:774–777.
Niell CM, Stryker MP (2008) Highly Selective Receptive Fields in Mouse Visual Cortex. J Neurosci 28:7520–7536.
Niell CM, Stryker MP (2010) Modulation of visual responses by behavioral state in mouse visual cortex. Neuron 65:472–479.
Nowak LG, Sanchez-Vives MV, McCormick DA (2008) Lack of orientation and direction selectivity in a subgroup of fast-spiking inhibitory interneurons: cellular and synaptic mechanisms and comparison with other electrophysiological cell types. Cereb Cortex 18:1058–1078.
Ohki K, Reid RC (2007) Specificity and randomness in the visual cortex. Curr Opin Neurobiol 17:401–407.
Palmer SE, Miller KD (2007) Effects of inhibitory gain and conductance fluctuations in a simple model for contrast-invariant orientation tuning in cat V1. J Neurophysiol 98:63–78.
Parra P, Gulyás AI, Miles R (1998) How many subtypes of inhibitory cells in the hippocampus? Neuron 20:983–993.
Poo C, Isaacson JS (2009) Odor representations in olfactory cortex: "sparse" coding, global inhibition, and oscillations. Neuron 62:850–861.
Priebe NJ, Ferster D (2008) Inhibition, spike threshold, and stimulus selectivity in primary visual cortex. Neuron 57:482–497.
Rubenstein JLR, Merzenich MM (2003) Model of autism: increased ratio of excitation/inhibition in key neural systems. Genes Brain Behav 2:255–267.
Runyan CA, Schummers J, Van Wart A, Kuhlman SJ, Wilson NR, Huang ZJ, Sur M (2010) Response features of parvalbumin-expressing interneurons suggest precise roles for subtypes of inhibition in visual cortex. Neuron 67:847–857.
Sceniak MP, Ringach DL, Hawken MJ, Shapley R (1999) Contrast's effect on spatial summation by macaque V1 neurons. Nat Neurosci 2:733–739.
Shapley R, Lennie P (1985) Spatial frequency analysis in the visual system. Annu Rev Neurosci 8:547–583.
Silberberg G, Markram H (2007) Disynaptic inhibition between neocortical pyramidal cells mediated by Martinotti cells. Neuron 53:735–746.
Sillito AM (1975) The contribution of inhibitory mechanisms to the receptive field

properties of neurones in the striate cortex of the cat. J Physiol (Lond) 250:305–329.
Sohya K, Kameyama K, Yanagawa Y, Obata K, Tsumoto T (2007) GABAergic neurons are less selective to stimulus orientation than excitatory neurons in layer II/III of visual cortex, as revealed by in vivo functional Ca2+ imaging in transgenic mice. J Neurosci 27:2145–2149.
Somers DC, Nelson SB, Sur M (1995) An emergent model of orientation selectivity in cat visual cortical simple cells. J Neurosci 15:5448–5465.
Somogyi P, Kisvárday ZF, Martin KA, Whitteridge D (1983) Synaptic connections of morphologically identified and physiologically characterized large basket cells in the striate cortex of cat. Neuroscience 10:261–294.
Sompolinsky H, Shapley R (1997) New perspectives on the mechanisms for orientation selectivity. Curr Opin Neurobiol 7:514–522.
Stepanyants A, Martinez LM, Ferecskó AS, Kisvárday ZF (2009) The fractions of short- and long-range connections in the visual cortex. Proc Natl Acad Sci USA 106:3555–3560.
Swadlow HA (2003) Fast-spike interneurons and feedforward inhibition in awake sensory neocortex. Cereb Cortex 13:25–32.
Tamamaki N, Yanagawa Y, Tomioka R, Miyazaki J-I, Obata K, Kaneko T (2003) Green fluorescent protein expression and colocalization with calretinin, parvalbumin, and somatostatin in the GAD67-GFP knock-in mouse. J Comp Neurol 467:60–79.
Tan AYY, Brown BD, Scholl B, Mohanty D, Priebe NJ (2011) Orientation selectivity of synaptic input to neurons in mouse and cat primary visual cortex. J Neurosci 31:12339–12350.
Tan Z, Hu H, Huang ZJ, Agmon A (2008) Robust but delayed thalamocortical activation of dendritic-targeting inhibitory interneurons. Proc Natl Acad Sci USA 105:2187–2192.
Taniguchi H, He M, Wu P, Kim S, Paik R, Sugino K, Kvitsani D, Fu Y, Lu J, Lin Y, Miyoshi G, Shima Y, Fishell G, Nelson SB, Huang ZJ (2011) A Resource of Cre Driver Lines for Genetic Targeting of GABAergic Neurons in Cerebral Cortex. Neuron 71:995–1013.
Vruwink M, Schmidt HH, Weinberg RJ, Burette A (2001) Substance P and nitric oxide signaling in cerebral cortex: anatomical evidence for reciprocal signaling between two classes of interneurons. J Comp Neurol 441:288–301.
Wang X-J, Tegnér J, Constantinidis C, Goldman-Rakic PS (2004) Division of labor among distinct subtypes of inhibitory neurons in a cortical microcircuit of working memory. Proc Natl Acad Sci USA 101:1368–1373.
Wang Y, Gupta A, Toledo-Rodriguez M, Wu CZ, Markram H (2002) Anatomical, physiological, molecular and circuit properties of nest basket cells in the developing somatosensory cortex. Cereb Cortex 12:395–410.
Wehr M, Zador AM (2003) Balanced inhibition underlies tuning and sharpens spike timing in auditory cortex. Nature 426:442–446.
Xu X, Roby KD, Callaway EM (2010) Immunochemical characterization of inhibitory mouse cortical neurons: three chemically distinct classes of inhibitory cells. J Comp Neurol 518:389–404.
Yazaki-Sugiyama Y, Kang S, Câteau H, Fukai T, Hensch TK (2009) Bidirectional plasticity in fast-spiking GABA circuits by visual experience. Nature 462:218–221.
Yoshimura Y, Callaway EM (2005) Fine-scale specificity of cortical networks depends on inhibitory cell type and connectivity. Nat Neurosci 8:1552–1559.
Zaitsev AV, Gonzalez-Burgos G, Povysheva NV, Kröner S, Lewis DA, Krimer LS (2005)

Localization of calcium-binding proteins in physiologically and morphologically characterized interneurons of monkey dorsolateral prefrontal cortex. Cereb Cortex 15:1178–1186.

Zariwala HA, Madisen L, Ahrens KF, Bernard A, Lein ES, Jones AR, Zeng H (2011) Visual Tuning Properties of Genetically Identified Layer 2/3 Neuronal Types in the Primary Visual Cortex of Cre-Transgenic Mice. Front Syst Neurosci 4:1–16.

Zhang LI, Tan AYY, Schreiner CE, Merzenich MM (2003) Topography and synaptic shaping of direction selectivity in primary auditory cortex. Nature 424:201–205.

Chapter 3: Tight coupling of structure and function in cortical inhibitory neurons

3.1 Summary

Whether and how the properties of inhibitory neurons in the mouse primary visual cortex (V1) relate to their local circuit remains unclear. In order to understand the distribution and origins of orientation selectivity in inhibitory neurons expressing the calcium binding protein parvalbumin (PV), we specifically labeled PV+ neurons with red fluorescent protein (RFP), and targeted a large number of these neurons for cell-attached electrophysiological recordings. PV+ neurons had a bimodal distribution of orientation selectivity, including a large group of broadly tuned PV+ neurons and a smaller group of highly tuned PV+ neurons. The dendritic morphology of PV+ cells, revealed by intracellular labeling, was strongly correlated with their tuning: highly tuned PV+ neurons had dendrites with shorter total length that branched near the soma, while broadly tuned PV+ neurons had dendrites with longer length that branched farther from the soma. High-speed two-photon calcium imaging of visual responses of V1 neuronal populations showed that the orientation preferences of highly tuned PV+ neurons resembled the preferred orientations of neighboring cells, and that the orientation selectivity of PV+ neurons was inversely correlated with the local orientation scatter. These results suggest that the diversity of the local neighborhood and the nature of dendritic sampling both contribute to the response selectivity of PV+ neurons.

3.2 Introduction

Inhibition has many roles in cortical circuits (Ferster and Miller, 2000; Wehr and Zador, 2003; Mariño et al., 2005; Priebe and Ferster, 2008; Cardin et al., 2009), and this diversity of function matches the diversity of the inhibitory neuron population in cortex. Inhibitory neuron subclasses differ in their gene expression, axonal projection patterns, dendritic morphology, and electrophysiological properties, suggesting that specific

subtypes may perform specific functions (Lund and Lewis, 1993; Kubota et al., 1994; Markram et al., 2004; Krimer et al., 2005).

This diversity has complicated the study of inhibitory neurons, however. Even parvalbumin-positive (PV+) cells, often considered as one distinct inhibitory cell type, are heterogeneous across all of these parameters. With respect to morphology and targets, PV+ cells include soma-targeting basket cells with small and large dendritic and axonal fields, axon-targeting chandelier cells, and dendrite-targeting multipolar bursting cells (Kisvárday and Eysel, 1993; Lund and Lewis, 1993; Han, 1994; Wang et al., 2002; Blatow et al., 2003; Krimer et al., 2005; Zaitsev et al., 2009). PV+ neurons also vary in expression of potassium channel subunits (Du et al., 1996; Chow et al., 1999), calcium binding proteins (Chow et al., 1999; Blatow et al., 2003), and other signaling molecules and receptors (Vruwink et al., 2001); (Yan et al., 1998). Across these subgroups, most PV+ neurons show fast-spiking behavior; however, PV+ neurons with regular-spiking and stuttering phenotypes have also been described (Han, 1994; Blatow et al., 2003; Markram et al., 2004; Krimer et al., 2005).

The PV+ population is also functionally diverse; in the mouse visual cortex (V1) these cells have receptive fields that range from unselective to highly selective for orientation tuning and other response features (Runyan et al., 2010; Hofer et al., 2011; Zariwala et al., 2011) (but see Sohya et al., 2007; Liu et al., 2009; Kerlin et al., 2010). The origins of PV+ neuron tuning remain unresolved but might depend on the specificity of local inputs. The salt-and-pepper organization of orientation preferences in mouse V1 (Ohki and Reid, 2007), coupled with uniformly sampled inputs from the orientation map, could provide broad orientation tuning to PV+ cells, whereas narrow tuning would require precise connections from cells with a particular orientation preference to a given PV+ neuron. On the other hand, small homogeneities in the orientation representation (Dräger, 1975), coupled with matched dendritic arbors of a subset of PV+ neurons, could enable these neurons to achieve narrow tuning by uniform sampling of the local neighborhood alone.

In this study, we recorded from a large number of PV+ neurons and found a bimodal distribution that included highly tuned and broadly tuned neurons. We compared the dendritic arbors of PV+ neurons with a range of tuning, and examined the spatial distribution of orientation preferences of nearby cells. We found that highly tuned PV+

neurons have shorter dendrites with the majority of branching occurring closer to the soma, while broadly tuned PV+ neurons have longer, more tortuous dendrites. Furthermore, the orientation selectivity of highly tuned PV+ neurons matches the tuning of nearby cells, suggesting that these neurons may sample uniformly from local inputs, yet the morphology of their dendritic arbors may influence their response selectivity by restricting the diversity of local inputs they sample.

3.3 Experimental Procedures

3.3.1 Mice

Experiments were carried out in mice under protocols approved by MIT's Animal Care and Use Committee and conformed to NIH guidelines. Heterozygous PV-Cre knock-in driver mice, which express Cre in over 90% of PV+ neurons, were backcrossed into a C57BL/6 line (Hippenmeyer et al., 2005). Thy1-GFP-S mice (Feng et al., 2000) were also maintained on a C57BL/6 line.

3.3.2 Viral Construct and Injection

RFP was expressed in Parvalbumin+ (PV+) interneurons in the visual cortex of PV-Cre mice by infection of a LS_2L-RFP construct packaged into adeno-associated virus (AAV, serotype 2/9) as described previously (Kuhlman and Huang, 2008; Runyan et al., 2010). Six-week old PV-Cre mice were initially anesthetized with 4% isoflurane in oxygen, and maintained on 2% isoflurane. The skull was thinned along a 1mm line at the rostral edge of V1, and the remaining skull and dura mater were carefully punctured using a glass micropipette filled with the virus. Two injections (0.25μl of virus, injected at 10nl/min) were made at each site, at depths of 500μm and 250μm respectively. After each injection, the pipette was held in place for five minutes prior to retraction to prevent leakage.

3.3.3 Animal Preparation

Two-four weeks post-injection, mice were anesthetized with a cocktail containing Fentanyl (0.05mg/kg), Midazolam (5mg/kg), and Medetomidine (0.5mg/kg),

supplemented with isoflurane. The eyes were protected with ophthalmic ointment during the surgery, and moistened afterward with saline. A metal head plate was attached to the skull parallel to V1 using cyanoacrylate glue and dental acrylic. A 2mm x 2mm craniotomy was performed over V1, and the exposed area was covered with a thin layer of 2% agarose in ACSF (140mM NaCl, 5mM KCl, 2mM $CaCl_2$, 1mM $MgCl_2$, .01mM EDTA, 10mM HEPES, 10mM Glucose, pH 7.4).

Mice were then transferred to a custom-built two-photon microscope (Majewska et al., 2000) that was powered by a Spectra Physics Mai-Tai eHP laser, passed through a Deep-See module (Spectra Physics / Newport), where the head plate was screwed into a moveable stage. To maintain anesthesia, 0.5% isoflurane in oxygen was supplied through a tube, and Fentanyl/Medetomidine was injected every hour. The body temperature was maintained at 37.5ºC with heating pads. The recording phase of physiology experiments typically lasted for 6-12 hours.

3.3.4 Targeted Cell-attached Recording

Glass pipettes with ~1.5μm tip size and 3-7MΩ resistance were filled with Alexa Fluor 488 (5μM in saline, Molecular Probes, Eugene, OR) and introduced into the pia above the viral injection site (at a 21-degree angle) using a micromanipulator (Sutter, MP-285) under visual guidance with epifluorescence. Upon entering the brain, the pipette was guided toward RFP+ cells in superficial layer 2/3 of V1 under two-photon guidance. The laser was tuned to 920nm, which allowed excitation of both the Alexa 488 and RFP fluorophores simultaneously. The pipette was targeted to RFP+ cells while applying constant positive pressure (0.2 psi), which was monitored with a digital pressure gauge (General Tools). When the pipette was just touching the cell surface, positive pressure was released, and sustained negative pressure immediately applied (0.2-0.6 psi) to obtain a loose seal (Joshi and Hawken, 2006). If well-isolated spikes were detected during the display of a drifting grating that randomly changed orientation and direction at 8 Hz, then the cell's orientation selectivity was assessed. Subsequently, current pulses (35ms, 900-2000nA) were delivered at 15 Hz for 30-60 seconds to fill the recorded cell through electroporation. Only single RFP+ cells that were distinctly filled during this procedure were included for analysis. In the same experiments, RFP- cells were targeted blindly. As

the tip was slowly advanced through the cortex, -0.5nA current pulses were delivered for 6.3ms at .55 Hz, and the tip resistance was monitored. When the tip resistance increased substantially, positive pressure was released, and negative pressure immediately applied, as above. The location of the tip was still monitored under two-photon guidance; all RFP- cells were located within the injection site and were also filled after recording. Recordings from GFP+ pyramidal neurons in Thy1-GFP-S mice were carried out similarly. Neurons in PV-Cre or Thy1 mice were recorded at depths of 100-300 um. Recordings were made with an Axoclamp-2A amplifier (Axon Instruments) using Clampex software (Axon Instruments, v8.1) at a sampling rate of 30 KHz.

3.3.5 Two-photon structural imaging

The laser was tuned to 920nm, allowing strong excitation of GFP, RFP, and Alexa 488. Images were collected through a high performance objective lens (25x Olympus XL Plan N objective, NA= 1.05). Z-stacks were collected at 2μm increments from the pial surface through the extent of the filled cell, at resolution of 0.4μm/pixel, spanning 200μm in x and y dimensions, using FluoView300 confocal imaging software (Olympus), on both the red (RFP+) and green (Alexa 488 dye) channels. In all filled cells, the signal on red and green channels overlapped throughout all processes, and PMT gain was optimized to visualize the finest processes.

3.3.6 Two-photon calcium imaging

For these experiments, we used a Prairie Ultima two-photon system (Prairie Technologies) driven by a Spectra Physics Mai-Tai eHP laser, passed through a Deep-See module (Spectra Physics / Newport). The excitation laser was tuned to 920nn, and functional imaging was done through a high performance objective lens (25x Olympus XL Plan N objective, NA= 1.05).

A glass pipette filled with Oregon Green Bapta-1 AM (OGB1-AM, 1.0mM, Molecular Probes, Eugene, OR) and Alexa Fluor 594 (100μM, Molecular Probes, Eugene, OR) was visually guided into the brain and lowered to a depth between 100 and 200μm below the surface, near the center of the viral injection site, and a small amount of dye was released

using a picospritzer. The brain was then left undisturbed for at least one hour before imaging.

We used a custom software system to measure changes in the calcium indicator fluorescence in response to visual stimuli. Imaging first included a raster scan to identify cell positions, and machine vision algorithms were used to identify cell bodies. Next, an algorithm was used to identify the shortest scan path between cells (Lillis et al., 2008), and this scan path was run at 50Hz, with a 90% dwell time inside the cells.

3.3.7 Visual Stimulation

Visual stimuli were displayed on a 17-inch LCD monitor placed 15cm from the eyes. Stimuli were generated in Matlab (Mathworks, Natick, MA) using the PsychoPhysics Toolbox (Brainard, 1997). Square wave drifting gratings with 100% contrast were used. In targeted cell-attached recordings, spatial frequency and temporal frequency were optimized to achieve the highest firing rate for each cell: spatial frequency ranged from 0.005 to 0.05 cycles per degree (cpd), and temporal frequency ranged from 1 to 3 cycles per second (cps). Test stimuli were episodically presented, equally alternating with a blank gray screen, with 8-second cycles (4 sec on, 4 sec off) at each of 18 directions.

3.3.8 Data Analysis: Visual Responses

Analysis of all data was carried out offline with custom-written Matlab routines. Electrophysiological time traces were imported into Matlab, smoothed with a Gaussian kernel, and spikes were identified by detection of events based on the derivative of the voltage traces. The spontaneous firing rate of each neuron was measured for 10 seconds preceding visual stimulation for each trial. A neuron was considered visually responsive if its firing rate at the preferred orientation was significantly higher than its spontaneous firing rate, determined with a t-test. The spontaneous firing rate was then subtracted from the response to each orientation, the mean firing rate across the entire 4-second stimulus interval. The response firing rates were then fit to a Gaussian function.

Fluorescence time traces were assigned to the appropriate cell location, to obtain a time trace sampled at 50Hz. The response ($\Delta F/F$) was calculated for each orientation by subtracting and then dividing the maximum fluorescence value during the grating

presentation by the mean fluorescence during the preceding blank (Schummers et al., 2008; Runyan et al., 2010).

Responses (either spike rates or ΔF/F values) were then fit with a circular Gaussian function in order to estimate the preferred orientation and tuning width (half-width at half-height). The orientation selectivity index (OSI) was calculated as the vector average of responses in the preferred direction (Schummers et al., 2002). Statistical comparisons were carried out using the Wilcoxon test, two-tailed t-test, and the Kolmogorov-Smirnoff test and yielded indistinguishable results. Values from two-tailed t-tests are reported under Results.

In the population calcium imaging datasets, the spatial arrangement of orientation preferences was assessed by calculating the local orientation scatter, or the mean difference in the preferred orientations of each cell and neighboring cells within 30, 60, or 120μm. This mean difference was compared between RFP+ cells and their neighbors and RFP- cells and their neighbors. The OSI values in this data set were normalized to the maximum OSI to estimate the relative orientation selectivity. In order to test the validity of the difference between the orientation mapping around RFP+ and RFP- neurons, a bootstrap procedure with 10,000 samples was used to estimate the orientation mapping in the randomized configuration, where the orientation preferences were resampled among the cells' spatial locations with replacement, and the local scatter around each cell was recalculated in each scrambled iteration (Dombeck et al., 2009).

3.3.9 Morphological Reconstructions

Neurons were reconstructed from z-stacks that were collected *in vivo,* as described above, using V3D semi-automatic tracing software (Peng et al., 2010). The multi-TIF 16-bit image stacks collected within the FluoView software were converted to high contrast 8-bit images within ImageJ software, and then imported into V3D. The contrast of each image was enhanced to allow the tracing of each thin dendritic process. Both the red (RFP+) and green (Alexa 488) channels were used to follow all of the neuron's major and minor processes from the soma. Within the V3D software, stacks were carefully scrolled through to distinguish each process and to mark each insertion, branch, and tip location. The

maximum soma diameter was measured in the x, y, and z axes; the mean diameter is reported as the soma size.

The 3-dimensional coordinates of the soma, dendritic insertion points, dendritic branches, and dendritic tips were then exported to Matlab, where custom-written software was used for the Sholl analysis (Gutierrez and Davies, 2007). For each neuron, the Sholl profile was fit to a Gaussian function, from which the peak number of crossings (amplitude), distance of the peak from the soma (displacement), and Sholl radius (half-width at half-height) were extracted. The polarity of the dendritic branching was assessed as follows. The direction of each branch and tip relative to the soma in each of the 3 cardinal planes was measured. In each plane, a dendritic polarity index (DPI) was then calculated by vector averaging the distances of the tips and branches around the soma. The area of the dendritic field was measured as the area of the polygon containing the distal dendritic tips as each vertex.

RFP+ neurons from brains of PV-Cre mice were reconstructed in vitro for comparison with the in vivo reconstructions using the RFP label. Coronal slices were collected at 100μm thickness, mounted on slides, and coverslipped. Z-stacks were collected at 1μm optical slices at 4μm per pixel on a Zeiss LSM 5 Pascal Exciter confocal microscope with the 543 laser line (RFP+ fluorophore), and neurons were reconstructed as above.

3.4 Results

3.4.1 Electrophysiological Properties of PV+ Neurons

We specifically expressed red fluorescent protein (RFP) in parvalbumin-positive (PV+) inhibitory interneurons in heterozygous PV-Cre knock-in mice (Kuhlman and Huang, 2008; Runyan et al., 2010), and used two-photon targeted cell-attached recording (Figure 3.1A) to record from 74 visually responsive RFP+ neurons and 34 visually responsive RFP- neurons in V1 of 27 PV-Cre mice. The spike shapes of the RFP+ and RFP- neurons were highly distinguishable (Figure 3.1B,C): the RFP+ neurons had narrower spike widths (RFP+: 3.0msec $\pm$ 0.018 s.d.; RFP-: 3.3msec $\pm$ 0.011 s.d.; $p < 0.05$, two-tailed two-sample t-

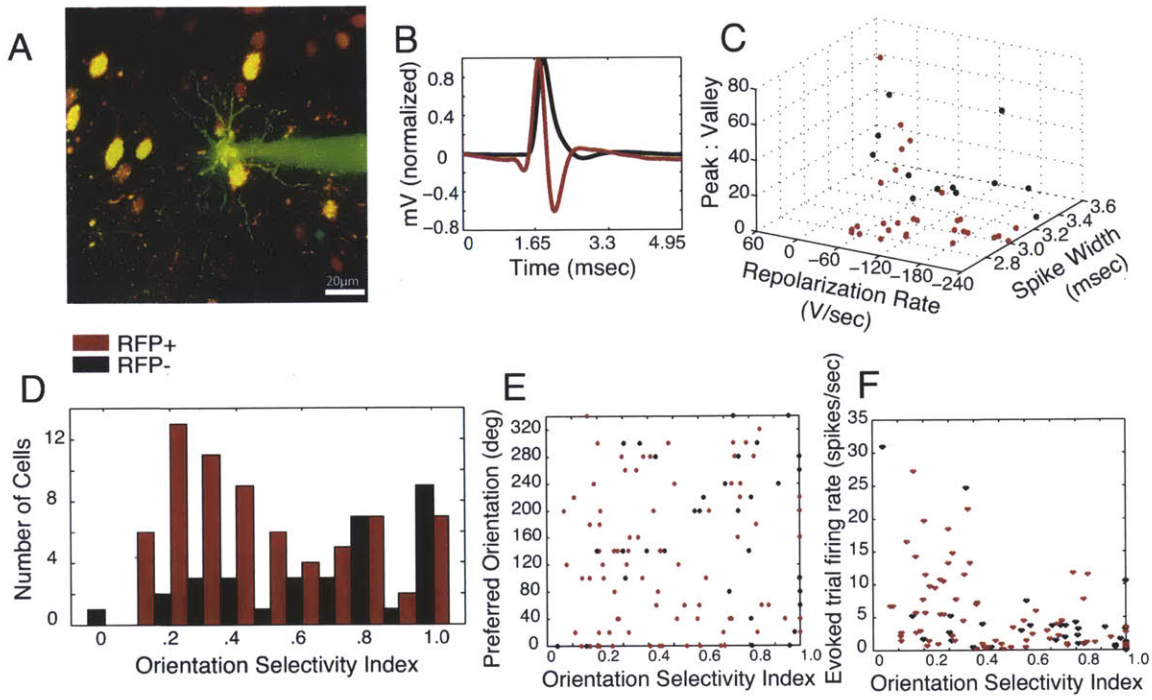

Figure 3.1. Targeted cell-attached recordings from RFP+ neurons reveal a range of orientation selectivity. (A) RFP+ neurons were targeted for cell-attached recordings under two-photon guidance, with a patch pipette containing green dye (Alexa 488). After recording, each cell was electroporated with the dye, and a z-stack was collected through the extent of the dendritic tree to enable morphological reconstruction. The example shown is an extended depth of focus montage of a z-stack taken of an electroporated RFP+ neuron in vivo after its orientation selectivity was characterized. Scalebar = 20μm (B) Spikes recorded from RFP+ neurons (red) and RFP- neurons (black) were averaged and normalized by their maximum voltage. Spikes recorded from the RFP+ neurons showed the characteristic shape of fast-spiking PV+ neurons, including a strong afterhyperpolarization. (C) The spike shapes of RFP+ neurons and RFP- neurons were distinct. The ratio of peak to valley amplitude ($p<.05$), repolarization rate ($p>.1$), and spike width ($p<.01$) are plotted for RFP+ and RFP- neurons. (D) The histogram of the distribution of orientation selectivity indices (OSIs) of RFP+ (red) and RFP- (black) neurons reveals that the distribution of orientation selectivity of RFP+ neurons was multimodal. Because of a large group of untuned RFP+ neurons, the mean orientation selectivity index (OSI) of RFP+ neurons was lower than that of RFP- neurons ($p<.05$); however, a second mode centered around OSI = 0.8 in the RFP+ distribution suggests a second subtype of PV+ neurons with high selectivity. (E) The preferred orientations of recorded RFP+ and RFP- neurons did not depend on their orientation selectivity (RFP+: $r = 0.075$, $p = 0.49$; RFP-: $r = 0.096$, $p = 0.60$). (F) The orientation selectivity and visually-evoked firing rate at the preferred orientation were strongly related in both RFP+ and RFP- neurons. The most highly tuned neurons had the lowest evoked firing rates (RFP+: $r = -0.44$, $p < .001$, RFP-: $r = -0.51$, $p < 0.01$).

test here and below), smaller peak:valley amplitudes (RFP+: 7.91 ± 16.81; RFP-: 21.52 ± 20.08; $p < 0.05$), but similar repolarization rates (RFP+: 107.27V/sec ± 69.39; RFP-: 105.45V/sec ± 75.45, $p = 0.76$). The spontaneous firing rate was higher in the RFP+ neurons (RFP+: 1.3Hz ± 2.2; RFP-: 0.4Hz ± 0.9; $p < 0.05$), which also had a nonsignificant trend toward higher evoked firing rates (RFP+: 7.5Hz ± 7.5; RFP-: 5.3 ± 8.1; $p = 0.13$).

3.4.2 Tuning Properties of PV+ Neurons

While the response features of PV+ neurons have been previously described by us (Chapter 2, Runyan et al., 2010) and others (Liu et al., 2009; Kerlin et al., 2010; Hofer et al., 2011; Zariwala et al., 2011), we aimed in this study to carefully evaluate the orientation selectivity of a large population of these neurons, and compare their morphological features to their response selectivity. For each neuron we measured the response to 18 drifting gratings in 20-degree increments, and calculated an orientation selectivity index (OSI) by vector averaging the response; the OSI can range from 0 (unselective for orientation) to 1 (responsive to only one orientation). On average, the OSIs were lower in the RFP+ population (RFP+: 0.4804 ± 0.2815, n=74; RFP-: 0.6767 ± 0.2882, n=34; $p < 0.05$). However, the OSI distribution in the RFP+ PV+ population appeared to be bimodal (Figure 3.1D), suggesting that the PV+ population could include at least two functional subtypes: highly tuned cells with OSIs centered near 0.8 and broadly tuned cells with OSIs centered near 0.3. All recorded RFP+ cells were located between 115 and 300μm below the pial surface (mean depth 173 ± 70μm), and soma depth and orientation selectivity were not correlated ($r = 0.18$, $p = 0.13$). Thus, it is unlikely that the highly selective PV+ neurons were a depth-based subclass such as multipolar bursting cells, a subclass of PV+ neurons that is located primarily at the border between layers I and II (Blatow et al., 2003), i.e. at typical depths of 90-100μm.

There was no correlation between the preferred orientation and OSI (Figure 3.1E; RFP+: $r = 0.075$, $p = 0.49$; RFP-: $r = 0.096$, $p = 0.60$). There was, however, a significant negative correlation between the firing rate at the preferred orientation and OSI in both RFP+ and RFP- neurons (Figure 3.1F), such that cells with the highest selectivity also had the lowest firing rates (RFP+: $r = -.44$, $p < 0.001$, RFP-: $r = -0.51$, $p < 0.01$). The negative relationship between orientation selectivity and visually-evoked firing rate suggests that

highly tuned neurons in mouse V1 may have fewer excitatory inputs than broadly tuned neurons.

3.4.3 Morphology of PV+ Neurons

After each cell's orientation response was characterized, it was filled with Alexa 488 (green) dye, and a detailed z-stack was collected through the extent of its dendritic tree on both the red and green channels. We examined the dendritic morphology of two types of cells: RFP+/PV+ inhibitory interneurons in PV-Cre mice and GFP+ pyramidal cells in Thy1-GFP-S mice.

We reconstructed 13 RFP+ neurons and 4 GFP+ pyramidal neurons. The orientation selectivity of reconstructed RFP+ neurons represented the full range of broadly tuned and highly tuned OSIs we described in Figure 3.1D (0.19 – 0.87). Examination of the reconstructions suggested that the dendritic morphology of RFP+ neurons varied systematically with orientation selectivity (Figure 3.2A, and also revealed clear differences in dendritic morphology between RFP+ and GFP+ neurons (Figure 3.2B). The RFP+ neurons seemed to have smaller and less complex dendritic arbors than GFP+ pyramidal neurons, and the sharply tuned PV+ neurons appeared to have shorter total dendrites than the broadly tuned PV+ neurons.

As a group (Figure 3.3A), the total dendritic length of RFP+ neurons was significantly shorter than that of GFP+ pyramidal neurons (RFP+: 2120 $\pm$ 1286μm, n=13; GFP+: 7681 $\pm$ 2794μm, n=4; $p<0.05$), as was the dendritic field (RFP+: 16440$\pm$5282μm^2; GFP+: 33222$\pm$9699μm^2). The soma diameters of RFP+ neurons were also significantly smaller than those of GFP+ neurons (RFP+ 18.5 $\pm$ 3.8μm; GFP+: 27.3 $\pm$ 12.2μm; $p < 0.05$). In order to assess the spatial extent of dendritic branching, we performed a Sholl analysis (Sholl, 1953; Gutierrez and Davies, 2007), in which we measured the number of processes crossing concentric spherical boundaries centered at the soma at 20μm increments. The Sholl profiles were characterized by four parameters: the radius of the profile, the distance of the peak from the soma, the peak number of Sholl intersections, and the total number of dendritic segments. Comparing the RFP+ and GFP+ pyramidal neuron groups, the radius of the Sholl profile (Figure 3.3B-C) tended to be smaller in the RFP+ population than in the

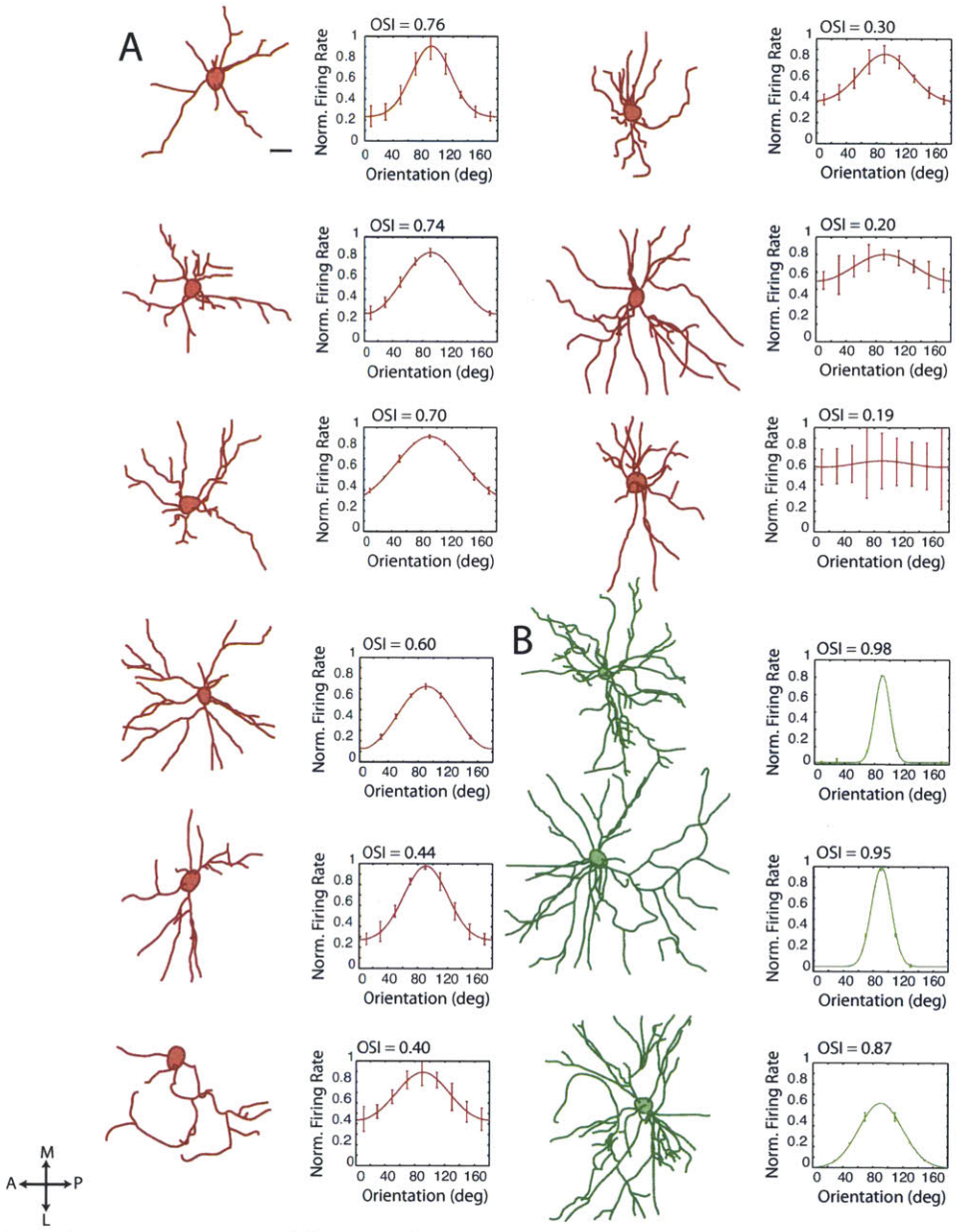

Figure 3.2: Relating structure and functional responses in RFP+/PV+ neurons and GFP+ pyramidal neurons. After each cell's orientation selectivity was characterized, it was intracellularly labeled and a two-photon z-stack was collected through its dendritic arbor. (A) Examples of reconstructed RFP+ neurons (left) and their orientation tuning curves (right), ordered by their orientation selectivity indices (OSI). Scale bar = 20μm and applies to all cells. (B) Examples of reconstructed GFP+ pyramidal neurons from the Thy1-GFP-S mice. Neuron reconstructions were flattened in the z-dimension for viewing purposes. Orientation responses were normalized to the peak firing rate and centered for ease of comparison. All neurons are oriented similarly. A = anterior, P = posterior, M = medial, L = lateral. Error bars on tuning curves indicate s.e.m.

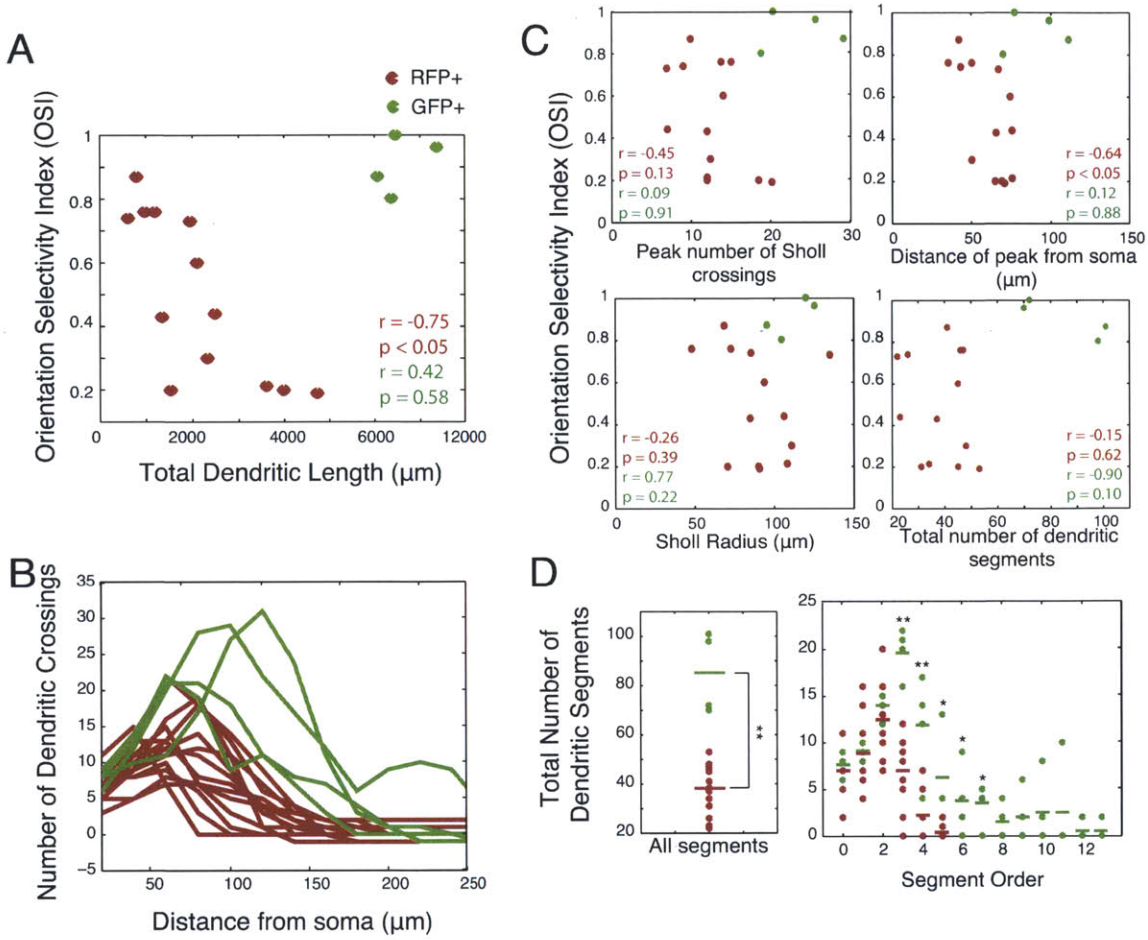

Figure 3.3. Dendritic morphology distinguishes PV+ neurons from pyramidal neurons, and several structural features of dendrites correlate with orientation selectivity in RFP+/PV+ neurons. (A) The total dendritic length was measured in 13 RFP+ neurons and 4 GFP+ pyramidal neurons, and compared to their orientation selectivity indices (OSIs). Dendritic length and OSI were strongly related in the RFP+ population ($r = -.75$, $p < .05$), while the dendritic lengths of GFP+ excitatory neurons (all highly tuned, OSI>0.7) were most similar to those of the untuned PV+ neurons. (B) Sholl analysis describes the spatial extent of dendritic branching, and the resulting Sholl profile indicated the number of dendritic processes crossing increasing distance boundaries from the soma. GFP+ pyramidal neurons (green) had more dendritic crossings with increasing distance than RFP+ neurons (red). (C) The Sholl profile was described by three parameters: its radius, the distance of its peak from the soma, and the peak number of crossings. Each parameter was compared to the OSI of each cell; the distance of the peak was significantly correlated with OSI in RFP+ neurons, while the peak number of crossings, Sholl radius, and the total number of dendritic segments were not significantly correlated to OSI in either RFP+ or GFP+ neurons. (D) The number of dendritic segments and distribution of segment rank (number of branches from the soma) provide a measure of dendritic branching complexity. The mean total number of segments and the number of higher order segments was higher in GFP+ pyramidal neurons than in RFP+ neurons, but did not differ as a function of OSI in RFP+ neurons as shown in (C). Lines indicate population means.

excitatory cells (RFP+: 59 ± 15μm; GFP+: 74 ± 9μm. P=0.09), and the peak number of intersections was lower in the RFP+ population (RFP+: 12.5 ± 3.9; GFP+: 23.5 ± 4.8, $p<0.05$). The peak number of intersections occurred closer to the soma in RFP+ neurons than in GFP+ neurons (RFP+: 60 ± 14μm; GFP+: 89 ± 19μm, $p<0.05$), and the total number of segments was lower in the RFP+ population (Figure 3.3D; RFP+: 38.3 ± 10.3; GFP+: 85.3 ± 16.5, $p<0.05$).

The total dendritic length was negatively correlated with orientation selectivity in RFP+ neurons ($r = -0.76$, $p < 0.001$), but not in GFP+ pyramidal neurons ($r = 0.42$, $p = 0.58$) (Figure 3.3A). However, the total area of the dendritic field did not correlate to the OSI in either group (RFP+: $r = -0.46$, $p = 0.22$; GFP+: $r = 0.009$, $p = 0.99$), nor did the soma size (RFP+: $r = 0.06$, $p = 0.84$; GFP+: $r = 0.007$, $p = 0.99$). The Sholl radius and peak number of Sholl crossings did not relate to tuning in RFP+ neurons (Figure 3.3C; radius: $r = -0.26$, $p = 0.39$; peak number of crossings: $r = -0.45$, $p = 0.13$) or GFP+ neurons (radius: $r = 0.77$, $p = 0.22$; peak number of crossings: $r = -0.09$, $p = 0.91$). The distance of the Sholl peak did significantly correlate to the OSI in RFP+ neurons ($r = -0.64$, $p < 0.05$) but not in GFP+ neurons ($r = 0.12$, $p = 0.88$). The total number of dendritic segments did not correlate to tuning in either cell type (RFP+: $r = -0.15$, $p = 0.62$; GFP+: $r = -0.90$, $p = 0.10$), nor did the number of primary segments (RFP+: $r = 0.32$, $p = 0.29$; GFP+: $r = 0.49$, $p = 0.51$), secondary segments (RFP+: $r = 0.01$, $p = 0.96$; GFP+: $r = 0.42$, $p = 0.58$), or higher order segments (RFP+: $r = -0.322$, $p = 0.28$; GFP+: $r = -0.09$, $p = 0.31$). Thus, PV+ neurons with different levels of orientation tuning have similar numbers of dendritic branches and branching complexity, but higher orientation selectivity of PV+ neurons correlates with shorter total dendritic length and shorter distance of maximal branching from the soma.

To assess whether the directionality of dendritic branching correlated with the orientation selectivity of RFP+ neurons, the angles of dendritic branches and tips from the soma were calculated in each of the three two-dimensional planes (Figure 3.4A; medial/lateral – anterior posterior, medial/lateral – dorsal/ventral, and dorsal/ventral – anterior/posterior). The polarity in each dimension was quantified by vector averaging, to obtain a Dendritic Polarity Index (DPI). The DPI was not correlated to orientation

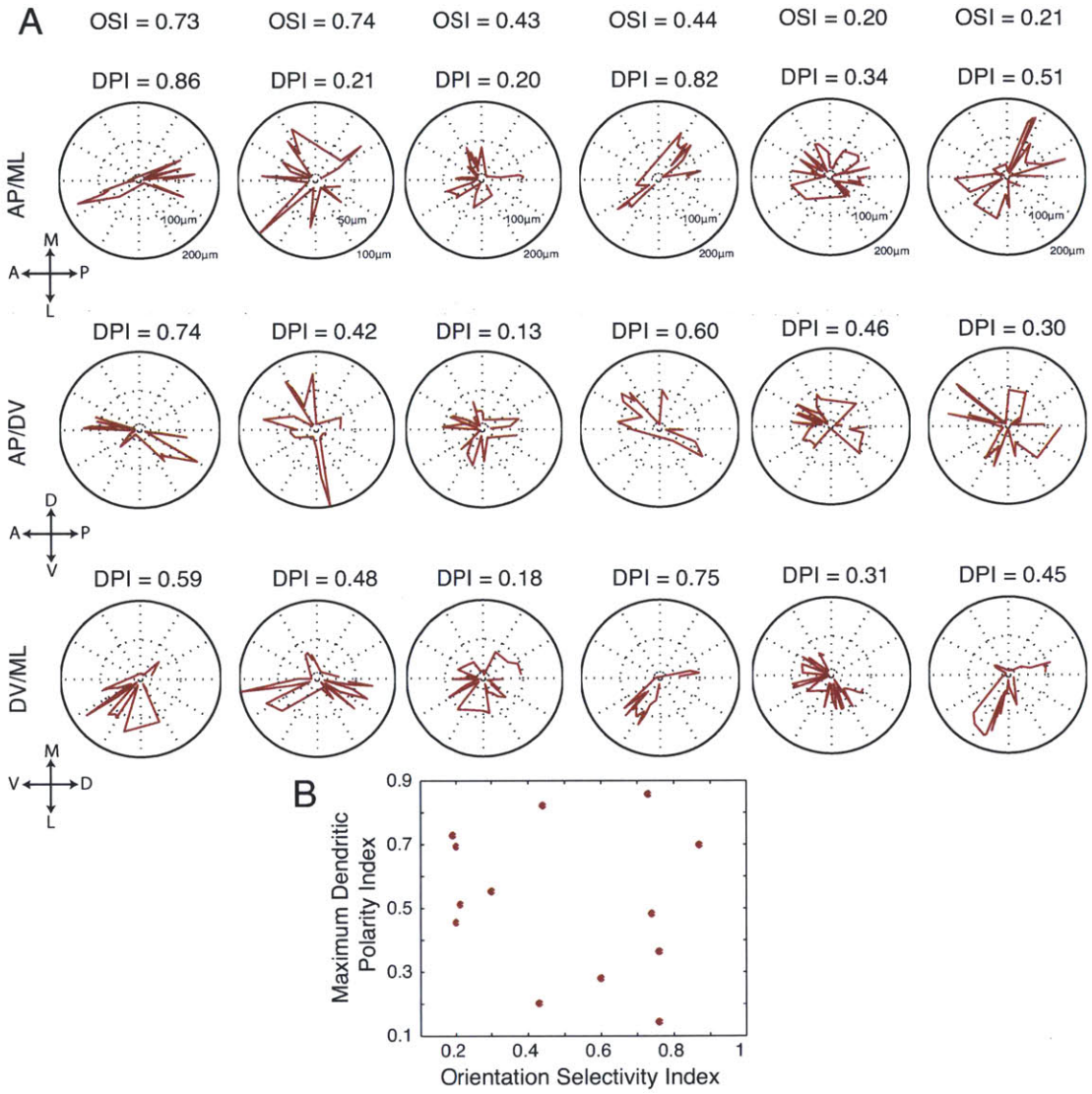

Figure 3.4. Dendritic polarity of RFP+ neurons is not related to their orientation selectivity. (A) Polar plots of the angle of each dendritic segment relative to the soma center for six representative RFP+ neurons in each of the three planes (AP/ML=anterior-posterior/medial-lateral, AP/DV=anterior-posterior/dorsal-ventral, and DV/ML=dorsal-ventral/medial-lateral). The Dendritic Polarity Index (DPI) was calculated in each dimension, as the vector average of the angle to and distance from the soma, and related to the orientation selectivity index (OSI) for each cell. (B) Although some neurons showed strong polarity in the direction of dendritic projections, no relationship was evident between the maximum dendritic polarity index (across the three dimensions) and OSI of RFP+ neurons ($r = -0.17$, $p = 0.57$).

selectivity, as both highly tuned and broadly tuned RFP+ neurons could have high DPIs ($r = -0.17$, $p = 0.57$) (Figure 3.4B).

Although our dendritic measurements in vivo are well within the ranges reported elsewhere for cortical basket cells (Helmstaedter et al., 2009; Zaitsev et al., 2009), we carried out a separate set of morphological measurements in vitro for comparison with the in vivo measurements. We sectioned V1 coronally, collected z-stacks of the RFP+ neurons *in vitro*, and reconstructed 8 RFP+ neurons in similar detail as those imaged *in vivo* (Figure 3.5). The Sholl profiles of the RFP+ neurons imaged *in vitro* were similar to the Sholl profiles of the RFP+ neurons imaged *in vivo* (Figure 3.5A), as were the total dendritic lengths (Figure 3.5B). None of the Sholl parameters (peak number of crossings: $p = 0.28$, distance of peak from soma: $p = 0.22$, profile radius: $p = 0.39$; for each comparison: n=8 RFP+ neurons imaged *in vitro*, n=13 RFP+ neurons imaged *in vivo*) nor the total dendritic length ($p = 0.98$) was significantly different between the data collected *in vivo* and *in vitro.*

3.4.4 Orientation Preference Maps of PV+ and PV- Neurons

We next examined the relationship between the tuning of PV+ neurons and their local neighborhood in the V1 orientation map. We used high-speed two-photon population calcium imaging in order to measure the orientation preferences of visually responsive PV+ neurons and their neighbors Figure 3.6A-C). 39 of 75 RFP+ PV+ neurons and 963 of 1405 RFP- neurons in four mice were visually responsive.

The preferred orientations of cells and their neighbors across the field of view were then compared (Figure 3.6C). In most networks, RFP+ cells with both high (Figure 3.6C, purple circles) and low (cyan circles) OSIs existed. The local orientation scatter was calculated surrounding each cell by measuring the difference between that cell's preferred orientation and those of the neighboring cells within 30, 60, or 120μm, and we compared the scatter surrounding RFP+ neurons and RFP- neurons (Figure 3.7A). The scatter was significantly lower surrounding RFP+ neurons than the scatter surrounding RFP- neurons; hence, RFP+ neurons tended to have similar orientation preferences to those of neighboring cells, while RFP- neurons did not. To validate this difference, we scrambled the orientation preferences among all of the cells in the field of view, maintaining their spatial locations and RFP+/RFP- identities, and again measured the scatter surrounding the

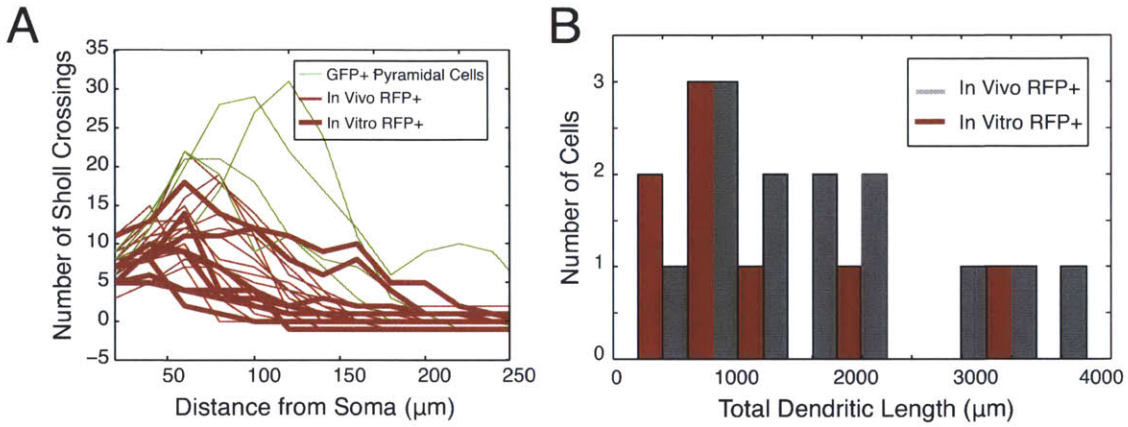

Figure 3.5. Comparison of in vitro morphological reconstructions of RFP+ neurons with in vivo reconstructions of physiologically characterized RFP+ neurons. (A) The Sholl profiles of the RFP+ PV+ neurons imaged in vitro (bold red), are superimposed on the in vivo data from Figure 3B. The in vitro Sholl profiles overlap extensively with the in vivo Sholl profiles. Peak number of crossings ($p = 0.28$), distance of the peak from the soma ($p = 0.22$), and radius ($p = 0.39$) of the Sholl profiles were statistically similar in the in vitro and in vivo imaged cells. (B) Histogram of the total dendritic length of RFP+ neurons imaged in vitro (red) and in vivo (gray). The total dendritic length was statistically similar ($p = 0.30$) between the two sets of cells. The morphological similarity between reconstructions of images taken in vivo and in vitro suggests that in vivo imaging fully captured the dendritic arbors of these neurons.

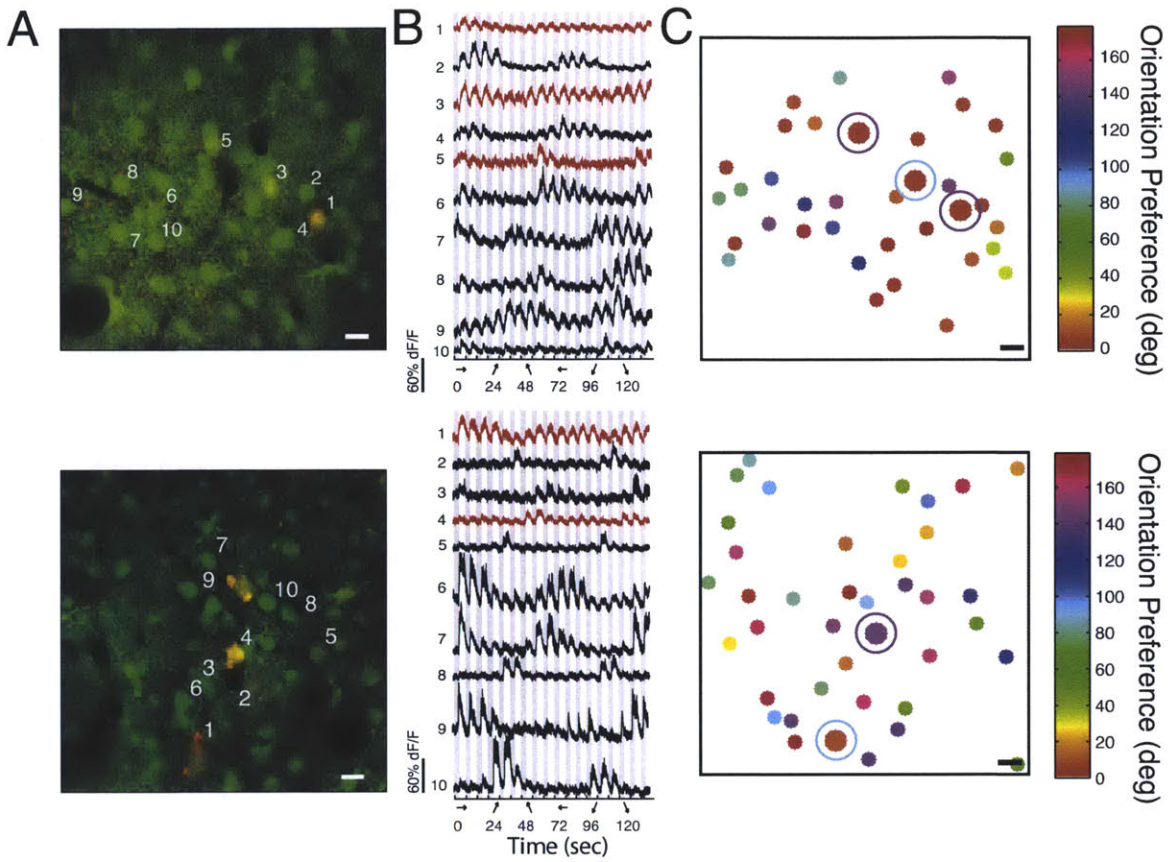

Figure 3.6. Two-photon calcium imaging allows mapping of orientation preference of RFP+ neurons and neighboring cells. (A) RFP+ neurons (red) and surrounding RFP- neurons were loaded with the calcium dye Oregon Green Bapta-1AM (OGB, green). Two such representative networks are shown (top and bottom). Scalebars = 10μm. (B) Example fluorescent responses to the 18 episodically presented drifting gratings (18 directions, gray: 4 seconds OFF and white: 4 seconds ON), from 10 cells in each of the two networks (Black: RFP- neuron responses, Red: RFP+ neuron responses). (C) Each tuned neuron has been color-coded by its preferred orientation. Smaller circles indicate RFP- neurons, and larger circles indicate RFP+ neurons. Color-coded ring around each RFP+ neuron indicates its strength of tuning: purple=high OSI, cyan=low OSI. Scalebars = 10μm.

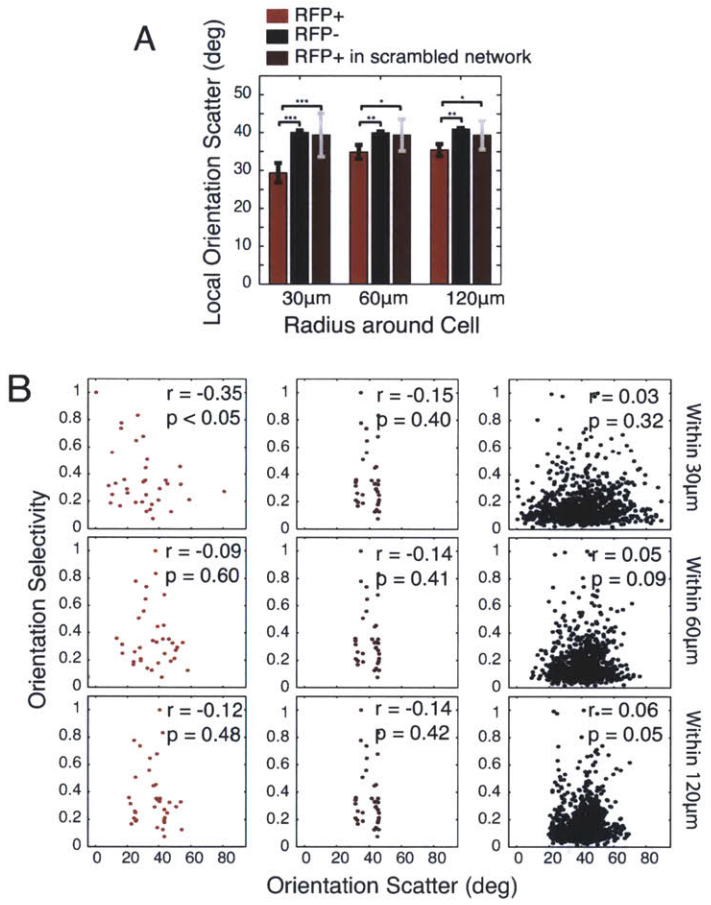

Figure 3.7. Tuned RFP+ neurons tend to share the orientation preferences of their neighbors. (A) The local scatter in orientation preference was measured, surrounding each neuron within 30μm, 60μm, and 120μm radii (red: RFP+ neurons, black: RFP- neurons, burgundy: RFP+ in network with scrambled orientation preferences). The scatter surrounding RFP+ neurons was lower than the scatter surrounding RFP- neurons ($p<0.001$), or RFP+ neurons in scrambled networks ($p<0.001$). Error bars for the RFP+ and RFP- bars indicate s.e.m., while error bars for the RFP+ scrambled bars indicate the 95% confidence interval of the estimate of the mean from 10,000 shuffles of the orientation preferences. (B) Within 30μm, the orientation selectivity of RFP+ neurons (left, red) but not RFP+ neurons in the scrambled networks (middle, burgundy) or RFP- neurons (right, black) is negatively correlated to orientation scatter. This correlation disappears at 60 (middle row) and 120μm (bottom row).

RFP+ neurons. Indeed, the true scatter surrounding RFP+ neurons was less than the scatter surrounding RFP+ neurons when the orientation preferences had been resampled among the cells in the field of view (Figure 3.7A). Thus, PV+ neurons tend to match the orientation preferences of neighboring cells, but RFP- neurons do not.

If PV+ neurons obtain orientation selectivity from the nearest cells, then the orientation map would be expected to be more homogeneous surrounding highly tuned RFP+ neurons than broadly tuned RFP+ neurons. In fact, orientation selectivity of RFP+ neurons but not RFP- neurons was negatively correlated to the local orientation scatter within 30μm (RFP+: $r = -0.35$, $p < 0.05$; RFP-: $r = 0.03$, $p = 0.32$; scrambled RFP+: $r = 0.03$, $p = 0.32$), but this relationship disappears when including cells 60μm (RFP+: $r = -0.09$, $p = 0.60$; RFP-: $r = 0.05$, $p = 0.09$, scrambled RFP+: $r = 0.05$, $r = -0.14$, $p = 0.41$) and 120μm (RFP+: $r = -0.12$, $p = 0.48$; RFP-: $r = 0.06$, $p = 0.05$, scrambled RFP+: $r = -0.14$, $p = 0.42$) away (Figure 3.7B). The relationship between orientation selectivity and local orientation scatter suggests that local networks with more spatially coherent orientation representations surround highly tuned PV+ neurons.

3.5 Discussion

We have carefully described the orientation selectivity of a large number of parvalbumin-expressing (PV+) inhibitory interneurons in the mouse primary visual cortex (V1), using two-photon targeted cell-attached recordings. Although PV+ neurons are less selective for orientation on average than the rest of the neuronal population of the primary visual cortex, the distribution of orientation selectivity in PV+ neurons is bimodal, with a significant population of highly tuned cells. When we compared the dendritic trees of PV+ neurons to their orientation selectivity, we found a strong relationship between structural and functional properties of these cells (Figures 3.2-3.3). Highly tuned PV+ neurons had shorter total dendritic lengths, while broadly tuned PV+ neurons had the longest dendritic projections. Longer dendrites did not necessarily translate to wider dendritic fields, and the polarity of dendritic projections was not related to the orientation selectivity (Figures 3.3-3.4), so broadly tuned inhibitory neurons may simply be sampling the local network

more extensively. Furthermore, we found that tuned PV+ neurons share the orientation preferences of neighboring cells, and that their selectivity depends on the diversity of local orientation preferences (Figure 3.7).

Many groups have now examined the orientation selectivity of inhibitory neurons in the mouse visual cortex; we and others have described the existence of both highly tuned and broadly tuned inhibitory neurons (Niell and Stryker, 2008; Ma et al., 2010; Runyan et al., 2010; Zariwala et al., 2011), while others have described only broadly tuned inhibitory neurons (Sohya et al., 2007; Liu et al., 2009; Kerlin et al., 2010). In this study, we have sampled a large number of PV+ inhibitory interneurons (n = 74 visually responsive PV+ neurons) in order to accurately depict the distribution of orientation selectivity (OSI) in this population. We found that the distribution of orientation selectivity is bimodal for PV+ neurons (Figure 3.1D), with a large peak at a low OSI near 0.3, and a second, smaller peak at a higher OSI that is similar to the mean orientation selectivity in the nonPV+ population, near 0.8. The bimodality of this distribution means that summary statistics such as the mean and standard deviation are misleading, as the mean OSI of the PV+ population is 0.48, a value that is not representative of the population because it falls in the trough between the two local maxima centered on 0.3 and 0.8. Thus, it appears that at least two classes of PV+ neurons exist, in terms of their orientation selectivity, broadly tuned and highly tuned. Differences in targeting and recording methods could account for this subclass missing from some studies (Hasenstaub and Callaway, 2010), as each study has used a unique combination of transgenic mice and recording techniques (Liu et al., 2009; Kerlin et al., 2010; Ma et al., 2010).

The dendritic trees of PV+ neurons were carefully and completely reconstructed in this study. Fine resolution z-stacks captured the full dorsal-ventral extent of the dendritic trees, while post-hoc image processing enhancing the image contrast and careful manual tracing allowed each fine dendritic process to be traced through its full extent. PV+ neurons imaged in slices and reconstructed with identical methodology yielded highly similar dendritic lengths and Sholl analysis results (Figure 3.5). Furthermore, the total dendritic lengths that we measured *in vivo* (0.9mm-5.0mm) are similar to those described by others for inhibitory basket neurons that were imaged *in vitro* (Wang et al., 2002 mean = 2.3mm; Kawaguchi et al., 2006 mean = 2.9mm; Helmstaedter et al., 2009).

Taken together, these results suggest that PV+ neurons obtain higher orientation selectivity by simply restricting their sampling of the local network, which is in agreement with recent findings that inhibitory neurons sample inputs according to a distance function (Bock et al., 2011; Hofer et al., 2011). Because rodents lack the highly ordered orientation maps found in carnivores, it has been commonly assumed in the field that orientation preferences are uniformly random across the rodent visual cortex (Ohki and Reid, 2007). However, our results confirm longstanding hints that local clustering of orientation preferences exist (Dräger, 1975; Kerlin et al., 2010). Local coherence in the orientation map, combined with sparse and highly local sampling of inputs by some inhibitory neurons could lead to high selectivity in these cells. Inhibitory neurons sampling the local network more extensively would sample more diverse orientations (Figure 3.8). Future studies examining the outputs of highly tuned and broadly tuned neurons will determine whether these neurons select their targets according to such spatial rules, or in functionally specific ways (Yoshimura and Callaway, 2005; Fino and Yuste, 2011; Packer and Yuste, 2011).

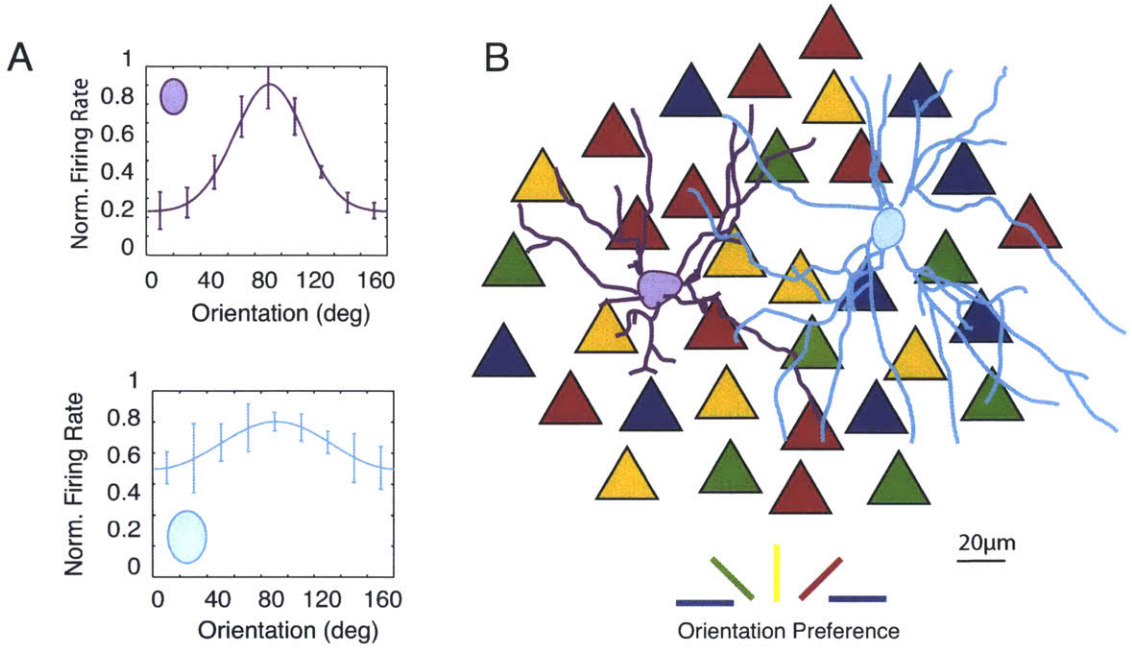

Figure 3.8. How might dendritic structure of PV+ neurons contribute to their tuning properties? (A) The mouse primary visual cortex does not have large-scale mapping organization of orientation preferences. How then do some PV+ neurons obtain highly selective responses for certain stimuli (top, purple), while others respond with broad selectivity (bottom, cyan)? (B) Highly Tuned PV+ neurons have shorter, less tortuous dendrites, with most branching occurring close to the soma. In contrast, Broadly Tuned PV+ neurons have longer, more tortuous dendrites, with more branching occurring farther from the soma. Thus Highly Tuned PV+ neurons sample fewer inputs, and local structure in the orientation representation leads to higher selectivity, while Broadly Tuned PV+ neurons sample more widely from the local network, receiving inputs with more diverse orientation preferences.

3.6 References

Blatow M, Rozov A, Katona I, Hormuzdi SG, Meyer AH, Whittington MA, Caputi A, Monyer H (2003) A Novel Network of Multipolar Bursting Interneurons Generates Theta Frequency Oscillations in Neocortex. Neuron 38:805–817.

Bock DD, Lee W-CA, Kerlin AM, Andermann ML, Hood G, Wetzel AW, Yurgenson S, Soucy ER, Kim HS, Reid RC (2011) Network anatomy and in vivo physiology of visual cortical neurons. Nature 471:177–182.

Cardin JA, Carlén M, Meletis K, Knoblich U, Zhang F, Deisseroth K, Tsai L-H, Moore CI (2009) Driving fast-spiking cells induces gamma rhythm and controls sensory responses. Nature 459:663–667.

Chow A, Erisir A, Farb C, Nadal MS, Ozaita A, Lau D, Welker E, Rudy B (1999) K(+) channel expression distinguishes subpopulations of parvalbumin- and somatostatin-containing neocortical interneurons. J Neurosci 19:9332–9345.

Dombeck DA, Graziano MS, Tank DW (2009) Functional clustering of neurons in motor cortex determined by cellular resolution imaging in awake behaving mice. J Neurosci 29:13751–13760.

Dräger UC (1975) Receptive fields of single cells and topography in mouse visual cortex. J Comp Neurol 160:269–290.

Du J, Zhang L, Weiser M, Rudy B, McBain CJ (1996) Developmental expression and functional characterization of the potassium-channel subunit Kv3.1b in parvalbumin-containing interneurons of the rat hippocampus. J Neurosci 16:506–518.

Feng G, Mellor RH, Bernstein M, Keller-Peck C, Nguyen QT, Wallace M, Nerbonne JM, Lichtman JW, Sanes JR (2000) Imaging neuronal subsets in transgenic mice expressing multiple spectral variants of GFP. Neuron 28:41–51.

Ferster D, Miller KD (2000) Neural mechanisms of orientation selectivity in the visual cortex. Annu Rev Neurosci 23:441–471.

Fino E, Yuste R (2011) Dense Inhibitory Connectivity in Neocortex. Neuron 69:1188–1203.

Gutierrez H, Davies AM (2007) A fast and accurate procedure for deriving the Sholl profile in quantitative studies of neuronal morphology. J Neurosci Methods 163:24–30.

Han ZS (1994) Electrophysiological and morphological differentiation of chandelier and basket cells in the rat hippocampal formation: a study combining intracellular recording and intracellular staining with biocytin. Neurosci Res 19:101–110.

Hasenstaub AR, Callaway EM (2010) Paint it black (or red, or green): optical and genetic tools illuminate inhibitory contributions to cortical circuit function. Neuron 67:681–684.

Helmstaedter M, Sakmann B, Feldmeyer D (2009) L2/3 interneuron groups defined by multiparameter analysis of axonal projection, dendritic geometry, and electrical excitability. Cereb Cortex 19:951–962.

Hippenmeyer S, Vrieseling E, Sigrist M, Portmann T, Laengle C, Ladle DR, Arber S (2005) A developmental switch in the response of DRG neurons to ETS transcription factor signaling. PLoS Biol 3:e159.

Hofer SB, Ko H, Pichler B, Vogelstein J, Ros H, Zeng H, Lein E, Lesica NA, Mrsic-Flogel TD (2011) Differential connectivity and response dynamics of excitatory and inhibitory neurons in visual cortex. Nat Neurosci 14:1045–1052.

Kawaguchi Y, Karube F, Kubota Y (2006) Dendritic branch typing and spine expression patterns in cortical nonpyramidal cells. Cereb Cortex 16:696–711.

Kerlin AM, Andermann ML, Berezovskii VK, Reid RC (2010) Broadly tuned response properties of diverse inhibitory neuron subtypes in mouse visual cortex. Neuron 67:858–871.

Kisvárday ZF, Eysel UT (1993) Functional and structural topography of horizontal inhibitory connections in cat visual cortex. Eur J Neurosci 5:1558–1572.

Krimer LS, Zaitsev AV, Czanner G, Kröner S, González-Burgos G, Povysheva NV, Iyengar S, Barrionuevo G, Lewis DA (2005) Cluster analysis-based physiological classification and morphological properties of inhibitory neurons in layers 2-3 of monkey dorsolateral prefrontal cortex. J Neurophysiol 94:3009–3022.

Kubota Y, Hattori R, Yui Y (1994) Three distinct subpopulations of GABAergic neurons in rat frontal agranular cortex. Brain Res 649:159–173.

Kuhlman SJ, Huang ZJ (2008) High-resolution labeling and functional manipulation of specific neuron types in mouse brain by Cre-activated viral gene expression. PLoS ONE 3:e2005.

Liu B-H, Li P, Li Y-T, Sun YJ, Yanagawa Y, Obata K, Zhang LI, Tao HW (2009) Visual receptive field structure of cortical inhibitory neurons revealed by two-photon imaging guided recording. J Neurosci 29:10520–10532.

Lund JS, Lewis DA (1993) Local circuit neurons of developing and mature macaque prefrontal cortex: Golgi and immunocytochemical characteristics. J Comp Neurol 328:282–312.

Ma W-P, Liu B-H, Li Y-T, Huang ZJ, Zhang LI, Tao HW (2010) Visual representations by cortical somatostatin inhibitory neurons--selective but with weak and delayed responses. J Neurosci 30:14371–14379.

Majewska A, Yiu G, Yuste R (2000) A custom-made two-photon microscope and deconvolution system. Pflugers Arch 441:398–408.

Mariño J, Schummers J, Lyon DC, Schwabe L, Beck O, Wiesing P, Obermayer K, Sur M (2005) Invariant computations in local cortical networks with balanced excitation and inhibition. Nat Neurosci 8:194–201.

Markram H, Toledo-Rodriguez M, Wang Y, Gupta A, Silberberg G, Wu C (2004) Interneurons of the neocortical inhibitory system. Nat Rev Neurosci 5:793–807.

Niell CM, Stryker MP (2008) Highly Selective Receptive Fields in Mouse Visual Cortex. J Neurosci 28:7520–7536.

Ohki K, Reid RC (2007) Specificity and randomness in the visual cortex. Curr Opin Neurobiol 17:401–407.

Packer AM, Yuste R (2011) Dense, Unspecific Connectivity of Neocortical Parvalbumin-Positive Interneurons: A Canonical Microcircuit for Inhibition? J Neurosci 31:13260–13271.

Peng H, Ruan Z, Long F, Simpson JH, Myers EW (2010) V3D enables real-time 3D visualization and quantitative analysis of large-scale biological image data sets. Nat Biotechnol 28:348–353.

Priebe NJ, Ferster D (2008) Inhibition, spike threshold, and stimulus selectivity in primary visual cortex. Neuron 57:482–497.

Runyan CA, Schummers J, Van Wart A, Kuhlman SJ, Wilson NR, Huang ZJ, Sur M (2010) Response features of parvalbumin-expressing interneurons suggest precise roles for

subtypes of inhibition in visual cortex. Neuron 67:847–857.
Schummers J, Mariño J, Sur M (2002) Synaptic integration by V1 neurons depends on location within the orientation map. Neuron 36:969–978.
Schummers J, Yu H, Sur M (2008) Tuned responses of astrocytes and their influence on hemodynamic signals in the visual cortex. Science 320:1638–1643.
Sholl DA (1953) Dendritic organization in the neurons of the visual and motor cortices of the cat. J Anat 87:387–406.
Sohya K, Kameyama K, Yanagawa Y, Obata K, Tsumoto T (2007) GABAergic neurons are less selective to stimulus orientation than excitatory neurons in layer II/III of visual cortex, as revealed by in vivo functional Ca2+ imaging in transgenic mice. J Neurosci 27:2145–2149.
Vruwink M, Schmidt HH, Weinberg RJ, Burette A (2001) Substance P and nitric oxide signaling in cerebral cortex: anatomical evidence for reciprocal signaling between two classes of interneurons. J Comp Neurol 441:288–301.
Wang Y, Gupta A, Toledo-Rodriguez M, Wu CZ, Markram H (2002) Anatomical, physiological, molecular and circuit properties of nest basket cells in the developing somatosensory cortex. Cereb Cortex 12:395–410.
Wehr M, Zador AM (2003) Balanced inhibition underlies tuning and sharpens spike timing in auditory cortex. Nature 426:442–446.
Yan XX, Baram TZ, Gerth A, Schultz L, Ribak CE (1998) Co-localization of corticotropin-releasing hormone with glutamate decarboxylase and calcium-binding proteins in infant rat neocortical interneurons. Exp Brain Res 123:334–340.
Yoshimura Y, Callaway EM (2005) Fine-scale specificity of cortical networks depends on inhibitory cell type and connectivity. Nat Neurosci 8:1552–1559.
Zaitsev AV, Povysheva NV, Gonzalez-Burgos G, Rotaru D, Fish KN, Krimer LS, Lewis DA (2009) Interneuron Diversity in Layers 2-3 of Monkey Prefrontal Cortex. Cerebral Cortex 19:1597–1615.
Zariwala HA, Madisen L, Ahrens KF, Bernard A, Lein ES, Jones AR, Zeng H (2011) Visual Tuning Properties of Genetically Identified Layer 2/3 Neuronal Types in the Primary Visual Cortex of Cre-Transgenic Mice. Front Syst Neurosci 4:1–16.

Chapter 4: Division and subtraction by distinct cortical inhibitory networks *in vivo*[1]

4.1 Summary

Brain circuits process information via specialized neuronal subclasses interacting within a network. Revealing their interplay requires activating specific cells while monitoring others in a functioning circuit. Here, using a new platform for two-way light-based circuit interrogation in visual cortex *in vivo*, we show the computational implications of modulating different subclasses of inhibitory neurons during sensory processing. While soma-targeting, parvalbumin-expressing interneurons (PV) divide responses (E/I) but preserve stimulus selectivity, dendrite-targeting, somatostatin-expressing inhibitory neurons (SOM) subtract from excitatory responses (E-I) and sharpen selectivity. Visualized in vivo cell-attached recordings demonstrate that division by PV neurons alters response gain whereas subtraction by SOM neurons shifts response levels. These findings provide direct evidence that inhibitory neuronal subclasses have distinct and complementary roles in cortical computations.

4.2 Introduction

Inhibition plays fundamental and diverse roles in cortical circuits, and is delivered by specialized cell types that have distinct intrinsic properties and connectivity patterns (Freund and Buzsáki, 1996; Markram et al., 2004; Klausberger and Somogyi, 2008). This diversity suggests that different inhibitory subtypes may have developed to serve distinct computational functions (Isaacson and Scanziani, 2011), and thus may hold specific relevance to neurological disorders (Lewis, 2000). For example, inhibition may not only regulate baseline activity and brain rhythms (Wang and Buzsáki, 1996; Cardin et al., 2009),

[1] The findings of this chapter were under review at *Nature* at the time of submission of the thesis: *Wilson*, Runyan*, Wang, & Sur. (Under Review). Division and subtraction by distinct inhibitory networks in vivo.*

but also sharpen responses to specific inputs (Rose and Blakemore, 1974; Sillito, 1979; Xing et al., 2011), regulate the gain of responses (Chance et al., 2002; Mitchell and Silver, 2003; Atallah et al., 2012), and mediate suppressive interactions between responses (Morrone et al., 1982; Crook et al., 1998; Kapfer et al., 2007; Silberberg and Markram, 2007). However, determining the potential sources of these inhibitory effects requires monitoring the changes in response patterns of specific cells while selectively manipulating the activity of different subclasses of inhibition.

Two key subclasses of inhibitory neurons are the neurons expressing parvalbumin (PV) and those expressing somatostatin (SOM). These subtypes are distinct in the cortex (Lund and Lewis, 1993; Kubota et al., 1994; Gonchar and Burkhalter, 1997; Kawaguchi and Kubota, 1997; Kawaguchi and Kondo, 2002; Gonchar et al., 2007; Xu et al., 2010), and differ in the anatomical targeting of their axons. PV neurons form inhibitory synapses in the proximal region of their targets, including the soma, axon initial segment, and proximal dendrites, while SOM neurons form synapses on more distal regions of the dendrites of their targets (DeFelipe and Fariñas, 1992; Kawaguchi and Kubota, 1997). This distinction between PV and SOM neurons has critical computational implications: PV inhibitory activity occurring near the soma affects the ability of all excitatory inputs to elicit a spike, limiting the temporal integration window in which inputs can be summed to produce a response, while the more distal SOM inhibitory signals interact with specific excitatory inputs, suppressing their ability to propagate along the dendrite (Pouille and Scanziani, 2001; Berger, 2003; Spruston, 2008).

Because specific inhibitory cell classes could not easily be manipulated, previous pharmacological or intracellular studies in primary visual cortex (V1) have necessarily considered inhibition as a single entity, and have produced contradictory findings on the role of inhibition. On the one hand, inhibition has been proposed to sharpen neuronal responses by removing weak inputs (Sillito, 1975; Bauman and Bonds, 1991; Vidyasagar et al., 1996), though there have been conflicting reports on whether inhibition predominantly targets non-preferred responses or preferred ones (Sompolinsky and Shapley, 1997; Ferster and Miller, 2000; Monier et al., 2003; Wehr and Zador, 2003; Priebe and Ferster, 2008). On the other hand, inhibition has been posited to control response gain (Chance et al., 2002; Mitchell and Silver, 2003), a network process by which cortical networks rapidly

"divide" or scale their dynamic range of responses (Heeger, 1992; Carandini and Heeger, 1994; Carandini et al., 1997; Busse et al., 2009). Such divisive inhibition is thought to be fundamental to processing across many brain systems, from primary sensory computations (Carandini and Heeger, 1994; Somers et al., 1995; Olsen et al., 2010; Papadopoulou et al., 2011) to motion integration (Simoncelli and Heeger, 1998), gaze enhancement (Andersen and Mountcastle, 1983), attention (Reynolds and Heeger, 2009), multisensory integration (Ohshiro et al., 2011), and value estimation (Louie and Glimcher, 2010).

Here, we show that inhibition in the cerebral cortex can have either of these functions, depending on its cellular source. We specifically activated two key subclasses of inhibitory cells, soma-targeting parvalbumin(PV)-expressing neurons and dendrite-targeting somatostatin(SOM)-expressing neurons. By combining optogenetic stimulation (Deisseroth, 2010) with population calcium imaging (Ohki et al., 2005; Schummers et al., 2008; Runyan et al., 2010), we were able to simultaneously measure the effects of specific types of inhibition on many target cells simultaneously. We then confirmed the differential effects of PV- and SOM-mediated inhibition by recording electrophysiological responses in their target cells.

4.3 Experimental Procedures

4.3.1: Mice

Experiments were carried out in mice under protocols approved by MIT's Animal Care and Use Committee and conformed to NIH guidelines. Heterozygous PV-Cre knock-in driver mice, which express Cre in over 90% of PV+ neurons, and SOM-Cre knock-in mice were backcrossed into a C57BL/6 line (Hippenmeyer et al., 2005; Taniguchi et al., 2011). Mice heterozygous for the GAD67-GFP (Δneo) allele (Tamamaki et al., 2003) were maintained on a C57BL/6 background; only mice older than 8 weeks were used. Numerous control experiments and development were also performed in Thy1-ChR2-YFP mice (Jackson labs).

4.3.2 Viral construct and injection

ChR2-mCherry was expressed specifically in Parvalbumin+ (PV) or Somatostatin+ (SOM) interneurons in the visual cortex of PV-Cre or SOM-Cre mice by infection of a double-floxed inverted open reading frame ChR2-mCherry adeno-associated viral construct.

Six-week old Cre mice were initially anaesthetized with 4% isoflurane in oxygen, and maintained on 2% isoflurane. The target coordinates were displaced from Bregma by 3.5 mm posterior and 2.2 mm lateral. The skull was thinned along a 1 mm line at the rostral edge of V1, and the remaining skull and dura were punctured using a glass micropipette filled with the virus. Two injections were made at each site, one at 500 μm below the cortical surface, and one at a depth of 250 μm. A volume of 0.25 μl of virus was injected at 125 nl/min at each depth. After each injection, the pipette was held in place for 5 minutes prior to retraction to prevent leakage.

4.3.3 Animal Preparation

Two weeks post-injection, mice were anesthetized with a cocktail containing Fentanyl (0.05mg/kg), Midazolam (5mg/kg), and Medetomidine (0.5mg/kg), supplemented with isoflurane. The eyes were protected with ophthalmic ointment during the surgery, and moistened afterward with saline. A metal headplate was attached to the skull using superglue and dental acrylic, and a 2mm x 2mm craniotomy was performed over the primary visual cortex region (area 17). The exposed area was then covered with a thin layer of 2% agarose in ACSF (140mM NaCl, 5mM KCl, 2mM $CaCl_2$, 1mM $MgCl_2$, .01mM EDTA, 10mM HEPES, 10mM Glucose, pH 7.4).

The mouse was transferred to the microscope (described below), and 0.5% isoflurane in oxygen was supplied through a tube, with fentanyl/medetomidine injected as needed every few hours. The body temperature was maintained at 37.5 C with a heating blanket (Harvard Apparatus) and supplementary heating pads. The recording phase of physiology experiments typically lasted for 4–6 hr in calcium imaging experiments and 8–12 hr in electrophysiology experiments.

For *in vitro* experiments, coronal sections (300 μm thick) of visual cortex were cut in <4°C ACSF using a Vibratome (Leica). Slices were incubated at 37°C for 20 minutes after slicing, and at room temperature for the remainder of the experiment. Slices were

transferred to a chamber (Warner Instruments) and recordings were taken from visually identified pyramidal neurons. Artificial cerebral spinal fluid (ACSF) contained 126 mM NaCl, 25 mM NaHCO3, 1 mM NaHPO4, 3 mM KCl, 2 mM MgSO4, 2 mM CaCl2, and 14 mM dextrose, was adjusted to 315-320 mOsm and 7.4 pH, and was bubbled with 95% O2 / 5% CO2. The intracellular pipette solution contained 100 mM potassium gluconate, 20 mM KCl, 10 mM HEPES, 4 mM MgATP, 0.3 mM NaGTP, and 10 mM Na-phosphocreatine.

4.3.4 Immunohistochemistry

Immediately after physiology experiments were completed, mice were overdosed with pentobarbitol and perfused transcardially with saline followed by 4% paraformaldehyde. The brain was extracted, cryoprotected in 30% sucrose/PBS, and then 40 μm sections were generated with a cryostat. Sections were blocked in 10% goat serum and 0.1% triton in PBS for 60 minutes at room temperature on a shaker, and incubated overnight at 4°C in primary antibody for somatostatin (rabbit anti-somatostatin, 1:200, Millipore, AB5494) or parvalbumin (mouse anti-parvalbumin, 1:250, Chemicon, MAB1572). Sections were then washed several times and incubated in secondary antibody for either somatostatin (goat anti-rabbit biotin-XX, Invitrogen) or parvalbumin (goat anti-guinea pig Alexa Fluor 488, 1:200, Molecular Probes, A11073). The somatostatin stain was amplified with an immunoperoxidase reaction (TSA Kit #12 with HRP, goat anti-rabbit IgG and Alexa Fluor 488 tyramide, Invitrogen, T-20922). Sections were mounted on slides and coverslipped with Vectashield Hardset mounting media with DAPI (Vector Labs). Images of immuno-fluorescent sections were taken at 20X with a confocal microscope (Zeiss LSM5 Exciter) and quantified with ImageJ (NIH). Cell counts and overlap were quantified using ImageJ software (NIH), where cells were identified via convex hull image segmentation, and considered positive for staining in a given channel when mean intensity within the cell area exceeded 100% baseline.

4.3.5 In vivo cell-attached electrophysiological recordings

Recordings[41] were made using custom software (Network Prism, Sur Lab) written in Matlab (Mathworks, Natick, MA) controlling a MultiClamp 700B Amplifier (Axon) that measured differences between a glass pipette electrode inserted into the brain at 20-35^0

and an Ag/AgCl ground pellet electrode (Warner Instruments) positioned in the same solution as the brain and the lens objective. Borosilicate pipettes (outer diameter=1.5mm, inner diameter=1.17mm, WPI) were pulled using a Sutter P-2000 laser puller (Sutter Instruments) to a diameter of 3-7 MΩ. For fluorescent visualization, pipettes were back-filled using capillary action for several minutes with either Oregon Green BAPTA 1-AM (during imaging; see below), Alexa Fluor 488 (100 um, Molecular Probes), or Alexa Fluor 594 (100 um, Molecular Probes). The pipette was targeted to the injection site using a 10x lens, and then targeted to individual cells using a 25x lens via concurrent two-photon imaging at 770 or 920 nm. Cells were either targeted by moving the pipette into the 3D vicinity and then commencing diagonal advance, or cells were patched blindly by advancing diagonally through the cortex. During cell approach, either zero pressure or light positive pressure was applied. Cell proximity was detected through deflections in electrical resistance observed in voltage clamp during a rapidly time-varying 5 mV command voltage. Once resistance had increased by 5-10 MΩ, slight negative pressure was applied and the pipette was advanced more slowly until resistance increased to 20-100 MΩ. At that point the amplifier was switched to current clamp, and spikes were recorded with zero injected current, under a Bessel filter of 4 KHz and an AC filter of 300 Hz.

4.3.6 In vitro whole-cell electrophysiological recordings

Borosilicate pipettes (3-5 MΩ, WPI) were pulled using a Sutter P-2000 puller (Sutter Instruments). Cells were visualized with an Achroplan 40x water-immersion lens with infrared-DIC optics and detected with an infrared camera (QImaging QICam) digitized to a computer monitor. Target cells were identified by briefly flashing either blue light (for YFP, filtered using FITC/CY2) or green light (for mCherry, filtered using TRITC/CY3). Experiments were driven by custom acquisition software (Network Prism, Sur Lab) again using a Multiclamp 700B amplifier (Axon Instruments) connected to a BNC-2110 connector block and M-Series dual-channel acquisition card (National Instruments). For each recording, a fast 5 mV test pulse was applied in voltage clamp to obtain the gigaseal, rupture was achieved by negative pressure delivered by mouth, and whole-cell recordings were then continuously verified for low levels of leak and series resistance. Depolarizations mediated by ChR2 activation were measured in voltage clamp at -60 mV.

ChR2-driven spiking was then measured in current clamp while injecting steady offset current to maintain baseline potential at -60 mV. All recordings were sampled at 10 kHz and low-pass filtered at 1 kHz.

4.3.7 Two-photon imaging: Bulk loading of calcium indicator

50 ug of Oregon Green BAPTA 1-AM (Invitrogen) was centrifuged and mixed with 4 ul pluronic acid (20% in DMSO) for 20 minutes, protecting from light. After verifying that mixture had occurred (presence of green tint) we then added this 4 µl to 46 µl of a solution containing 10 mM Alexa 594 (Invitrogen) in 200 µl of saline. This mixture was then centrifuged through a 0.22 um filter (Millipore) for 30 seconds and stored on ice. Borosilicate pipettes (outer diameter=1.5mm, inner diameter=1.17mm, WPI) were then pulled using a Sutter P-2000 laser puller (Sutter Instruments) to a diameter of 1-5 MΩ. 2 µl of dye was added to each pipette and allowed to fill to the tip via capillary action over minutes. The filled tip was then navigated to the 3D area of interest within cortex under two-photon imaging guidance. Once in position, sustained but light positive pressure was incrementally applied in an increasing manner using a Picrospritzer II until dye ejection began, as verified using continuous two-photon imaging in the red and green channels. Once dye ejection had been detected, we sustained that level of "minimal" positive pressure for 60 seconds. We then waited 1-2 hours to ensure that dye uptake across a large number of cells had been achieved.

4.3.8 Two-photon imaging system

We used a Prairie Ultima two-photon system (Prairie Technologies) driven by a Spectra Physics Mai-Tai eHP laser, passed through a Deep-See module (Spectra Physics / Newport). Laser power was controlled via pockels cell (Conoptics) and guided into the scan head of a modified Olympus BX51WIF microscope using the standard Prairie configuration. The excitation laser tuned to 770 nm-960 nm was then passed through a 660 LP filter, and out through the objective. Received light then passed back through the objective, bounced off of the 660 LP filter, through an IR blocking filter (IR Super-Cold Mirror, 45 mm) and into a PMT separator dichroic mirror (575 LP) which split the signal to a red PMT (with 607/45 barrier filter), or a green PMT (with 525/70 barrier filter). All

functional imaging was done using a 25x Olympus XL Plan N high-numerical index objective lens.

4.3.9 Targeted scan imaging

Following bulk loading (see above), we then used a custom all-Matlab system (Network Visor, Sur Lab) to detect changes in fluorescence associated with cellular activity. Briefly, the red and green PMT BNC cables coming from a two photon microscope (Prairie Ultima), and carrying fluorescence information, were forked and fed into a custom A/D acquisition system and graphical user interface (National Instruments+Matlab) and sampled at 1.25 MHz / channel. The control lines of the two-photon's X and Y galvanometers were in turn substituted with D/A control lines from the custom system. To switch arbitrarily between using the base imaging system and our custom scans, we added a TTL switch that selected which control source was used to control the galvanometer at any time. Finally, the X and Y galvanometer feedback lines were connected to our custom A/D system, to acquire the real-time position (also at 1.25 MHz) of the galvanometers to back-attribute the fluorescence signals detected to accurate X,Y positions. Imaging then proceeded under software control by 1) conducting a raster scan to identify cell positions, 2) using machine vision algorithms to cleanly identify and segment the cell bodies, 3) use a genetic algorithm to identify the shortest scan path between cells (Lillis et al., 2008) and 4) running the scan path rapidly with higher dwell time inside of the cells and faster jumps between cells. The imaging parameters that we used for all data were: 1-100 cells, 50 Hz imaging (20 ms per lap), 90% of the 20 ms imaging lap within the cell.

4.3.10 Optogenetic stimulation

To deliver channelrhodopsin to genetically-defined subclasses of cells, we used the AAV-DIO-ChR2-mCherry strategy recently pioneered[7] which uses an adeno-associated virus (AAV) with a double-floxed inverted open reading frame (DIO) and a payload of channelrhodopsin fused to mCherry (ChR2-mCherry). The pAAV-Ef1a-DIO-hChR2(H134R)-mCherry-WPRE-pA live virus was a gift from Dinos Meletis and Marie Carlen in the laboratory of Li-Huei Tsai and subsequently received from the University of North Carolina viral vector core facility. Specific cell subclasses expressing Cre (SOM or PV,

see Mice above) upon viral expression will undergo Cre recombination which reverses the payload sequence to activate its expression. Following delivery of the virus to cells (see Viral Injection above) and waiting a minimum of 2 weeks (though expression was best at 4-8 weeks), cells became illuminated with mCherry connoting functional ChR2 expression. To drive these cells, we employed a diode-pumped solid state blue laser with analog intensity control (473 nm, 200 mW, MBL-III-473, OptoEngine, LLC) coupled via SMA terminal to a 200 um fiber (ThorLabs) that was integrated into our microscope light path (Prairie Technologies). Pulse patterns were driven via custom D/A optogenetics software written in Matlab and synchronized with our other systems via trigger pulses.

4.3.11 Visual and optogenetic stimulation: Orientation tuning

To assess the orientation selectivity and tuning of different neurons, we presented oriented gratings to a 23" 1080p LCD monitor (Dell) using custom software (Network Visstim, Sur Lab) written in ActiveSTIM (Activestim.com) and PsychToolbox-3 (Psychtoolbox.com) on a Windows 7 computer (Dell Precision) with a GeForce 8800 GTS 640MB graphics card (PNY). Gratings were optimized for cellular responsiveness using a contrast of 100%, spatial frequency of 0.002-0.256 cycles/degree, and a temporal frequency of 1-3Hz. Gratings were then presented by stepping the orientation from 0-360 degrees in steps of 20 degrees, with each grating presentation being preceded for 4 seconds "off" followed by 4 seconds "on", for a total presentation duration of 144 seconds. Each of these "trials" was then repeated with and without optogenetic stimulation, alternating conditions every trial and acquiring between 8-40 trials per cell or network. Optogenetic stimulation preceded the onset of visual stimulus by 100 ms, and consisted of 10 pulses, 10ms each, at 10 Hz for 1 second. Thus, during every recording sweep, the visual stimulation was on from 4-8 s, and the optogenetic stimulation was on from 3.9-4.9sec.

4.3.12 Visual and optogenetic stimulation: Contrast-response functions

To assess the contrast responses of different neurons, we repeated the visual stimulation conditions above, except with different stimulus parameters. First, the optimal stimulus parameters (orientation, spatial frequency, temporal frequency) for the cell of

interest was determined empirically using the procedure above. We then used these parameters to collect contrast responses at 0, 2, 4, 8, 16, 32, 64, 100, 64, 32, 16, 8, 4, 2, 0% contrast, presenting the gratings of different contrast with a 4 second preceding "off" period followed by a 2 second "on" period, for a total presentation of 90 seconds. Each of these ascending and descending contrast "trials" was then repeated with and without optogenetic stimulation, alternating conditions every trial and acquiring between 6-25 trials per cell. Optogenetic stimulation again preceded the onset of visual stimulus by 100ms, and consisted of 10 pulses, 10ms each, at 10 Hz for 1 second. Thus, during every recording sweep, the visual stimulation was on from 4-6sec, and the optogenetic stimulation was on from 3.9-4.9sec.

4.3.13 Data analysis: Electrophysiology

Data was acquired directly into Matlab via custom software (Network Prism, Sur Lab) and saved as .mat files. Spike detection was performed via analysis routines that used manually-defined thresholds followed by spike shape template matching for further verification. Spike times in response to every stimulus were then grouped into "on" or "off" periods based on their timing relative to visual stimulation, and "on" spikes for each stimulus were decremented by the number of "off" spikes observed during an equal time period. For orientation experiments, # spikes per stimulus = (# spikes "on") - (# spikes "off") because "on" and "off" periods were the same duration. For contrast experiments, # spikes per stimulus = (# spikes "on") - ((# spikes "off first half" + # spikes "off second half") / 2) because "off" was twice as long as "on". In this manner, # spikes for every stimulus were collected for each cell, and grouped according to trials with and without optogenetic stimulation.

4.3.14 Data analysis: Targeted scan imaging

Data was acquired directly into Matlab via custom software (Network Visor, Sur Lab) and saved as .mat files. Data consisted of, for example, 144 seconds of imaging a network at 50 Hz, where every second the laser would spin around the network sampling the many cells, dwelling in identified cell bodies along the way and spending minimal durations in the gaps between cells. This resulted in a repeated "scan pattern" that the

laser followed repeatedly to collect information on every cell. Data from the green PMT channel was thus isolated as a time-varying fluorescence waveform and was then aligned with the X,Y position of the galvanometers during each moment of the scan, by using the X,Y feedback vectors recorded (see Fastscan imaging, above). This allowed us to attribute recorded fluorescence back to the moment-to-moment position of the laser in excitation space as it proceeded along each lap of the repeated scan pattern. The position vectors were then transformed to "cell id" vectors that recognized which moments the laser was within the convex hull borders of each cell, tagging every position at which fluorescence was recorded with a cell id, or no cell id if the laser was passing between cells at that instant. This allowed us to break up the global PMT signal and re-build waveforms for every cell that was scanned. If the laser completed a lap every 0.020 ms (50 Hz), and there were 50 cells, then with 90% dwell time we would excite every cell for 360 us every lap, a significant dwell time. Because we were also sampling at a high rate (1.25 MHz / channel), we collected many samples at every cell during every lap. These samples were averaged to create a single data point (F) for every cell during every 0.020 ms lap, and the data points for the cells were collected into F waveforms. F was then transformed into dF/F % by determining the 7% percentile of the F waveform and considering this the baseline, and computing (F – F_baseline) / F_baseline * 100% for every point in the waveform. The dF/F waveform was then detrended for bleaching as a precaution (though none was usually evident), and down-sampled by a factor of 5 for further precision in estimating the size of the transients. Finally, the full frame average dF/F was subtracted from every cell's individual dF/F to ensure that positive transients were indeed specific to the cell of interest. Within these cellular response waveforms then, dF/F responses were quantified for each stimulus by finding the peak of the response within the "on" period of the stimulus and subtracting the local baseline averaged during the corresponding "off" period of the stimulus. In this manner, dF/F responses for every stimulus were collected for every cell, and grouped according to trials with and without optogenetic stimulation.

4.3.15 Data analysis: Imaging during optogenetic stimulation

It is not feasible to image during blue laser pulses, and we simply relied on imaging the peak response that immediately followed the "blinded" period, which typically does not

miss the overall peak of the visual response (due to the summation of calcium signal that continues to grow from visual stimulus onset), in order to estimate the relative effect of optogenetic stimulation on responses. In other words, "stimulus artifacts" where optical stimulation intersected with optical measurements were removed just as one would in electrophysiology where electrical stimulation intersected with electrical measurements - this same procedure was applied equally across all stimuli, cells and conditions.

4.3.16 Data analysis: Orientation tuning curves

For every cell of interest, the methods in "Data analysis: Electrophysiology" or "Data analysis: Targeted scan imaging" were used to collect responses for each oriented stimulus (0 to 360 degrees, in steps of 20 degrees) collected during each repeated 144 second trial. These responses were then turned into a "tuning curve" of orientation vs. response for each trial. These tuning curves were grouped according to whether or not optogenetic stimulation was present (baseline vs. ChR2, for example). The response tuning curves in each group were then averaged to produce the average tuning curve for the cell without optogenetic stimulation (A, "Control"), and the average tuning curve for the cell with stimulation (B, "+PV" or "+SOM"). The "suppression" for each stimulus was computed as the simple decrement (A-B) in response when subtracting the optogenetic responses from the corresponding baseline responses: for electrophysiology it was the "number of spikes fewer", and for fastscan imaging it was "delta dF/F" at each stimulus from subtracting (A-B). Preferred orientation (PO) was computed by identifying the orientation associated with the maximum response in the control curve. For some figures as noted, Gaussian fits were computed for the tuning curves using either single Gaussians (population data), or a sum of two Gaussians (cell data) with peaks 180° apart and five parameters: preferred orientation θ_p, tuning width σ, baseline response R_0, response at the preferred orientation R_p, and response at the null orientation R_n (Carandini and Ferster, 2000). For summary Gaussian curves, cells with maximal tuning curve amplitudes of at least 5% dF/F were used and responses were thresholded at a dF/F value of 2.5%, chosen as a close estimation of the fluorescence change associated with one spike. Peak responses were centered at 0 degrees, averaged, and then fit using a single Gaussian to the peak response. Tuning curve statistics were computed as follows: 1) baseline was the average level (dF/F) above zero of

the flat portion of the Gaussian, 2) amplitude was computed as the difference between the Baseline and the peak of the Gaussian, 3) tuning width was computed as the half-width at half-maximum of the Gaussian function, and 4) and Orientation Selectivity Index (OSI) was computed by taking the vector average for the preferred orientation according to the formula OSI = sqrt[sum(response*cos(2*theta))^2+sum(response*sin(2*theta)^2))] / sum(responses). Increases in OSI could thus be due to either a decrease in tuning width, or a subtraction across all values of the baseline response. The direction selectivity index (DSI) was calculated as the ratio of the difference of the fit amplitudes in the preferred and non-preferred directions and their sum. Population mean tuning curves shown in Figs. 2-3 were obtained by plotting the Gaussian function with the mean parameter values (baseline, amplitude, and sigma converted from HWHM) from cells in the control and +ChR2 conditions, and the associated s.e.m. values. Goodness of fit for division or subtraction was quantified for orientation by plotting Control data points for all orientations versus their corresponding +ChR2 data points, and measuring the deviation between those values using least squares when the Control data was either subtracted or divided to match the ChR2 data.

4.3.17 Data analysis: Contrast response curves

For every cell of interest, the methods in "Data analysis: Electrophysiology" were used to collect responses for each stimulus of ascending contrast (0, 2, 4, 8, 16, 32, 64, 100%). These responses were then turned into a "contrast response curve" of contrast vs. response for each trial. These "contrast response curves" were then grouped according to whether or not optogenetic stimulation was present (control vs. ChR2, for example). The response curves in each group were then averaged to produce the average curve for the cell without optogenetic stimulation (A), and the average tuning curve for the cell with stimulation (B), each fit with a Naka-Rushton function (y = Rmax*((response^n)/(response^n+C50^n))) to obtain the Rmax , the saturation point, and the C50, the contrast at the half-saturation point, while n was maintained at the same value between conditions. For contrast recordings, goodness of fit was statistically compared by doing a t-test between the actual suppression values at 16% contrast and the predicted suppression for pure subtraction (equal to suppression at RMax) or pure division (equal to

suppression at RMax, scaled down by the ratio of response / response at maximum contrast). Suppression slopes for contrast data to probe for imbalance of suppression were taken by measuring the suppression with ChR2 at 16, 32, 64 and 100% contrast for each cell, normalizing by that cell's max suppression, and fitting a line to these suppression values.

4.3.18 Statistics

All comparisons, including between Control and +ChR2 conditions, were performed with paired two-tailed t-tests. All means are reported with the standard error of the mean, unless otherwise stated. Comparisons between target cell populations were performed with unpaired two-tailed t-tests.

4.4 Results

4.4.1 All-optical network dissection of cortical inhibitory subclasses during visual computations

In order to measure the effects of distinct cell classes within a functioning network, we built a custom system bringing together different forms of optogenetic stimulation with in vivo two-photon imaging in the mammalian brain (Figure 4.1A). To detect subtle effects of inhibitory activation on neighboring cells, we also developed a custom algorithm-driven high-speed high-dwell imaging system (Figure 4.1A) that automatically locked onto cells in a network loaded with a calcium indicator dye (OGB, Figure 4.1B), computed a scan path (Figure 4.1C, (Lillis et al., 2008)), and sampled population activity at high temporal resolution with high dwell times within neurons (Figure 4.1C-D). This allowed us to achieve high signal to noise, permitting precise detection of various levels of suppression in optical responses. The measured fluorescence traces yielded orientation-selective responses that were highly repeatable across trials (Figure 4.1E) and enabled the resolution of clear tuning curves (Figure 4.1F).

To optically activate PV or SOM neurons, in parallel experiments, we specifically expressed channelrhodopsin-2 (ChR2) in these cells by injecting a double-floxed ChR2-

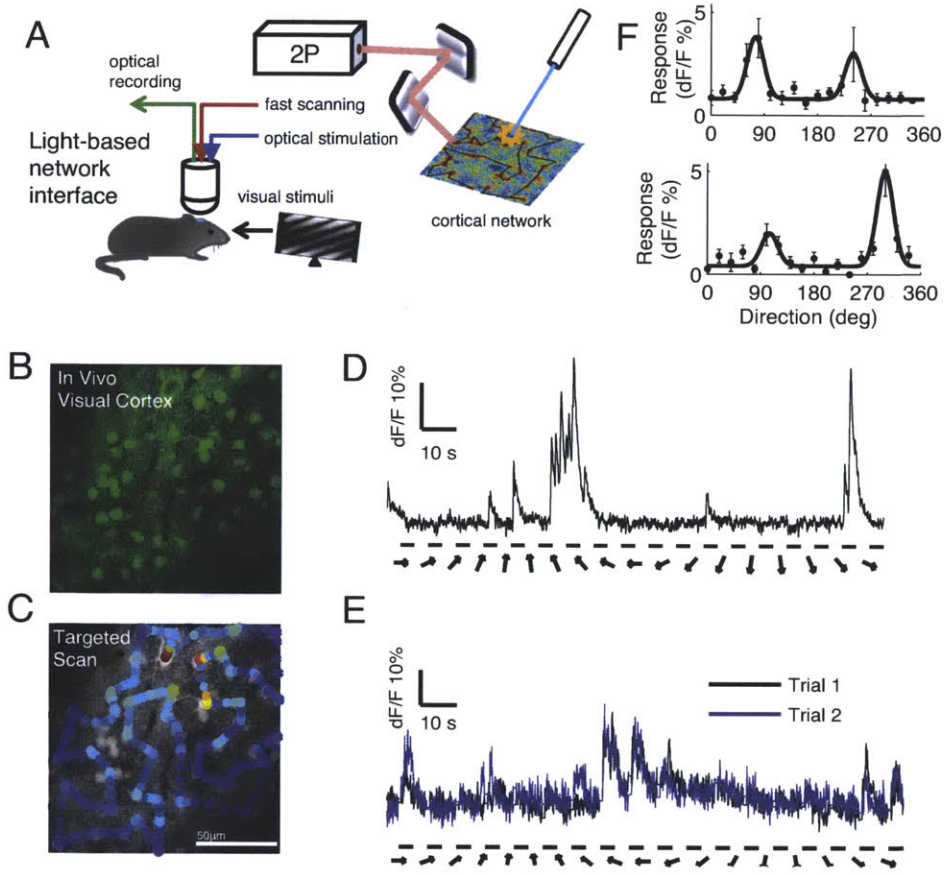

Figure 4.1. All-optical network dissection of cortical subclasses during visual computations. (A) Directed light, for optical recording and stimulation, was targeted to the cortical network of an animal being shown visual stimuli. (B) A traditional raster scan located cells in the network that were bulk loaded with the calcium indicator dye Oregon Green Bapta1-AM (OGB). (C) These cells were then imaged at high speed using targeted 2P scanning along an arbitrary scan path. Scale bar: 50 μm, applies to B and C. (D) This led to the optical detection of robust cellular activity in response to episodically presented oriented drifting gratings (shown by arrows), that could be analyzed as primary signals or deconvolved to estimate action potentials (red lines). (E) Evoked optical traces were highly consistent over repeated presentations of visual stimuli. (F) The clear, repeatable responses allowed for the resolution of well-defined response tuning curves (dots), fit by dual Gaussians (line).

mcherry viral construct into PV-Cre or SOM-Cre mice (Cardin et al., 2009). Immunostaining in injected PV-Cre mice revealed that mCherry-ChR2 was highly co-localized with PV (Figure 4.2A), as 97% of mCherry-labeled cells were PV+ (N = 391 cells, Figure 4.2B). In SOM-Cre mice, mCherry-ChR2 was specifically expressed in SOM neurons (Figure 4.2C); in these animals, 100% of mCherry-labeled cells were SOM+ (N=76, Figure 4.2D). This led to highly reliable, on-demand activation of infected neurons *in vivo* (Figure 4.2E-H), where we could modulate interneuron spiking on a timescale of milliseconds, produce sustained stimulation over seconds, or induce robust rhythms with periodic stimulation. Targeted *in vivo* cell-attached recordings (Figure 4.2E) were used to verify optogenetic modulation during visual stimulation, in which interneurons were selectively driven for a 1-second interval at the onset of visual stimulation (Figure 4.2F). We then recorded responses of neighboring, non-infected neurons to episodically presented drifting oriented gratings (Figure 4.2I) and interleaved these recordings with trials where we inhibited the cells through interneuron activation (Figure 4.2J). Concurrent calcium imaging and optogenetic stimulation allowed us to simultaneously quantify both interneuron activation and suppression of neighboring cells during visual stimulation.

4.4.2 Divisive and subtractive inhibition driven by different inhibitory cell classes

By loading a patch of visual cortex in PV-Cre mice with the calcium indicator dye OGB, we could visualize both ChR2-infected PV cells as well as non-infected cells (Figure 4.3A). Thus, we could optically activate PV cells while recording the visual responses of non-infected cells with a scan path customized for each image, and thereby assess the nature of suppression evoked by PV cells (Figure 4.3B); we could similarly stimulate ChR2-infected SOM cells (Figure 4.3C) and assess their effects on target cells (Figure 4.3D). Activation of both PV and SOM cells resulted in a significant decrease in the peak responses of target cells compared to responses measured during interleaved non-ChR2 trials (Figure 4.3E; PV: 79.1±1% of Control, N=150 cells, P<0.001; SOM: 79.7±2% of Control, N=77 cells, P<0.001). An interesting pattern emerged when comparing suppression across a neuron's tuned response profile, where the amount of suppression mediated by PV neurons was larger when the "control" response strength was greater (Figure 4.3F). Plotting the relative suppression at each orientation vs. the control response revealed a linear relationship with

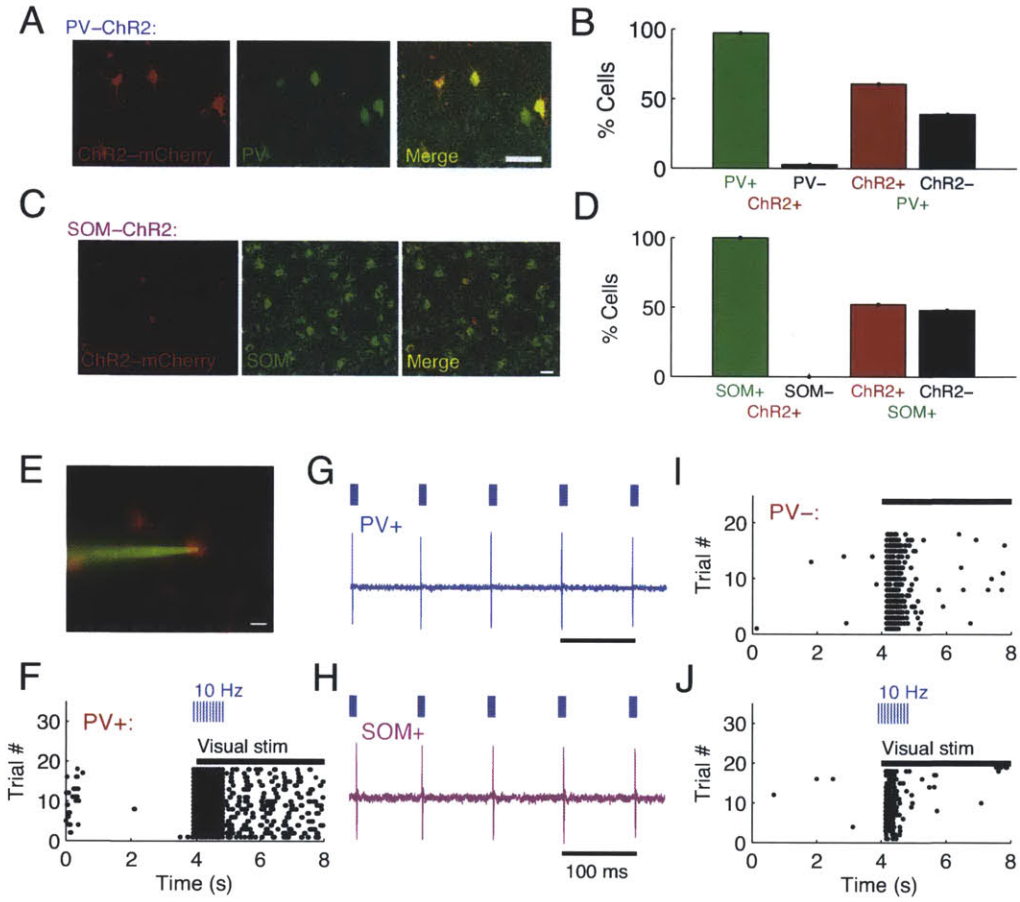

Figure 4.2. PV and SOM neurons were specifically and reliably activated with ChR2. (A) Optogenetic targeting of parvalbumin-containing (PV+) neurons witJ mCherry-channelrhodopsin (mCherry-ChR2) using Cre-lox technology. Cells expressing mCherry-ChR2 also expressed PV. Scale bar: 50 μm. (B) 97% of mCherry-ChR2+ cells were PV+, and 61% of PV+ cells inside the injection site were also mCherry-ChR2+. (C) Expression of mCherry-ChR2 was similar in somatostatin-containing (SOM+) neurons. Cells expressing mCherry-ChR2 also expressed SOM. Scale bar: 50 μm. (D) 100% of infected cells were SOM+, and 52% of SOM+ cells were also mCherry-ChR2+ inside the injection site. (E) In vivo targeted cell-attached recording of a mCherry-ChR2+ PV+ cell. Scale bar: 15 μm. (F) Evoked action potentials from a mCherry-ChR2+ PV+ cell. PV+ neurons were activated at the onset (3.9 s) of 4 s of visual stimulation, through 10 Hz stimulation of the PV+ neuron. (G) Optical activation of PV+ cells at 10 Hz led to repeatable spiking. Scale bar: 100 ms. (H) In separate experiments, SOM+ neurons were reliably activated following an identical stimulation protocol. Scale bar: 100 ms. (I) Recording of the visual response of a PV- neuron in the control condition. (J) Reduction of spikes during and after PV activation compared to responses during control visual stimulation (I).

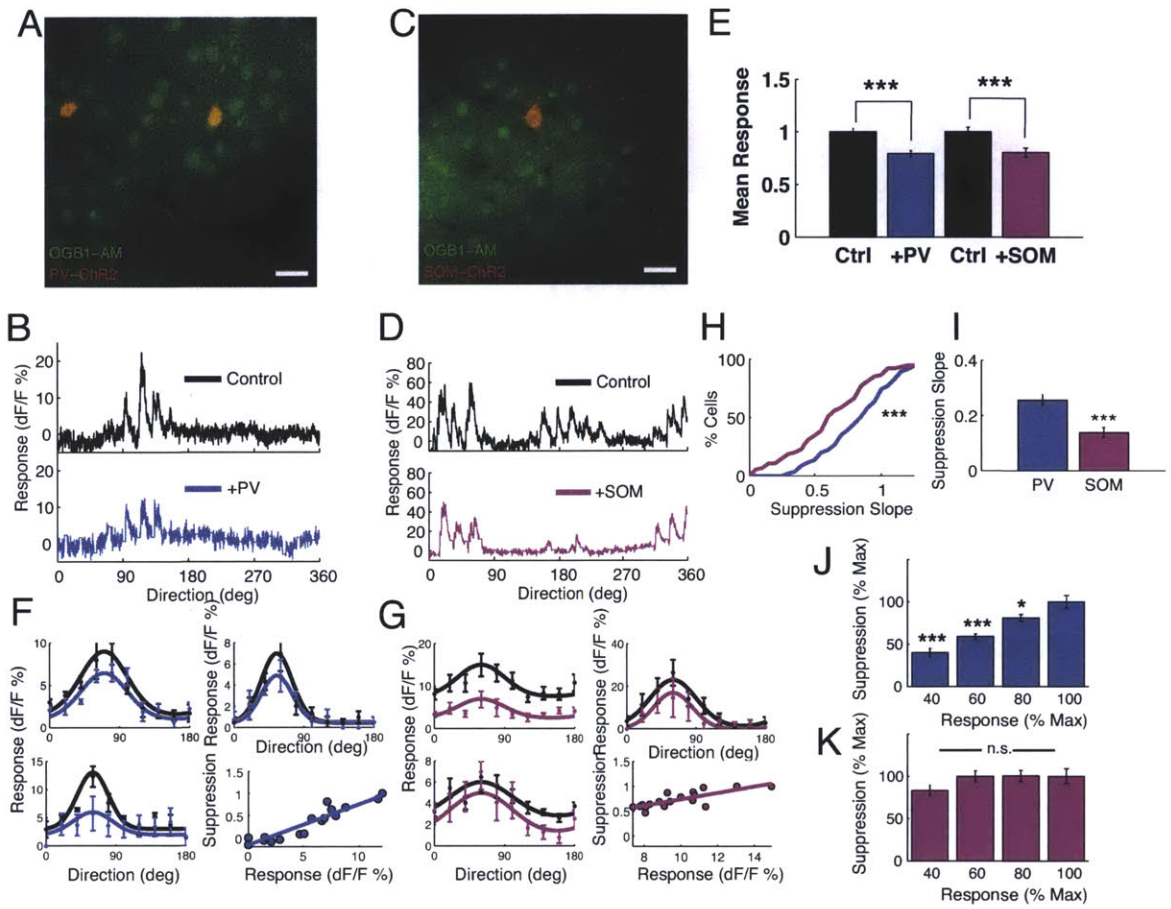

Figure 4.3. Divisive and subtractive inhibition driven by different inhibitory cell classes. (A) An imaging site showing neurons loaded with calcium indicator ("OGB1-AM", green) and two PV+ neurons expressing mCherry-ChR2 ("PV-ChR2", red) that were also loaded (yellow = merged red and green) in visual cortex in vivo. Scale bar = 20 μm. (B) Optical responses to visual stimuli, either without ("Control") or with ("+PV") simultaneous optical PV activation in interleaved trials, recorded during episodically-presented oriented drifting gratings in 18 directions (see Fig. 4.1D). The photo-artifact from ChR2 stimulation has been removed from these trials, as described in the methods. (C) An imaging site showing an mCherry-ChR2+ SOM neuron (yellow = merged red and green) and other neurons (green) loaded with OGB in visual cortex in vivo. Scale bar = 20 μm. (D) Optical responses, either without ("Control") or with ("+SOM") simultaneous optical SOM activation, recorded during the presentation of drifting gratings, as in (B). (E) Normalized to control values, PV and SOM activation ("+ChR2") significantly reduced the peak response in target cells (***P<0.001, *P<0.05). (F) Mean response tuning curves for 3 cells demonstrate that control responses (black) were scaled downward non-uniformly upon PV activation (blue). Larger control responses, at or near preferred stimuli, showed greater suppression. Mean responses (dots) were fit by two Gaussians separated by 180 degrees, and only the preferred direction is shown, centered for comparison purposes. (Lower right plot) The normalized PV-mediated suppression plotted as a function of control response for each stimulus, showing a linear, positive relationship between the cell's activity and amount of suppression. (G) Mean response tuning curves for 3 cells, this time modulated by SOM activation, demonstrating that control responses (black) were scaled downward

more uniformly upon SOM activation (pink). (Lower right plot) The normalized SOM-mediated suppression strength plotted as a function of control response for each stimulus, again showed a linear but relatively flat relationship. (H) Cumulative density plots of the distributions of suppression vs. response slopes for all cells suppressed by SOM activation (pink) and PV activation (blue). P<0.001, Kolmogorov-Smirnov test. (I) The mean suppression slope was significantly higher with PV-activation than with SOM activation (***P<0.001). (J) Relative amount of PV-mediated suppression received at each response strength in the baseline curve, from weakest to strongest, normalized to each cell's maximum. Every bar is significantly different, at either * = P<0.05, or *** = P<0.001, from the bar for highest response. (K) Same as (J), but for SOM-mediated suppression. n.s.: no significant difference is observed between any set of bars.

a positive slope when PV cells were activated (Figure 4.3F). In contrast, SOM activation caused the full response profile to be shifted downward relatively uniformly (Figure 4.3G), particularly when the control responses or baseline levels were high relative to the suppression thereby avoiding a "floor effect". Plotting the relative suppression at each orientation vs. the control response revealed a relatively flat linear relationship between the two when SOM cells were activated (Figure 4.3G). The distribution of these slopes was significantly different between cells suppressed by PV and SOM neurons (Figure 4.3H; p=0.001, Kolmogorov-Smirnov test), and PV activation produced significantly larger slopes (Figure 4.3I; 0.26±0.02) than SOM activation (0.14±0.02, p<0.001).

Comparing the suppression at different response strengths for each cell further demonstrated the asymmetric relationship between response and suppression when PV cells were activated (Figure 4.3J; responses at 40, 60, and even 80% of the maximum response evoked significantly less suppression than at 100% response strength; $P<0.05$ – 0.001 for pair-wise comparisons with suppression at 100% response). In contrast, SOM suppression affected weak and strong stimuli similarly (Figure 4.3K; 40, 60, 80 and 100% response strengths showed no difference in the amount of suppression at each; $P>0.2$). Thus, suppression by SOM cells is relatively uniform across responses of different strengths, whereas suppression by PV cells is non-uniform and proportional to the response level of the target neuron.

4.4.3 Comparison of the impacts of PV and SOM-driven inhibition on the tuning of neuronal responses

This distinction between PV- and SOM-mediated suppression would be expected to impact different aspects of a target cell's response profile and thus stimulus selectivity and physiological function. Proportionate suppression would "scale" responses and reduce the tuning curve's peak amplitude more severely than its spontaneous response level or baseline, whereas uniform suppression would "shift" the entire tuning curve downward, including the baseline.

Indeed, activation of PV and SOM cells uniquely impacted the orientation tuning curves of their target cells (Figure 4.4A). While PV activation caused a decrease in the peak-baseline amplitude of the tuning function, SOM activation had no significant effect (Figure 4.4B; PV: 28.5±4.5% reduction, $P<0.001$, $N=50$ cells; SOM: 19.8±11.2%, $P=0.10$, $N=25$ cells). PV and SOM activation both reduced the baseline response at the non-preferred orientation (Figure 4.4B; PV - 11±4% decrease in baseline, $P<0.05$; vs. SOM - 19±6%, $P<0.001$). PV activation did not affect the tuning width (Figure 4.4C; half-width at half-height, 38.7±3.0 deg control vs. 35.2±3.0 deg +PV, $P=0.31$), while SOM activation significantly narrowed the tuning width of target cells (Figure 4.4C; 45.7±4.1 deg control vs. 37.5±4.3 deg +SOM, $P<0.01$). Similarly, PV activation did not affect the orientation selectivity index (Figure 4.4D; OSI: 0.29±0.01 control vs. 0.29±0.01 +PV, $P=0.71$) or the direction selectivity index (Figure 4.4E; DSI: 0.33±0.03 control vs. 0.36±0.03, P=0.44). SOM activation significantly increased the OSI (Figure 4.4D; 0.26±0.01 control vs. 0.30±0.01 +SOM, $P<0.01$), and showed a trend toward increasing the DSI of target cells (Figure 4.4E; 0.28±0.04 control vs. 0.34±0.05 +SOM, P=0.10). Thus, the relatively uniform suppression by SOM cells leads to a sharpening in response selectivity of target neurons, whereas the non-uniform but proportional suppression by PV cells reduces response magnitude but does not change response selectivity.

These differential effects were not attributable to differing activity levels or tuning properties because peak and baseline neuronal responses of PV and SOM targeted neurons were similar (Figure 4.5; peak responses - PV: dF/F 22.2±1.5%, $N=150$ cells, vs. SOM: 19.5±1.2%, $N=77$ cells; $P=0.32$; baseline responses – PV: 3.70±0.34%dF/F vs. SOM: 3.94±0.50%dF/F, P=0.68), as were the control condition tuning properties (Figure 4.5).

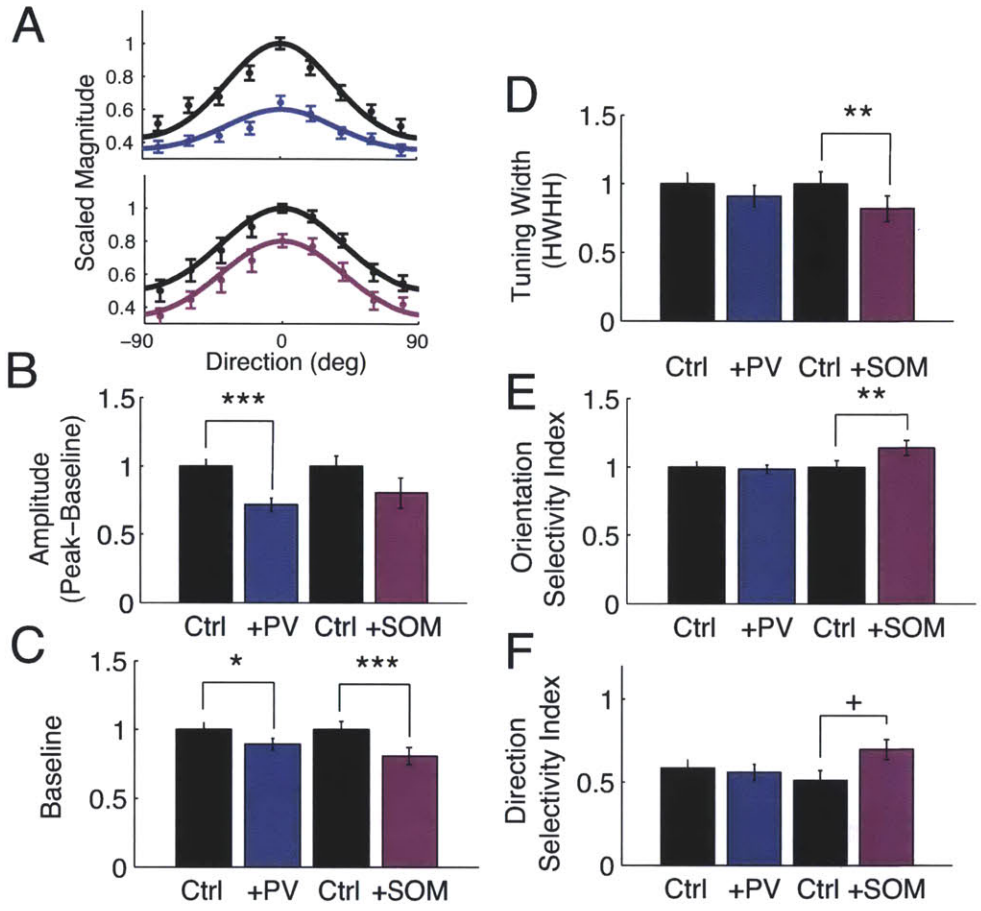

Figure 4.4. PV and SOM activation have unique effects on target cell tuning properties, measured with calcium imaging. (A) Mean tuning curves in control condition (black) and with PV activation (blue, top) and with SOM activation (pink, bottom) reveal the distinction between PV and SOM effects on tuning. (B) Effect of PV and SOM activation on the control tuning curve parameters, obtained from Gaussian fits to the dF/F responses. PV activation reduced the peak-baseline amplitude of the tuning curve ($P<0.001$), while SOM did not ($P=0.10$). (C) Both PV and SOM activation affected the baseline of the tuning curve (PV: $P<0.05$, SOM $P<0.001$). (D) Tuning width, quantified as the half-width at half-height of the Gaussian in the preferred direction, did not change with PV activation ($P=0.31$), while it narrowed with SOM activation ($P<0.01$). Control amplitude ($P=0.69$), baseline ($P=0.59$), and tuning width ($P=0.59$) did not differ between the PV and SOM data. (E) Quantification of the effects of PV and SOM activation on the selectivity of target neurons shows that PV activation did not affect the orientation selectivity index (OSI) ($P=0.71$), while SOM activation significantly increased the OSI ($P<0.01$). (F) The direction selectivity index (DSI) of targets was also unaffected by PV activation ($P=0.44$), and SOM activation showed a trend toward increasing the DSI ($P=0.10$). Control OSIs and DSIs were not significantly different between the PV and SOM data (OSI: $P= 0.21$, DSI: $P= 0.60$).

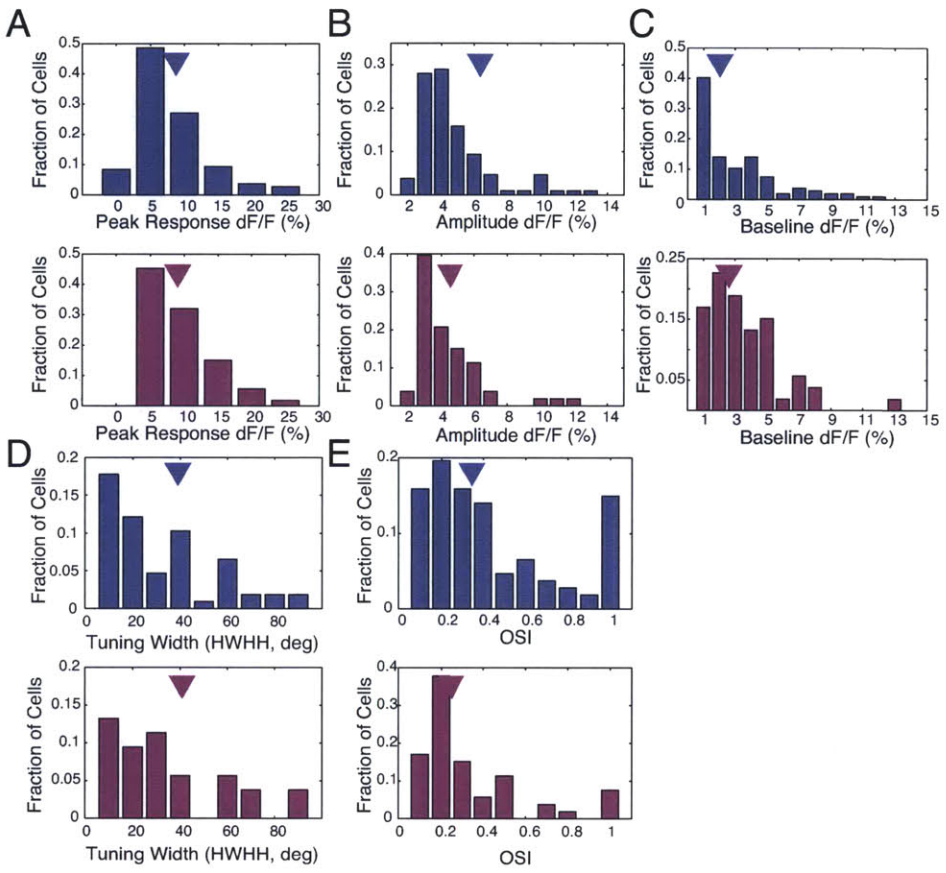

Figure 4.5. PV and SOM target cells have similar control response properties. Properties of cells analyzed in Figure 2 are shown. (A) The control peak response rate was not significantly different between PV (blue) and SOM (pink) target cells (P=0.2). (B) The control peak-baseline amplitude of response was statistically similar between PV and SOM target cells (P=0.59). (C) The control baseline response was statistically similar (P=0.96). (D) The tuning width (half-width at half-height) was similar (P=0.59). (E) The OSI was also statistically similar (P=0.21).

4.4.4 PV and SOM specific effects on target cells examined with electrophysiological recordings

In order to further examine the differential effects of PV and SOM neurons on their targets that were revealed with calcium imaging, we repeated these experiments with electrophysiological cell-attached recordings in vivo, in conjunction with visual and optogenetic stimulation (Figure 4.6A). Putative pyramidal neurons (Figure 4.6B) were identified by their regular spiking properties (Figure 4.6C, The peak:trough ratio of individual spikes was larger for all recorded cells than in identified fast-spiking PV+ neurons (2.82±0.20 for all recorded cells, N=25; 1.41±0.18 in PV+ neurons, N=53, $p<0.001$). The peak firing rates in cells were significantly suppressed by PV and SOM activation (Figure 4.6D, PV: 51.1±1% of Control, N=21 cells, $p<0.001$; SOM: 49.1±1%, N=17 cells, $p<0.001$). Plotting the spike rasters of patched cells to multiple presented orientations (Figure 4.6E-F) allowed us to compare the raw responses in the absence (black) and presence (blue, pink) of ChR2 activation of PV or SOM cells during interleaved control and ChR2 trials. Computing turning curves (Figure 4.6G) again revealed PV-mediated suppression that was non-uniform and depended on the level of the control response, whereas SOM activation shifted tuning curves downward more uniformly (Figure 4.6H). Slopes of the suppression vs. control response lines (e.g. Figure 4.6I-J) were significantly greater for PV-targeted cells compared to SOM-targeted cells (Figure 4.6K, PV: 0.16±0.03, N=21 vs. SOM: 0.06±0.03, N=17, $p<0.05$).

These PV- and SOM- specific suppression patterns again had specific effects on the orientation tuning curves of target cells. While PV activation significantly reduced the peak-baseline amplitude of the tuning curve (Figure 4.7A; 5.8±2.1Hz Control vs. 3.5±1.2Hz +PV, $p<0.05$), SOM activation did not affect it (5.5±1.6Hz Control vs. 5.54±1.2Hz, $p=0.99$). The control peak and baseline responses were similar between the PV and SOM target cells (peak: $p=0.65$, baseline: $p=0.33$). PV activation did not change the firing rate at the baseline of the tuning function (Figure 4.7B; 7.1±5.7Hz Control vs. 6.1±5.1Hz +PV, $p=0.18$), but the baseline was significantly reduced by SOM activation (1.5±0.4Hz Control vs. 0.8±0.3Hz +SOM, $p<0.01$). PV-mediated suppression had no impact on the orientation or direction

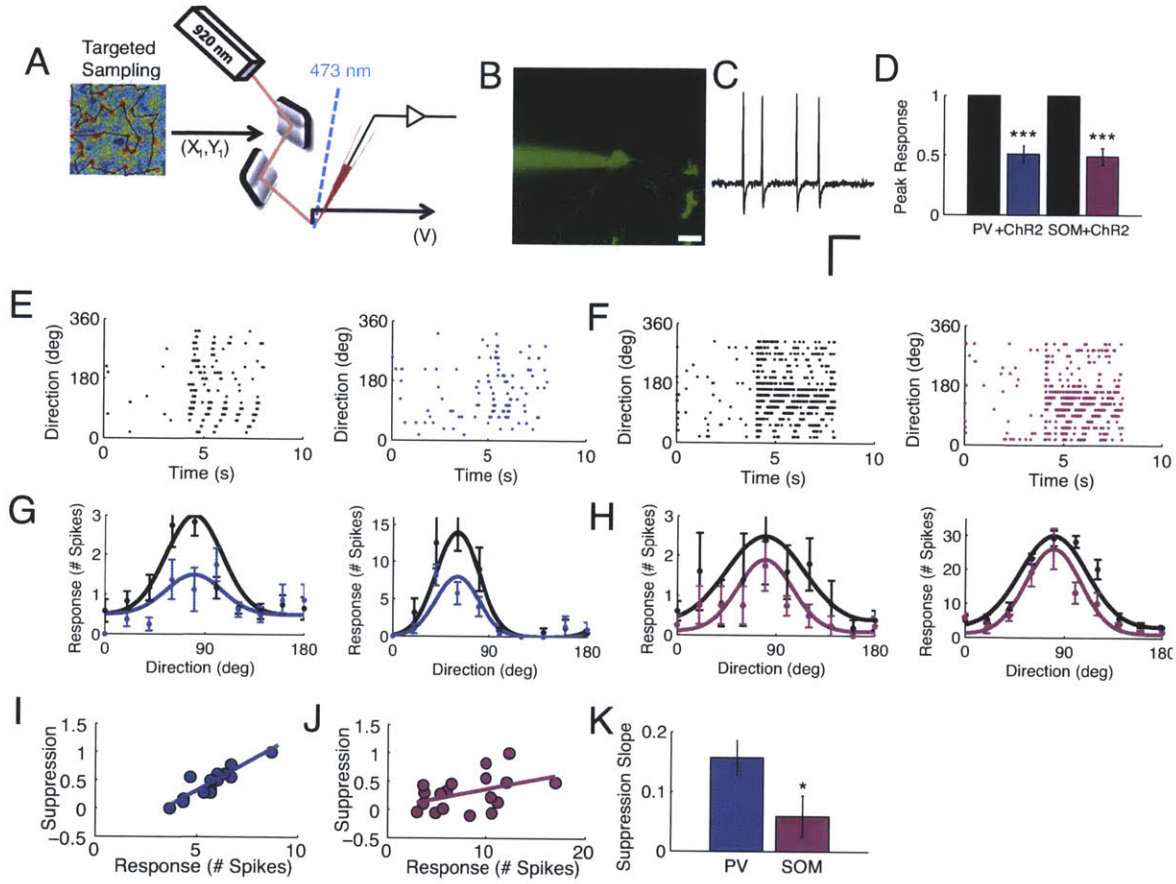

Figure 4.6. Divisive and subtractive impacts of PV and SOM-driven inhibition: electrophysiological recordings. (A) Optically activating PV neurons while recording visual responses using targeted in vivo patch recordings. (B) The image shows a targeted patch under two-photon guidance onto a pyramidal neuron filled with Alexa 488 dye by a pipette filled with the same. Scale bar: 20 μm. (C) Representative spikes recorded in these experiments. Scale bars: 1 mV, 20 ms. (D) Normalized to control values, PV activation ("+ChR2" blue bar) significantly suppressed the peak responses of target cells (***P<0.001). SOM activation ("+ChR2" pink bar) also significantly suppressed the peak responses of target cells (***P<0.001). (E) Raster spike responses for a non-PV cell depicting spikes in time (x axis) over 18 directions (y axis), pooled over multiple trials. Comparing control raster plots (black) to those taken during optogenetic activation of PV neurons reveals suppression in some trials (blue). Time=0 indicates the beginning of the trial, which included a 4-second blank followed by a 4-second orientation presentation. (F) Similarly, raster plots are shown for a sample target of SOM neurons. (G) Control tuning curves (black) were suppressed with ChR2 activation of PV neurons (blue) in two example cells. The tuning curves at left are from the cell in part E. As in Figure 2f-g, the preferred direction is shown for each cell, aligned for comparison purposes. (H) Control tuning curves (black) were suppressed with ChR2 activation of SOM neurons (pink) in two example cells. (I) Representative example of the relationship between suppression with activation and control response strength, with PV activation. (J) Same as (I) for SOM activation. (K) Bar graphs showing that the mean suppression vs. response slopes were significantly higher with PV activation than with SOM activation (*P<0.05).

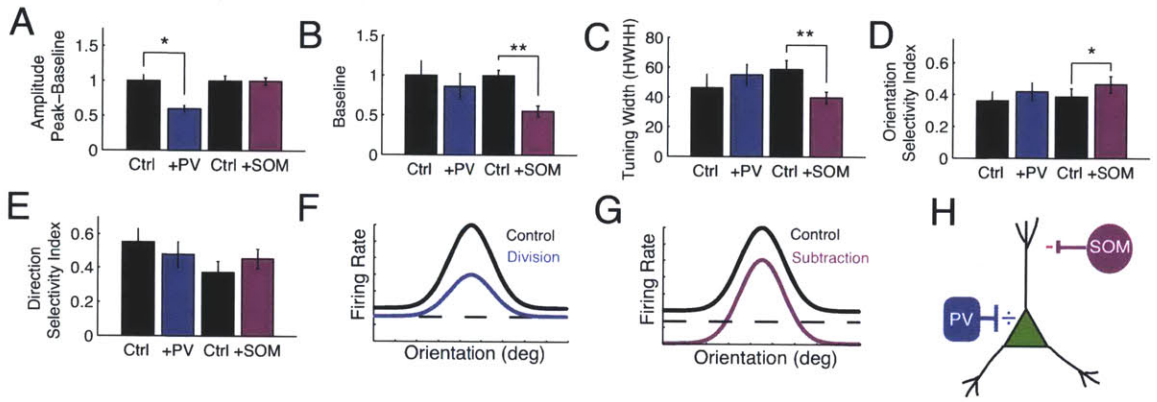

Figure 4.7. Effects of PV and SOM activation on orientation tuning of target cells, measured with electrophysiology. (A) Quantification of the change in tuning curve peak-baseline amplitude during either PV or SOM activation. PV activation resulted in a significant decrease in amplitude (*, $P<0.05$). (B) Quantification of the decrease in the baseline of the entire tuning curve during either PV or SOM activation. PV activation did not change the baseline, but SOM activation decreased the baseline (**, $P<0.01$). (C) Activation of PV neurons did not affect the tuning width (half-width at half-height), while activation of SOM neurons led to significantly more narrow tuning widths (**, $P<0.01$). (D) PV activation did not change the orientation selectivity index (OSI), but SOM activation significantly increased the OSI ($P<0.05$). (E) Neither PV nor SOM activation significantly affected the direction selectivity of target neurons. (F) The effects of PV activation on tuning, a decrease in the amplitude, little change in the baseline, and no change in tuning width or orientation selectivity are consistent with divisive inhibition (blue). (G) The effects of SOM activation, little change in amplitude, decreased baseline, decreased tuning width, and higher selectivity are consistent with subtractive inhibition (pink). (H) Cartoon illustrating a structural dichotomy between the two subtypes that could relate to our functional results. While SOM neurons predominantly target the dendrites of pyramidal cells and produce inhibitory subtraction, PV cells divide and scale the pyramidal cell's net response, perhaps by virtue of their predominantly somatic targeting.

selectivity of target cells, as the tuning width was unchanged with PV activation (Figure 4.7C; 46.1±40.5deg Control vs 54.9±30.1deg +PV, p=0.33) as were the orientation selectivity index (OSI) (Figure 4.7D; 0.36±0.25 Control vs. 0.42±0.25 +PV, p=0.19) and the direction selectivity index (DSI) (Figure 4.7E; 0.55±0.08 Control vs. 0.48±0.08 +PV, p=0.46). SOM activation, however, resulted in narrower tuning widths (Figure 4.7C; 58.6±25.4deg Control vs. 39.7±16.4deg +SOM, p<0.01) and higher OSIs (Figure 4.7D; 0.39±0.21 Control vs. 0.46±0.21 +SOM, p<0.05), though DSIs were not significantly affected (Figure 4.7E; 0.37±0.06 Control vs. 0.45±0.06 +SOM, p=0.31). These measures of orientation and direction selectivity were not significantly different between the control conditions of PV and SOM target cells (OSI: p=0.72, tuning width: p=0.28, DSI: p=0.1).

The net result of these transforms - stemming fundamentally from the observation that SOM-mediated inhibition is relatively independent of control response levels in target cells while PV-mediated inhibition is linearly dependent on control responses - is that inhibition mediated by SOM cells increases response selectivity whereas inhibition mediated by PV cells scales response amplitudes while leaving response selectivity unaffected (Figure 4.7F,GH).

4.4.5 Modulation of gain by PV and SOM-mediated inhibition

The divisive impact of PV activation suggests that PV neurons indeed implement dynamic gain control in cortex, which has been previously attributed to intracortical inhibition (Chance and Abbott, 2000; Murphy and Miller, 2003; Katzner et al., 2011; Atallah et al., 2012; Olsen et al., 2012). Therefore, we carried out cell-attached recordings and examined the modulation of responses with increasing contrast. Such stimuli provide different levels of drive to visual cortex neurons (Figure 4.8A-B), and the saturation of responses with increasing contrast (Figure 4.8B) is a consequence of response gain normalization (Heeger, 1992; Finn et al., 2007; Priebe and Ferster, 2008).

Target cell responses were suppressed by both PV activation (Figure 4.8C; 59±5% of Control, N=17; P<0.001) and SOM activation (75±6%, N=16; P<0.001). Presenting gratings of optimal orientation at increasing contrasts to a patched cell resulted in increasing responses that saturated at a maximal level (Figure 4.8D). PV activation led to a reduction of responses, with curves of similar half-saturation points (Figure 4.8D C50, green circles)

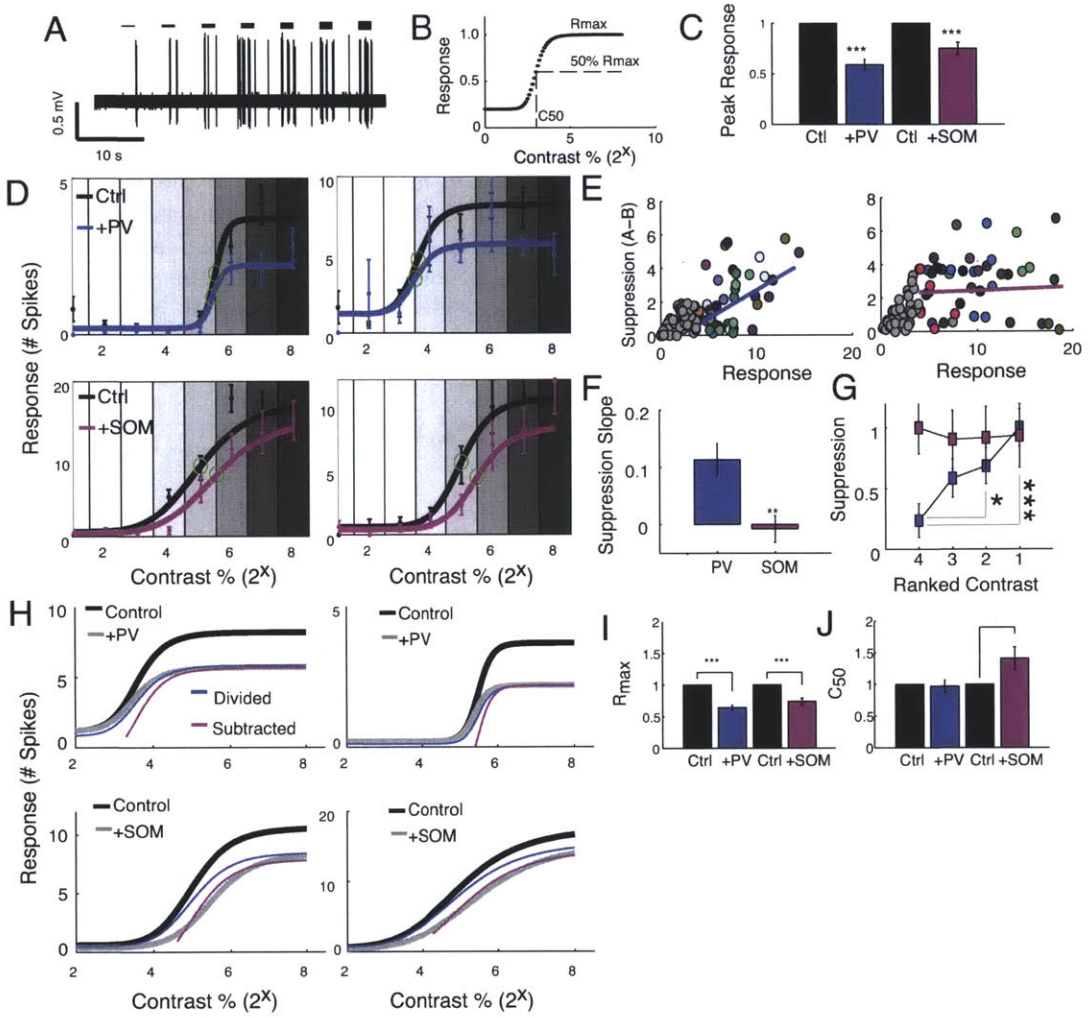

Figure 4.8. Modulation of response gain by PV and SOM cells (A) Visual responses to stimuli of varying contrast were measured in target cells with cell-attached recordings while optically activating PV or SOM neurons. This panel shows an example recording while driving a neuron with drifting gratings of increasing contrast, at the cell's preferred orientation. (B) The growth in firing with increasing contrast was examined as a Naka-Rushton curve with a saturation level (Rmax) and a half-saturation point (contrast of 50% Rmax, C50). (C) As in previous data, both PV and SOM activation significantly decreased the peak visual response (***P<0.001, normalized to the control response). (D) Control contrast-response curves are shown in black; curves with PV activation in blue; with SOM activation in pink. C50 values (green circles) are marked on each curve. PV activation caused a reduction in Rmax but no change in C50, implying a change in response gain, while SOM activation caused the curves to shift down, leading to a shift in C50 toward higher contrasts. (E) Relationship between suppression and response: line plots showing that amount of suppression was a strong function of the response strength (at top 5 contrasts to avoid floor effects) when PV cells were activated (slope=0.25), while the relationship was flat when SOM cells

were activated (slope=0.004). (F) Summary data across all target cells show the mean suppression vs. response slope was significantly larger when PV cells were activated than when SOM cells were activated. (G) When stimuli were ranked by response strength, suppression was equal across all ranks when SOM cells were activated, but ranks with smaller responses tended to have less suppression by PV cells (*P<0.05 when comparing 4th to 2nd strongest contrast; ***P<0.001 comparing 4th strongest to the strongest contrast). (H) The control contrast curves are shown for the same four neurons from above (black lines) and +PV and +SOM (gray lines). Divisive curves obtained by dividing the control curve by a constant to match the Rmax of the +ChR2 curve are shown in blue; subtractive curves obtained by subtracting the control curve by a constant to match the Rmax of the +ChR2 curve are shown in pink. Divisive curves qualitatively match the +PV curves more closely than subtractive curves, while subtractive curves better match the +SOM curves. (I) Summary Rmax data for all cells, showing a significant decrease in Rmax with both PV-ChR2 and SOM-ChR2 stimulation (***, P<0.001). (J) Summary C50 data for all cells showing no change with PV-ChR2 activation but a significant shift in C50 to higher contrasts after SOM-ChR2 activation (*, P<0.05).

but a lower gain (slope) and lower response saturation level (Rmax). SOM activation, on the other hand, resulted in a generalized reduction in the response at all contrasts and a downward shift in the response-contrast curve (with a floor effect at low response levels) (Figure 4.8D).

When we compared the amount of suppression with the control response, we confirmed our findings in the orientation domain (Figures 4.4, 4.7), that PV-mediated suppression was dependent on the response level (Figure 4.8E), but SOM-mediated suppression was relatively independent of the response level (Figure 4.8E). The mean of the population suppression vs. response slopes was significantly higher when PV cells were activated than when SOM cells were activated (Figure 4.8F; PV: 0.11±0.03, N=17 cells vs. SOM: -0.008±0.02 SOM, N=16 cells; P<0.01). Furthermore, when contrasts were ranked by response level, SOM-mediated suppression was uniform across ranks, whereas PV-mediated suppression was strongly dependent on rank (Figure 4.8G, P<0.05 comparing 16% to 64% contrast, P<0.001 comparing 16% to 100% contrast).

The contrast curves with PV activation closely resembled the control curves divided by a constant scale factor (blue lines in Figure 4.8H), while the curves with SOM activation resembled the control curves subtracted by a constant. Averaged across all cells, PV activation scaled response magnitude without affecting half-saturation contrast, yielding a significant difference in Rmax (Figure 4.8I; 64.1±3.5% of control; N=17 cells; P<0.001), but

no difference in C50 (Figure 4.8J; 95.0±10% of control; P=0.65). SOM activation significantly reduced Rmax (Figure 4.8I 73.6±5.3 percent of control SOM+ChR2; N=16 cells; P<0.001), but, unlike PV, also significantly increased C50 (Figure 4.8J; 141±17.7% of control SOM+ChR2; P<0.05), with no effect on the response gain (P=0.23 comparing slopes at C50 before and after SOM activation, vs. P<0.01 comparing slopes of monotonic response-contrast functions before and after PV activation. Across the population of cells, post-PV contrast functions were better fit by a model of division than subtraction (P<0.0001), whereas post-SOM functions were better fit by a model of subtraction than division (P<0.001). Thus, SOM activation shifts responses downward uniformly across contrasts, increasing the contrast required to achieve half-saturation response levels, but leaves the response gain unaffected, while PV activation contributes directly to controlling the gain of target cell responses in multiplicative fashion.

4.5 Discussion

While a growing literature has started to examine the input and firing properties of specific inhibitory neuron classes (Chapter 2 of this thesis, (Kerlin et al., 2010; Ma et al., 2010; Runyan et al., 2010; Hofer et al., 2011; Zariwala et al., 2011)), little is understood about the functional nature of their output. Being able to trigger inhibition and measure its effects on connected cells in the functioning cortex has allowed us to decipher the computational impact of different forms of inhibition on sensory processing. By controlling PV-mediated perisomatic or SOM-mediated dendritic suppression during well-characterized cortical computations underlying vision, and utilizing multiple imaging, optical stimulation and *in vivo* physiology methods, we demonstrate that PV and SOM neurons perform unique inhibitory operations on their target neurons. PV neurons implement divisive normalization, while SOM neurons perform relatively uniform subtraction of responses in their targets. These different canonical computations lead to strikingly complementary effects on neuronal responses: activation of SOM neurons alters stimulus selectivity whereas activation of PV neurons preserves selectivity. PV neurons

modulate response gain whereas SOM neurons shift response levels but leave response gain unaffected.

The role of inhibition in shaping stimulus selectivity of visual cortex neurons has been difficult to resolve with previous methods. Orientation tuning has been proposed to arise from aligned excitatory inputs to V1 neurons, sharpened by the spike threshold (Ferster and Miller, 2000; Priebe and Ferster, 2008). Intracellular recordings in cat and mouse V1 have found closely matched tuning of excitatory and inhibitory synaptic conductances (Anderson et al., 2000; Mariño et al., 2005; Tan et al., 2011), suggesting that inhibition might not sharpen orientation selectivity, and intracellular blockade of inhibition indeed does not affect orientation tuning (Nelson et al., 1994). However, broadly tuned or untuned inhibition can in principle sharpen neuronal responses (Vidyasagar et al., 1996; Sompolinsky and Shapley, 1997); such inhibition has also been described in V1 neurons (Monier et al., 2003; Liu et al., 2011; Xing et al., 2011), and extracellular pharmacological blockade of network inhibition broadens orientation selectivity (Rose and Blakemore, 1974; Sillito, 1979; Tsumoto et al., 1979; Jirmann et al., 2009). Our experiments probed in unbiased fashion the effects of two distinct sources of inhibition on the orientation selectivity of their targets, by optogenetically stimulating them identically in conjunction with all stimulus orientations. Our results show unequivocally that inhibition provided by SOM cells sharpens orientation (and direction) selectivity, while inhibition provided by PV cells affects response strength but does not alter stimulus selectivity.

Inhibition has long been proposed to regulate the gain of cortical responses, and we now demonstrate that PV cells are crucial for this function. Activation of PV neurons influences V1 responses in divisive fashion, across a wide range of stimuli with diverse features (orientations) and drive (contrast). Pharmacological blockade of inhibition alters the response gain of V1 neurons (Katzner et al., 2011), in a manner that is well explained by PV effects. Gain control as a mechanism for regulating or enhancing the dynamic range of responses has been demonstrated in a wide range of cortical areas and functions, pointing to the central role of PV cells in a fundamental property of cortical circuits. In V1, PV-mediated inhibition arises from cells with diverse orientation preferences (Kerlin et al., 2010; Ma et al., 2010), including well-tuned neurons (Runyan et al., 2010; Zariwala et al., 2011). While our study was designed to examine responses evoked by steady-state stimuli

and sustained inhibition, rapid PV-mediated inhibition matched to excitation in time can also shape response gain and even selectivity, as demonstrated in the auditory (Wehr and Zador, 2003; Zhang et al., 2003; Tan et al., 2004), somatosensory (Okun and Lampl, 2008; Gentet et al., 2010) and prefrontal cortices (Haider et al., 2006). Finally, the regulation of response gain by PV cells may be important for developmental regulation of inputs during experience dependent plasticity of cortical circuits (de Villers-Sidani et al., 2008; Yazaki-Sugiyama et al., 2009).

The distinctive effects of PV and SOM inhibition are likely to arise from differences in their cellular zones of impact. SOM neurons form synapses on distal dendrites, while PV neurons tend to target the perisomatic region. When dendritic IPSPs coincide with excitation, as is the case when we stimulate SOM neurons in synchrony with the visual stimulus, inhibition reduces the amplitude of local EPSPs propagating toward the soma (Miles et al., 1996; Tsubokawa and Ross, 1996), or even cancels out the EPSP (Liu, 2004). Thus SOM inputs operate linearly against excitatory inputs along the dendrites, affecting their summation within the dendritic tree (Pouille and Scanziani, 2001; Pouille et al., 2009). Perisomatic IPSPs, however, occurring at the junction of all incoming excitation, are in place to strongly impact spike initiation and firing rate (Miles et al., 1996; Pouille and Scanziani, 2001; Berger, 2003).

4.6 References

Andersen RA, Mountcastle VB (1983) The influence of the angle of gaze upon the excitability of the light-sensitive neurons of the posterior parietal cortex. J Neurosci 3:532–548.

Anderson JS, Carandini M, Ferster D (2000) Orientation tuning of input conductance, excitation, and inhibition in cat primary visual cortex. J Neurophysiol 84:909–926.

Atallah BV, Bruns W, Carandini M, Scanziani M (2012) Parvalbumin-expressing interneurons linearly transform cortical responses to visual stimuli. Neuron 73:159–170.

Bauman LA, Bonds AB (1991) Inhibitory refinement of spatial frequency selectivity in single cells of the cat striate cortex. Vision Res 31:933–944.

Berger T (2003) Timing and Precision of Spike Initiation in Layer V Pyramidal Cells of the Rat Somatosensory Cortex. Cerebral Cortex 13:274–281.

Busse L, Wade AR, Carandini M (2009) Representation of concurrent stimuli by population activity in visual cortex. Neuron 64:931–942.

Carandini M, Ferster D (2000) Membrane potential and firing rate in cat primary visual cortex. J Neurosci 20:470–484.
Carandini M, Heeger DJ (1994) Summation and division by neurons in primate visual cortex. Science 264:1333–1336.
Carandini M, Heeger DJ, Movshon JA (1997) Linearity and normalization in simple cells of the macaque primary visual cortex. J Neurosci 17:8621–8644.
Cardin JA, Carlén M, Meletis K, Knoblich U, Zhang F, Deisseroth K, Tsai L-H, Moore CI (2009) Driving fast-spiking cells induces gamma rhythm and controls sensory responses. Nature 459:663–667.
Chance FS, Abbott LF (2000) Divisive inhibition in recurrent networks. Network (Bristol, England) 11:119–129.
Chance FS, Abbott LF, Reyes AD (2002) Gain modulation from background synaptic input. Neuron 35:773–782.
Crook JM, Kisvárday ZF, Eysel UT (1998) Evidence for a contribution of lateral inhibition to orientation tuning and direction selectivity in cat visual cortex: reversible inactivation of functionally characterized sites combined with neuroanatomical tracing techniques. Eur J Neurosci 10:2056–2075.
de Villers-Sidani E, Simpson KL, Lu Y-F, Lin RCS, Merzenich MM (2008) Manipulating critical period closure across different sectors of the primary auditory cortex. Nat Neurosci 11:957–965.
DeFelipe J, Fariñas I (1992) The pyramidal neuron of the cerebral cortex: morphological and chemical characteristics of the synaptic inputs. Prog Neurobiol 39:563–607.
Deisseroth K (2010) Controlling the brain with light. Sci Am 303:48–55.
Ferster D, Miller KD (2000) Neural mechanisms of orientation selectivity in the visual cortex. Annu Rev Neurosci 23:441–471.
Finn IM, Priebe NJ, Ferster D (2007) The emergence of contrast-invariant orientation tuning in simple cells of cat visual cortex. Neuron 54:137–152.
Freund TF, Buzsáki G (1996) Interneurons of the hippocampus. Hippocampus 6:347–470.
Gentet LJ, Avermann M, Matyas F, Staiger JF, Petersen CCH (2010) Membrane potential dynamics of GABAergic neurons in the barrel cortex of behaving mice. Neuron 65:422–435.
Gonchar Y, Burkhalter A (1997) Three distinct families of GABAergic neurons in rat visual cortex. Cereb Cortex 7:347–358.
Gonchar Y, Wang Q, Burkhalter A (2007) Multiple distinct subtypes of GABAergic neurons in mouse visual cortex identified by triple immunostaining. Frontiers in neuroanatomy 1:3.
Haider B, Duque A, Hasenstaub A, McCormick D (2006) Neocortical Network Activity In Vivo Is Generated through a Dynamic Balance of Excitation and .... J Neurosci.
Heeger DJ (1992) Normalization of cell responses in cat striate cortex. Visual Neuroscience 9:181–197.
Hippenmeyer S, Vrieseling E, Sigrist M, Portmann T, Laengle C, Ladle DR, Arber S (2005) A developmental switch in the response of DRG neurons to ETS transcription factor signaling. PLoS Biol 3:e159.
Hofer SB, Ko H, Pichler B, Vogelstein J, Ros H, Zeng H, Lein E, Lesica NA, Mrsic-Flogel TD (2011) Differential connectivity and response dynamics of excitatory and inhibitory neurons in visual cortex. Nat Neurosci 14:1045–1052.

Isaacson JS, Scanziani M (2011) How inhibition shapes cortical activity. Neuron 72:231–243.
Jirmann K-U, Pernberg J, Eysel UT (2009) Region-specificity of GABAA receptor mediated effects on orientation and direction selectivity in cat visual cortical area 18. Exp Brain Res 192:369–378.
Kapfer C, Glickfeld LL, Atallah BV, Scanziani M (2007) Supralinear increase of recurrent inhibition during sparse activity in the somatosensory cortex. Nature Publishing Group 10:743–753.
Katzner S, Busse L, Carandini M (2011) GABAA Inhibition Controls Response Gain in Visual Cortex. J Neurosci 31:5931–5941.
Kawaguchi Y, Kondo S (2002) Parvalbumin, somatostatin and cholecystokinin as chemical markers for specific GABAergic interneuron types in the rat frontal cortex. J Neurocytol 31:277–287.
Kawaguchi Y, Kubota Y (1997) GABAergic cell subtypes and their synaptic connections in rat frontal cortex. Cereb Cortex 7:476–486.
Kerlin AM, Andermann ML, Berezovskii VK, Reid RC (2010) Broadly tuned response properties of diverse inhibitory neuron subtypes in mouse visual cortex. Neuron 67:858–871.
Klausberger T, Somogyi P (2008) Neuronal diversity and temporal dynamics: the unity of hippocampal circuit operations. Science 321:53–57.
Kubota Y, Hattori R, Yui Y (1994) Three distinct subpopulations of GABAergic neurons in rat frontal agranular cortex. Brain Res 649:159–173.
Kulik A, Vida I, Fukazawa Y, Guetg N, Kasugai Y, Marker CL, Rigato F, Bettler B, Wickman K, Frotscher M, Shigemoto R (2006) Compartment-dependent colocalization of Kir3.2-containing K+ channels and GABAB receptors in hippocampal pyramidal cells. J Neurosci 26:4289–4297.
Lewis DA (2000) GABAergic local circuit neurons and prefrontal cortical dysfunction in schizophrenia. Brain Res Brain Res Rev 31:270–276.
Lillis KP, Eng A, White JA, Mertz J (2008) Two-photon imaging of spatially extended neuronal network dynamics with high temporal resolution. J Neurosci Methods 172:178–184.
Liu B-H, Li Y-T, Ma W-P, Pan C-J, Zhang LI, Tao HW (2011) Broad Inhibition Sharpens Orientation Selectivity by Expanding Input Dynamic Range in Mouse Simple Cells. Neuron 71:542–554.
Liu G (2004) Local structural balance and functional interaction of excitatory and inhibitory synapses in hippocampal dendrites. Nature Publishing Group 7:373–379.
Louie K, Glimcher PW (2010) Separating value from choice: delay discounting activity in the lateral intraparietal area. J Neurosci 30:5498–5507.
Lund JS, Lewis DA (1993) Local circuit neurons of developing and mature macaque prefrontal cortex: Golgi and immunocytochemical characteristics. J Comp Neurol 328:282–312.
Ma W-P, Liu B-H, Li Y-T, Huang ZJ, Zhang LI, Tao HW (2010) Visual representations by cortical somatostatin inhibitory neurons--selective but with weak and delayed responses. J Neurosci 30:14371–14379.
Mariño J, Schummers J, Lyon DC, Schwabe L, Beck O, Wiesing P, Obermayer K, Sur M (2005) Invariant computations in local cortical networks with balanced excitation and

inhibition. Nat Neurosci 8:194–201.
Markram H, Toledo-Rodriguez M, Wang Y, Gupta A, Silberberg G, Wu C (2004) Interneurons of the neocortical inhibitory system. Nat Rev Neurosci 5:793–807.
Miles R, Tóth K, Gulyás AI, Hájos N, Freund TF (1996) Differences between somatic and dendritic inhibition in the hippocampus. Neuron 16:815–823.
Mitchell SJ, Silver RA (2003) Shunting inhibition modulates neuronal gain during synaptic excitation. Neuron 38:433–445.
Monier C, Chavane F, Baudot P, Graham LJ, Fregnac Y (2003) Orientation and direction selectivity of synaptic inputs in visual cortical neurons: A diversity of combinations produces spike tuning. Neuron 37:663–680.
Morrone MC, Burr DC, Maffei L (1982) Functional implications of cross-orientation inhibition of cortical visual cells. I. Neurophysiological evidence. Proc R Soc Lond, B, Biol Sci 216:335–354.
Murphy BK, Miller KD (2003) Multiplicative gain changes are induced by excitation or inhibition alone. J Neurosci 23:10040–10051.
Nelson S, Toth L, Sheth B, Sur M (1994) Orientation selectivity of cortical neurons during intracellular blockade of inhibition. Science 265:774–777.
Ohki K, Chung S, Ch'ng YH, Kara P, Reid RC (2005) Functional imaging with cellular resolution reveals precise micro-architecture in visual cortex. Nature 433:597–603.
Ohshiro T, Angelaki DE, DeAngelis GC (2011) A normalization model of multisensory integration. Nat Neurosci 14:775–782.
Okun M, Lampl I (2008) Instantaneous correlation of excitation and inhibition during ongoing and sensory-evoked activities. Nature Publishing Group 11:535–537.
Olsen SR, Bhandawat V, Wilson RI (2010) Divisive Normalization in Olfactory Population Codes. Neuron 66:287–299.
Olsen SR, Bortone DS, Adesnik H, Scanziani M (2012) Gain control by layer six in cortical circuits of vision. Nature 483:47–52.
Papadopoulou M, Cassenaer S, Nowotny T, Laurent G (2011) Normalization for sparse encoding of odors by a wide-field interneuron. Science 332:721–725.
Pouille F, Marin-Burgin A, Adesnik H, Atallah BV, Scanziani M (2009) Input normalization by global feedforward inhibition expands cortical dynamic range. Nat Neurosci 12:1577–1585.
Pouille F, Scanziani M (2001) Enforcement of temporal fidelity in pyramidal cells by somatic feed-forward inhibition. Science 293:1159–1163.
Priebe NJ, Ferster D (2008) Inhibition, spike threshold, and stimulus selectivity in primary visual cortex. Neuron 57:482–497.
Reynolds JH, Heeger DJ (2009) The normalization model of attention. Neuron 61:168–185.
Rose D, Blakemore C (1974) Effects of bicuculline on functions of inhibition in visual cortex. Nature 249:375–377.
Runyan CA, Schummers J, Van Wart A, Kuhlman SJ, Wilson NR, Huang ZJ, Sur M (2010) Response features of parvalbumin-expressing interneurons suggest precise roles for subtypes of inhibition in visual cortex. Neuron 67:847–857.
Schummers J, Yu H, Sur M (2008) Tuned responses of astrocytes and their influence on hemodynamic signals in the visual cortex. Science 320:1638–1643.
Silberberg G, Markram H (2007) Disynaptic inhibition between neocortical pyramidal cells mediated by Martinotti cells. Neuron 53:735–746.

Sillito AM (1975) The contribution of inhibitory mechanisms to the receptive field properties of neurones in the striate cortex of the cat. J Physiol (Lond) 250:305–329.
Sillito AM (1979) Inhibitory mechanisms influencing complex cell orientation selectivity and their modification at high resting discharge levels. J Physiol (Lond) 289:33–53.
Simoncelli EP, Heeger DJ (1998) A model of neuronal responses in visual area MT. Vision Res 38:743–761.
Somers DC, Nelson SB, Sur M (1995) An emergent model of orientation selectivity in cat visual cortical simple cells. J Neurosci 15:5448–5465.
Sompolinsky H, Shapley R (1997) New perspectives on the mechanisms for orientation selectivity. Curr Opin Neurobiol 7:514–522.
Spruston N (2008) Pyramidal neurons: dendritic structure and synaptic integration. Nat Rev Neurosci 9:206–221.
Tamamaki N, Yanagawa Y, Tomioka R, Miyazaki J-I, Obata K, Kaneko T (2003) Green fluorescent protein expression and colocalization with calretinin, parvalbumin, and somatostatin in the GAD67-GFP knock-in mouse. J Comp Neurol 467:60–79.
Tan AYY, Brown BD, Scholl B, Mohanty D, Priebe NJ (2011) Orientation selectivity of synaptic input to neurons in mouse and cat primary visual cortex. J Neurosci 31:12339–12350.
Tan AYY, Zhang LI, Merzenich MM, Schreiner CE (2004) Tone-evoked excitatory and inhibitory synaptic conductances of primary auditory cortex neurons. J Neurophysiol 92:630–643.
Taniguchi H, He M, Wu P, Kim S, Paik R, Sugino K, Kvitsani D, Fu Y, Lu J, Lin Y, Miyoshi G, Shima Y, Fishell G, Nelson SB, Huang ZJ (2011) A Resource of Cre Driver Lines for Genetic Targeting of GABAergic Neurons in Cerebral Cortex. Neuron 71:995–1013.
Tsubokawa H, Ross WN (1996) IPSPs modulate spike backpropagation and associated [Ca2+]i changes in the dendrites of hippocampal CA1 pyramidal neurons. J Neurophysiol 76:2896–2906.
Tsumoto T, Eckart W, Creutzfeldt OD (1979) Modification of orientation sensitivity of cat visual cortex neurons by removal of GABA-mediated inhibition. Exp Brain Res 34:351–363.
Vidyasagar TR, Pei X, Volgushev M (1996) Multiple mechanisms underlying the orientation selectivity of visual cortical neurones. Trends Neurosci 19:272–277.
Wang X-J, Buzsáki G (1996) Gamma oscillation by synaptic inhibition in a hippocampal interneuronal network model. J Neurosci 16:6402–6413.
Wehr M, Zador AM (2003) Balanced inhibition underlies tuning and sharpens spike timing in auditory cortex. Nature 426:442–446.
Xing D, Ringach DL, Hawken MJ, Shapley RM (2011) Untuned suppression makes a major contribution to the enhancement of orientation selectivity in macaque v1. J Neurosci 31:15972–15982.
Xu X, Roby KD, Callaway EM (2010) Immunochemical characterization of inhibitory mouse cortical neurons: three chemically distinct classes of inhibitory cells. J Comp Neurol 518:389–404.
Yazaki-Sugiyama Y, Kang S, Câteau H, Fukai T, Hensch TK (2009) Bidirectional plasticity in fast-spiking GABA circuits by visual experience. Nature 462:218–221.
Zariwala HA, Madisen L, Ahrens KF, Bernard A, Lein ES, Jones AR, Zeng H (2011) Visual Tuning Properties of Genetically Identified Layer 2/3 Neuronal Types in the Primary

Visual Cortex of Cre-Transgenic Mice. Front Syst Neurosci 4:1–16.
Zhang LI, Tan AYY, Schreiner CE, Merzenich MM (2003) Topography and synaptic shaping of direction selectivity in primary auditory cortex. Nature 424:201–205.

Chapter 5: Mapping the functional targeting of single cortical inhibitory interneurons *in vivo*[1]

5.1 Summary

Because most studies of the connectivity of inhibitory neurons have been restricted to *in vitro* paired electrophysiological recordings or anatomical reconstructions, little is understood about the specificity of inhibitory to excitatory connections. Here, we developed a system to optically activate single channelrhodopsin-2 (ChR2) expressing neurons while recording calcium responses in the surrounding population with two-photon imaging. We could then assess the functional impact of a single inhibitory neuron on the visual responses of potential targets within the field of view. We find that neither parvalbumin-positive (PV+) nor somatostatin-positive (SOM+) neurons follow strict distance functions in choosing local targets. Instead, PV+ or SOM+ neurons functionally suppressed spatially random subsets of neighboring cells. PV+ neurons showed a tendency to functionally target neurons with similar response properties, while SOM+ neurons seemed to target more randomly, suggesting that these cell types may use different strategies in interconnecting with the local network.

5.2 Introduction

Previous chapters of this thesis explored the receptive field properties of subtypes of inhibitory interneurons, and the functional impacts of their activity on target cells. We have shown that both soma-targeting PV+ neurons and dendrite-targeting SOM+ neurons can have highly stimulus-specific responses, but that a large subset of PV+ cells is very broadly tuned. Furthermore, we have activated PV and SOM neurons and measured the functional impacts on target cells, finding that PV neurons divisively normalize responses,

[1] The findings of this chapter were under review at *Nature* at the time of submission of the thesis: *Wilson*, Runyan*, Wang, & Sur. (Under Review). Division and subtraction by distinct inhibitory networks in vivo.*

while SOM neurons provide more subtractive inhibition. But what are the targets of PV and SOM neurons?

The connectivity of inhibitory neurons has necessarily been explored *in vitro* in previous studies, where, with a few notable exceptions (Bock et al., 2011; Hofer et al., 2011), the functional response properties of cells in the circuit are unknown. Even these studies only explored the excitatory to inhibitory connections, and not inhibitory to excitatory. Serial electron microscopy (EM) allows the complete reconstruction of a neuron's synaptic connections, providing valuable information about the location and number of synapses an inhibitory neuron makes on its targets, but cannot describe the functional impact of an inhibitory neuron's action potential on its targets. Early EM studies showed that PV+ basket cells form synapses on the soma, and suggested that they do not form synapses on all nearby pyramidal neurons, but rather might select specific targets (DeFelipe and Fariñas, 1992). Extracellular stimulation of afferent axons combined with whole cell recordings of single neurons *in vitro* has uncovered cortical circuit motifs. For instance, the strong recruitment of layer 4 FS neurons by thalamocortical inputs that results in reliably feedforward inhibition acting nearly simultaneously with feedforward excitation (Inoue and Imoto, 2006), while intracortical excitation cannot as easily stimulate inhibitory circuits (Gil and Amitai, 1996). Dual, triple, or quadruple, whole cell patch electrophysiology in brain slices allows characterization of these connections at higher resolution, measuring the impacts of one neuron's spike on the other(s), but only a few potential connections can be assessed at one time (Tamás et al., 1998; Sun et al., 2006; 2006). Whole-cell patch recordings combined with glutamate uncaging allow the mapping of hundreds or thousands of potential connections (Dantzker and Callaway, 2000; Yoshimura and Callaway, 2005; Yoshimura et al., 2005; Fino and Yuste, 2011; Packer and Yuste, 2011). Still, whether PV+ neurons form specific connections and participate in well-defined subnetworks (Yoshimura and Callaway, 2005) or uniformly blanket the local population with synapses (Packer and Yuste, 2011) remains unresolved.

If these kinds of methods could be employed in the intact brain, we would learn which connections matter in real computations. To date, such methods have been difficult to implement in the intact brain, however, at least on the scale necessary to draw conclusions about the construction of cortical circuits (but see Gentet et al., 2010). Here,

we have developed a system to activate single neurons expressing channelrhodopsin-2 (ChR2) in the intact cortex, while recording the effects on visual responses of nearby neurons using two-photon calcium imaging. We find that functional effects of activated PV and SOM neurons can be detected in only a fraction of the nearby population during online visual computations. Further, PV neurons seem to functionally target neurons with similar orientation preferences, while SOM neurons target cells in the local network randomly.

5.3 Experimental Procedures

5.3.1 Animals

Experiments were carried out in mice, under protocols approved by MIT's Animal Care and Use Committee and conforming to NIH guidelines. Heterozygous SOM-Cre knockin driver mice(Taniguchi et al., 2011), obtained from Jackson Labs (SOM-CreERT2), were backcrossed into a C57BL/6 line. Heterozygous PV-Cre knockin driver mice (Pvalb-Cre, Jackson Labs), which express Cre in over 90% of PV+ neurons, were backcrossed into the same C57BL/6 line (Hippenmeyer et al., 2005).

5.3.2 Surgery: Viral injections

The pAAV-Ef1a-DIO-hChR2(H134R)-mCherry-WPRE-pA live virus was a gift from Dinos Meletis and Marie Carlen in the laboratory of Li-Huei Tsai and subsequently received from the University of North Carolina viral vector core facility.

Six-week old Cre mice were initially anesthetized with 4% isoflurane in oxygen, and maintained on 2% isoflurane. The target coordinates were displaced from Bregma by 3.5 mm posterior and 2.2 mm lateral. The skull was thinned along a 1 mm line at the rostral edge of V1, and the remaining skull and dura were punctured using a glass micropipette filled with the virus. Two injections were made at each site, one at 500 μm below the cortical surface, and one at a depth of 250 μm. A volume of 0.25 μl of virus was injected at 125 nl/min at each depth. After each injection, the pipette was held in place for 5 minutes prior to retraction to prevent leakage.

5.3.3 Surgery: In vivo experiments

Two weeks or more post-injection, mice were re-anesthetized with a cocktail containing fentanyl (0.05 mg/kg), midazolam (5 mg/kg), and medetomidine (0.5 mg/kg), supplemented with isoflurane. The eyes were protected with ophthalmic ointment during the surgery and moistened afterward with saline. A metal head plate was attached to the skull using superglue and dental acrylic, and a 2 mm x 2 mm craniotomy was performed over the primary visual cortex region (area 17). The exposed area was then covered with a thin layer of 2% agarose in ACSF (140 mM NaCl, 5 mM KCl, 2 mM CaCl2, 1 mM MgCl2, .01 mM EDTA, 10 mM HEPES, 10 mM glucose, pH 7.4). Head plates were then screwed into a moveable stage and transferred to the microscope (described below), and 0.5% isoflurane in oxygen was supplied through a tube, with fentanyl/medetomidine injected as needed every few hours. The body temperature was maintained at 37.5 C with a heating blanket (Harvard Apparatus) and supplementary heating pads. The recording phase of physiology experiments typically lasted for 4–6 hr in calcium imaging experiments and 8–12 hr in electrophysiology experiments.

5.3.4 In vivo cell-attached electrophysiological recordings

Recordings were made using custom software (Network Prism, Sur Lab) written in Matlab (Mathworks, Natick, MA) controlling a MultiClamp 700B Amplifier (Axon) that measured differences between a glass pipette electrode inserted into the brain at 20-35^0 and an Ag/AgCl ground pellet electrode (Warner Instruments) positioned in the same solution as the brain and the lens objective. Borosilicate pipettes (outer diameter=1.5mm, inner diameter=1.17mm, WPI) were pulled using a Sutter P-2000 laser puller (Sutter Instruments) to a diameter of 3-7 MΩ. For fluorescent visualization, pipettes were back-filled using capillary action for several minutes with either Oregon Green BAPTA 1-AM (during imaging; see below), Alexa Fluor 488 (100 um, Molecular Probes), or Alexa Fluor 594 (100 um, Molecular Probes). The pipette was targeted to the injection site using a 10x lens, and then targeted to individual cells using a 25x lens via concurrent two-photon imaging at 770 or 920 nm. Cells were either targeted by moving the pipette into the 3D vicinity and then commencing diagonal advance, or cells were patched blindly by advancing diagonally through the cortex. During cell approach, either zero pressure or

light positive pressure was applied. Cell proximity was detected through deflections in electrical resistance observed in voltage clamp during a rapidly time-varying 5 mV command voltage. Once resistance had increased by 5-10 MΩ, slight negative pressure was applied and the pipette was advanced more slowly until resistance increased to 20-100 MΩ. At that point the amplifier was switched to current clamp, and spikes were recorded with zero injected current, under a Bessel filter of 4 KHz and an AC filter of 300 Hz.

5.3.5 Two-photon imaging system

We used a Prairie Ultima two-photon system (Prairie Technologies) driven by a Spectra Physics Mai-Tai eHP laser, passed through a Deep-See module (Spectra Physics / Newport). Laser power was controlled via pockels cell (Conoptics) and guided into the scan head of a modified Olympus BX51WIF microscope using the standard Prairie configuration. The excitation laser tuned to 770 nm-960 nm was then passed through a 660 LP filter, and out through the objective. Received light then passed back through the objective, bounced off of the 660 LP filter, through an IR blocking filter (IR Super-Cold Mirror, 45 mm) and into a PMT separator dichroic mirror (575 LP) which split the signal to a red PMT (with 607/45 barrier filter), or a green PMT (with 525/70 barrier filter). All functional imaging was done using a 25x Olympus XL Plan N (NA = 1.05).

5.3.6 Two-photon imaging: Bulk loading of the calcium indicator

A glass pipette filled with Oregon Green Bapta-1 AM (OGB1-AM, 1.0mM, Molecular Probes, Eugene, OR) and Alexa Fluor 594 (100μM, Molecular Probes, Eugene, OR) was visually guided into the brain and lowered to a depth between 100 and 200μm below the surface, near the center of the viral injection site, and a small amount of dye was released using a picospritzer. The brain was then left undisturbed for at least one hour before imaging.

5.3.7 Two-photon imaging: targeted scan

Following bulk loading (see above), we then used a custom all-Matlab system (Network Visor, Sur Lab) to detect changes in fluorescence associated with cellular activity. Briefly, the red and green PMT BNC cables coming from a two photon microscope (Prairie

Ultima), and carrying fluorescence information, were forked and fed into a custom A/D acquisition system and graphical user interface (National Instruments+Matlab) and sampled at 1.25MHz / channel. The control lines of the two-photon's X and Y galvanometers were in turn substituted with D/A control lines from the custom system. To switch arbitrarily between using the base imaging system and our custom scans, we added a TTL switch that selected which control source was used to control the galvanometer at any time. Finally, the X and Y galvanometer feedback lines were connected to our custom A/D system, to acquire the real-time position (also at 1.25MHz) of the galvanometers to back-attribute the fluorescence signals detected to accurate X,Y positions. Imaging then proceeded under software control by 1) conducting a raster scan to identify cell positions, 2) using machine vision algorithms to cleanly identify and segment the cell bodies, 3) use a genetic algorithm to identify the shortest scan path between cells, and 4) running the scan path rapidly with higher dwell time inside of the cells and faster jumps between cells.
Data was acquired directly into Matlab via custom software (Network Visor, Sur Lab) and saved as .mat files. The laser position vectors were transformed to "cell id" vectors that recognized which moments the laser was within the convex hull borders of each cell, tagging every position at which fluorescence was recorded with a cell id, or no cell id if the laser was passing between cells at that instant. If the laser completed a lap every 0.020 ms (50 Hz), and there were 50 cells, then with 90% dwell time we would excite every cell for 360 us every lap, a significant dwell time. Because we were also sampling at a high rate (1.25 MHz / channel), we collected many samples at every cell during every lap. The imaging parameters that we used for all data were: 1-100 cells, 50 Hz imaging (20 ms per lap), 90% of the 20 ms imaging lap within the cell.

5.3.8 Focal optogenetic stimulation

We built a custom laser stimulation system that was then integrated with our imaging system. First, a diode-pumped solid state blue laser with analog intensity control (473 nm, 200 mW, MBL-III-473, OptoEngine, LLC) was incorporated via fiber optic cable into a two-photon uncaging section of our light path via a readily available FC port (Prairie Technologies) and a 680SP dichroic mirror. This light beam was collimated and aligned

commercially to produce a blue spot size of 5-25 um (Prairie Technologies). Second, an additional set of X,Y galvanometers was intercepted and controlled with a custom photostimulation D/A system built using a National Instruments PCI-6229 data acquisition card, a BNC-2110 breakout box, and a graphical user interface written in Matlab (Network Visor, Sur Lab). Waveforms were sent to control to galvanometers and move the position of the second blue laser spot in X,Y coordinates. Third, the targeted stimulation system was micro-aligned with the imaging system by first centering each beam on a target connected to the objective, and then "burning in" small spots into a fluorescent substrate that was then re-scanned with the imaging system - X,Y offsets that were observed were cancelled out empirically by adding command voltages to the mirror commands to compensate the alignment.

To verify the efficacy and specificity of the targeted system in eliciting spikes from single ChR2+ neurons, we performed cell-attached electrophysiology and imaging recordings from PV and SOM ChR2+ neurons both *in vitro* and *in vivo*, as described above. An XY grid of 10x10 locations at various spatial scales was used to systematically map the spatial activation zone of the neuron, at the soma, as well as along processes at the same scale as the imaging experiments above. In order to test the ability of the targeted laser to elicit spikes from different z-planes, it was focused above the plane containing the cell soma, and the mapping was repeated.

5.3.9 Visual stimulus

Oriented drifting gratings were presented on a 23" 1080p LCD monitor (Dell) using custom software (Network Visstim, Sur Lab) written in ActiveSTIM (Activestim.com) and PsychToolbox-3 (Psychtoolbox.com) on a Windows 7 computer (Dell Precision) with a GeForce 8800 GTS 640MB graphics card (PNY). Gratings were optimized for cellular responsiveness using a contrast of 100%, spatial frequency of 0.002-0.256 cycles/degree, and a temporal frequency of 1-3 Hz. Gratings were then presented by stepping the orientation from 0-360 degrees in steps of 20 degrees, with each grating presentation being preceded for 4 seconds "off" followed by 4 seconds "on", for a total presentation duration of 144 seconds. Each of these "trials" was then repeated with and without optogenetic stimulation, alternating conditions every trial and acquiring between 8-40

trials per cell or network. Optogenetic stimulation preceded the onset of visual stimulus by 100 ms, and consisted of 10 pulses, 10 ms each, at 10 Hz for 1 second. Thus, during every recording sweep, the visual stimulation was on from 4-8 s, and the optogenetic stimulation was on from 3.9-4.9 s.

5.3.10 Data Analysis: Targeted scan imaging

The fluorescence samples collected on each lap within each cell were averaged to create a single data point (F) for every cell during every 0.020 ms lap, and the data points for the cells were collected into F waveforms. The dF/F response was quantified for each stimulus by finding the peak of the response within the "on" period of the stimulus and subtracting the local baseline averaged during the corresponding "off" period of the stimulus. In this manner, dF/F responses for every stimulus were collected for every cell, and grouped according to trials with and without optogenetic stimulation.

5.3.11 Data Analysis: Single cell activation

Control tuning curves were compared to tuning curves from the targeted stimulation condition. For a cell to be considered "suppressed", its control response had to be significantly higher, as determined with a two-tailed paired t-test, $p<0.05$. When assessing the mapping of suppression, (Figure 5.14), the actual percent suppression was used in the analysis of the spatial organization of PV and SOM suppression. The coherence index was calculated for each neuron as the ratio between the distance to the nearest cell and the distance to the nearest cell with similar suppression (within 10%). The local coherence was, for each cell, the mean difference in percent suppression within a 50μm radius. To compare to a re-ordered network, where PV and SOM neurons target according to a simple distance function, suppression values were sorted to decrease monotonically with distance. To compare to a randomly organized network of functional suppression by PV or SOM neurons, suppression values were resampled 10,000 times for each cell with replacement from the original distribution of suppression values for the same network. The mean cumulative probability distribution of this randomized data is plotted in Figure 5.14C, with the borders of upper and lower 95% confidence interval shown.

For the analysis of the tuning of inhibitory cell targeting, the number of cells matching the preferred orientation (± 20 deg) or the orientation orthogonal to the preferred orientation of the inhibitory cell were used to compare the response tuning and targeting of inhibitory neurons. The numbers of targets were then normalized by the number of available targets with that preferred orientation, in order to correct for biases in the local representation of orientation. The targets at the PO vs the nonPO were then compared to a random resampling, where the same orientation distribution was resampled among the cells in each network.

5.4 Results

5.4.1 Activating single ChR2+ inhibitory neurons vivo

To define the functional outputs of single inhibitory neurons, we developed a system to focally stimulate an individual neuron via ChR2 while simultaneously imaging responses of large numbers of neighboring cells. The ChR2-stimulating 473nm laser beam was narrowed to a small effective radius (Figure 5.1A); in acute slices, the effective radius of the blue laser spot was less than 50μm (Figure 5.1B-D). Systematically mapping the efficacy of the blue spot in eliciting spikes further demonstrated its reliable spatial targeting of activation *in vitro* (Figure 5.2) and *in vivo* (Figure 5.3). Targeted cell-attached recordings from ChR2+ cortical inhibitory neurons *in vivo* confirmed the spatial efficacy of the blue laser spot to be well under 50μm even in the intact brain (Figure 5.4). When the blue spot was targeted 100μm directly above the ChR2+ cell body, the spike efficacy of laser stimulation was very poor (Figure 5.4B). Furthermore, calcium dye injections were targeted to the edge of the viral injection site, where mCherry-ChR2 expression was sparse. Careful z-stacks through the cell of interest confirmed that cells in other z-planes virtually never share the same xy location (Figure 5.5). Furthermore, in several instances we recorded from one ChR2+ PV or SOM cell while targeting the blue spot stimulation to a neighboring ChR2+ PV or SOM cell, respectively. In no case did we observe co-activation of the non-targeted ChR2+ neuron, suggesting that in these conditions, activation was not

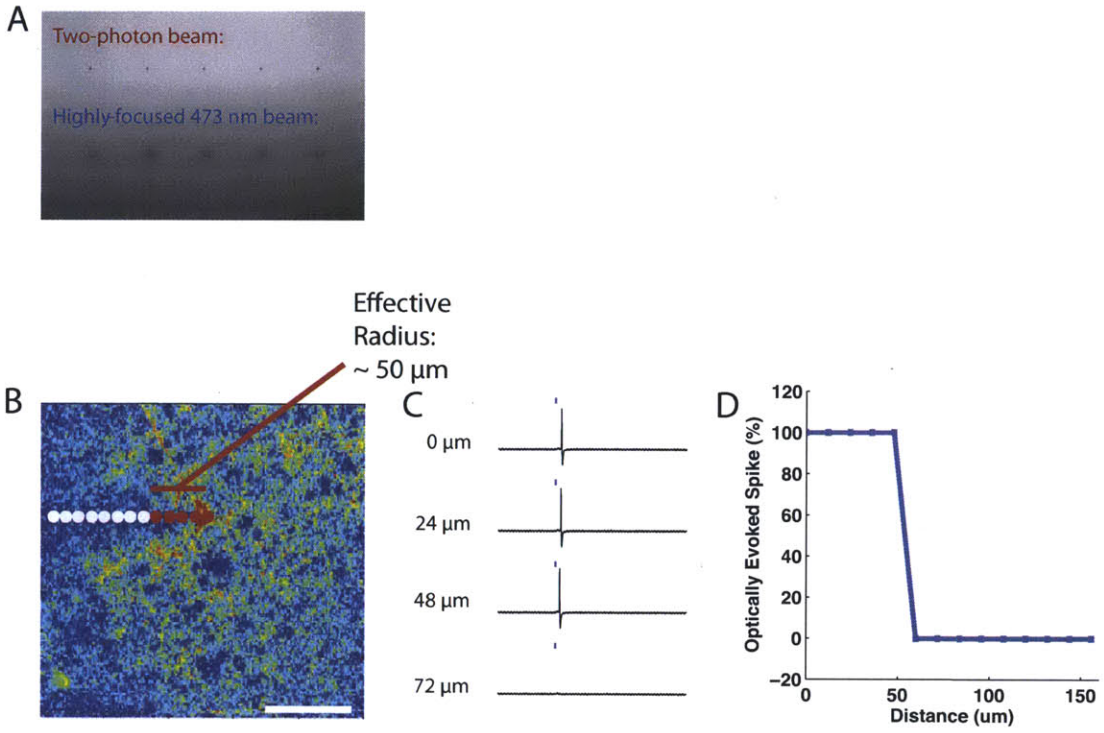

Figure 5.1. Focal laser spot has small effective radius. (A) The point spread function of the stimulation beam was assessed by burning spots into a fluorescent substrate over long durations (minutes), which should provide an upper bound on the maximal area experiencing energy transfer during illumination with the targeted stimulation beam – through the focus and aperture of our optics we were able to get the stimulation beam spread to a scale comparable to that of the 2P beam. (B) Measurement of the functional impact of the beam physiologically. ChR2 was expressed in neurons in acute slices (300 µm) including those deep in the slice, the neuron was visualized under 2P illumination and patched, and the targeted beam was "stepped" towards the neuron until an action potential was detected. Scale bar: 100µm. (C) The beam effectively elicited action potentials at the cell's location; action potentials disappeared when the beam was stepped beyond ~50 um from the cell. (D) Quantification of the experiment in B-C, showing the rapid falloff as the beam left the vicinity of the cell.

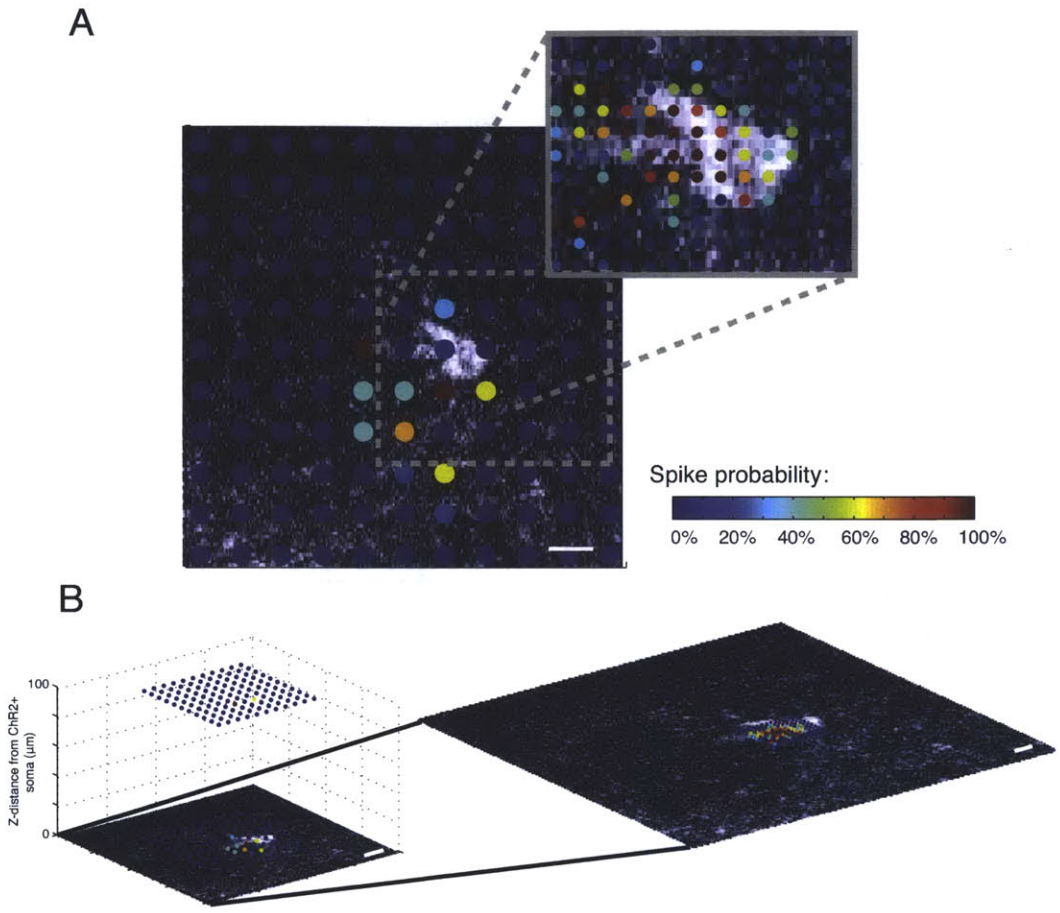

Figure 5.2. Mapping the efficacy of focal laser stimulation of single ChR2+ neurons in vitro. (A) A grid of focal locations spaced ~16 µm apart was used to test the spatial resolution of the focal blue laser stimulation, in terms of spike efficacy, in an acute slice where a ChR2+ SOM+ neuron was recorded in cell-attached mode. The colorbar indicates the spike probability when the blue spot was focused on each location. The smaller rectangle represents a second, higher resolution grid, where locations ~2 µm apart were tested. Scale bar: 15 µm. (B) The same xy mapping of stimulation locations (A) was repeated in a z-plane 100 µm above the plane containing the patched cell body. Scale bar: 15 µm.

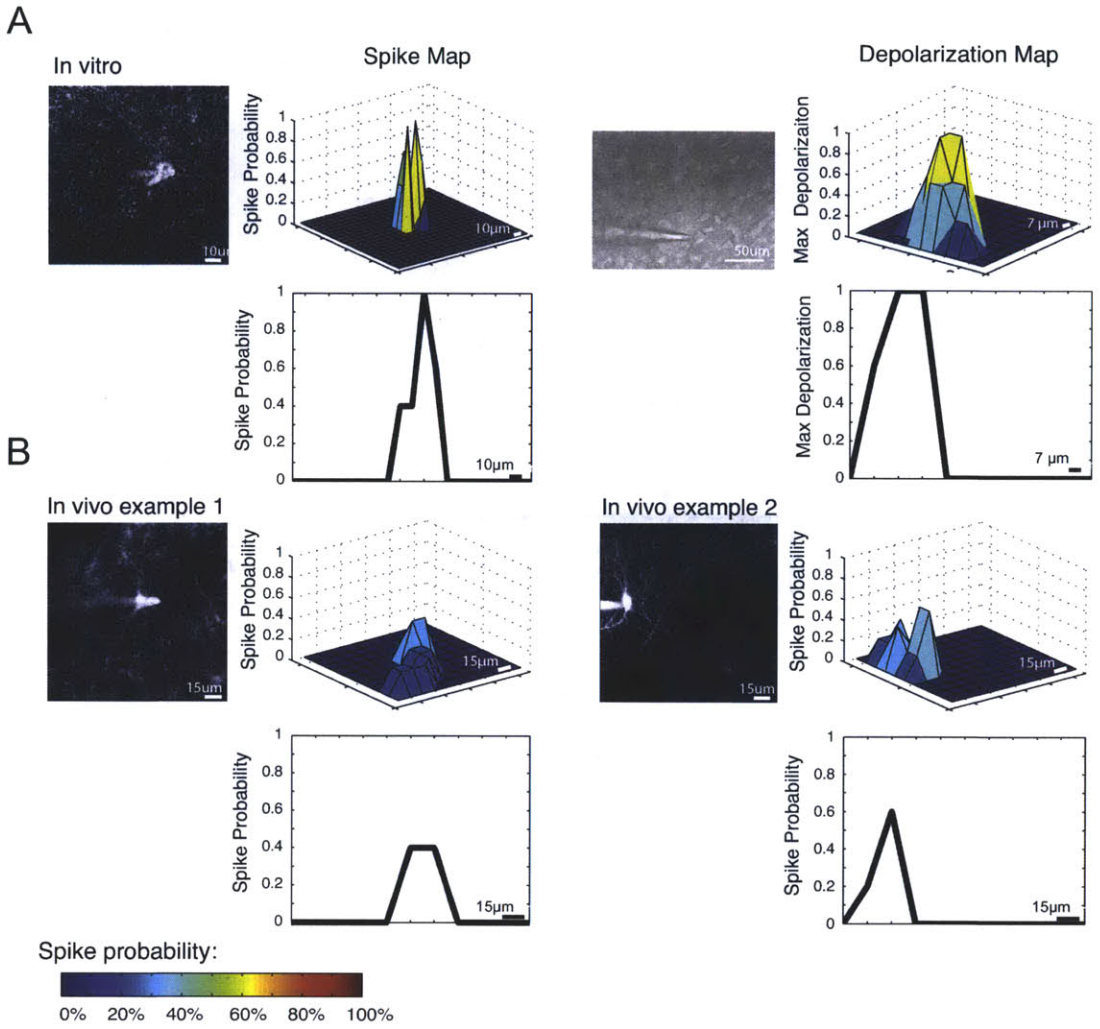

Figure 5.3. Mapping the efficacy of focal laser stimulation of single ChR2+ neurons in vitro and in vivo. Summary of multiple maps in vitro and in vivo for spatial comparison. (A) ChR2+ neurons in acute slices preparations were patched under two-photon guidance, and a grid of xy-focal positions spaced ~16 µm apart evaluated with respect to the effectiveness of the blue laser spot to elicit spikes (left) or detectable depolarization (right) in the patched neuron. Two examples are shown (Left and Right), and a color-coded topography map shows the extent of response at each location. A 2-D line plot of spike efficacy vs. xy distance from the patched neuron demonstrates the specificity of the focal blue laser stimulation. (B) The same mapping of spike efficacy was repeated in vivo, at grid locations spaced 16 µm apart, showing that the laser had to be close to the cell's soma to elicit spikes.

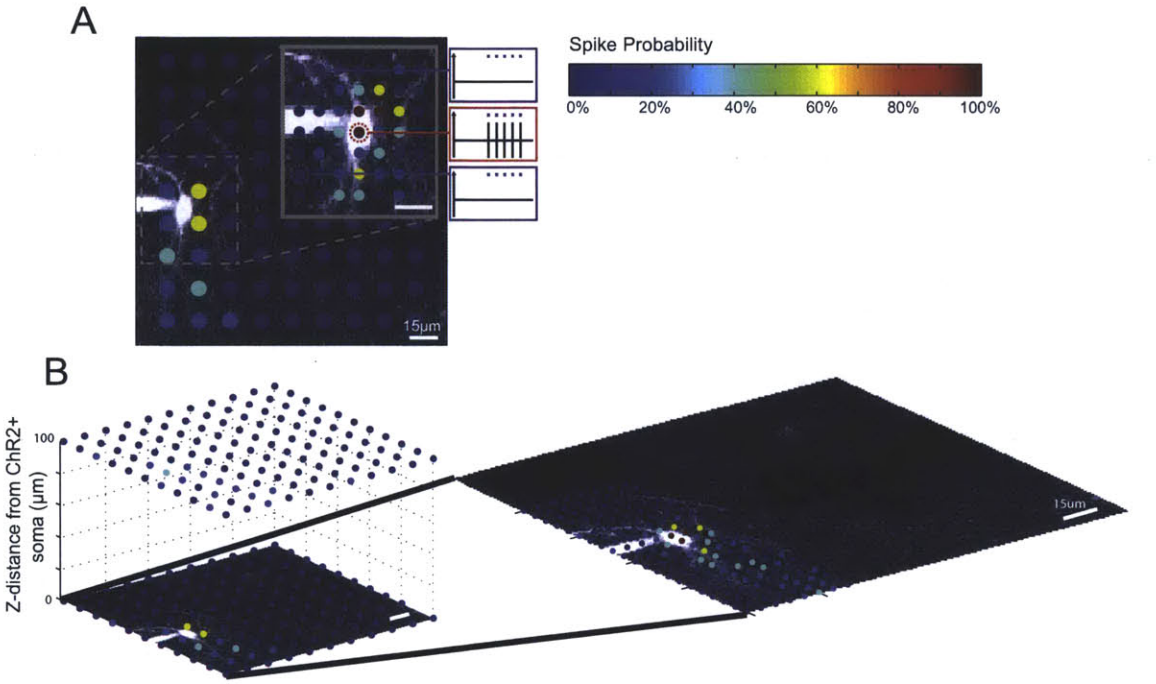

Figure 5.4. Spatial efficacy of blue spot stimulation in single ChR2+ inhibitory neurons in vivo. (A) A SOM ChR2+ neuron in vivo was patched and recorded while systematically mapping the blue spot target locations that caused it to spike. A typical map, at the size of our typical imaging field of view, is shown (larger image), where the focal blue laser was stepped across a grid at 16 µm increments. The inset depicts a higher resolution map taken to extensively map the full extent of activation close to the target cell and its proximal dendrites (indicated by boxed region in larger image), taken at 6.5 µm increments. The tight effective radius in this and other control recordings performed in vivo and in vitro suggest that the effective radius of focal stimulation for typical single cells is <50 µm. This resolution, combined with selection of networks with sparse virus expression, is sufficient for the targeted activation of specific cells. The color bar indicates the spike probability at each location (0-100%). Both scalebars: 15 µm. (B) We mapped the ability of focal blue laser stimulation to elicit spikes both inside and outside the plane of focus that included the ChR2+ neuron's cell body, at 16 µm resolution. The spike probability from locations 100 µm above the neuron was virtually 0 except for one location directly above the cell body (light blue dot in top grid), which elicited spikes with very low probability. Therefore, in order to elicit spikes, even at low probability, from outside of the z-plane of the ChR2+ neuron's cell body, the focal stimulation must be directly above the soma.

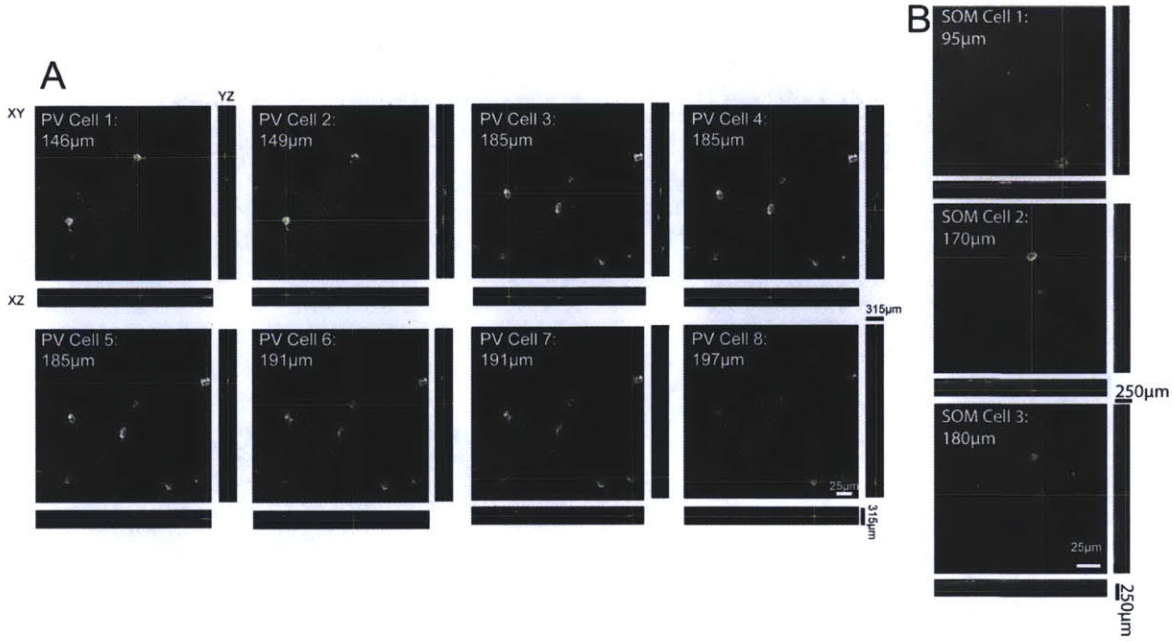

Figure 5.5. The mCherry-ChR2 construct was sparsely expressed in the networks where single cell stimulation was attempted. A-B. Cells were selected for targeting based on careful screening of the area for sparse expression, in both XY and in depth by taking Z stacks. These experiments were also intentionally done in mice with sparse expression. Given the sparse expression of the virally-expressed ChR2 used in our experiments, where neurons at different depths were rarely if ever in the same xy location, it is unlikely that we activated neurons from depths above or below the neuron of interest. Here we show the xy planes from z-stacks that contained mCherry-ChR2+ neurons from a representative PV-Cre mouse (B), where 315 µm of depth were examined at 3 µm increments and a SOM-Cre mouse (C), where 250 µm of depth were examined at 5 µm increments. The cross hairs in each plane indicate the focus of the orthogonal XZ and YZ planes shown to the right and below each image, and show that no other mCherry-ChR2+ neurons were directly above or below any of these neurons.

spreading through gap junctions within the PV+ or SOM+ neurons, but was instead restricted to the targeted cell.

5.4.2 Mapping the functional suppression mediated by single inhibitory neurons in vivo

Confident that we were able to activate single inhibitory neurons with the blue spot, we loaded networks with the calcium indicator dye OGB, and measured the visual responses of populations of cells with and without activation of a single ChR2+ neuron (Figure 5.6). Mapping response modulation across a network while controlling a PV+ neurons, we triggered suppression in some cells (Figure 5.7A-C). Interestingly, scattered within the same network, other cells were unaffected by the focal PV activation (Figure 5.7A-C). We thus established a map of the cells that were significantly modulated during focal PV cell activation (Figure 5.7C). Similar non-uniform maps of functional suppression were obtained from every imaged animal (Figure 5.7D, n = 4 networks). Overall, focal PV activation resulted in the significant suppression of 43.1±2.1% of neurons within the field of view. A similar, nonuniform pattern was observed when single SOM neurons were activated, where significantly suppressed cells existed alongside other cells in the network that were not suppressed (Figure 5.8A-C). Focal stimulation of SOM neurons resulted in significant suppression of 16.2±2.9% of neurons within the field of view (Figure 5.8D, n = 5 networks). Defining "suppressed" cells by a simple threshold (15, 30, 60% suppression) rather than using the significance test resulted in qualitatively similar (nonuniform) suppression maps for both PV (Figure 5.9) and SOM neurons (Figure 5.10). PV and SOM activation rarely caused disinhibition in neighboring neurons, and so indirect effects were not considered further (Figure 5.11). Electrical stimulation of a single ChR2+ SOM cell with a patch electrode yielded a similar suppression map (12% of cells suppressed, Figure 5.12). These maps reveal a remarkable diversity in the functional suppression mediated by single PV or SOM neurons within their local neighborhoods.

5.4.3 Uncovering rules of functional connectivity by inhibitory neurons

Is there an underlying rule by which an inhibitory cell makes functional connections with its targets? Recent reports in brain slices have suggested that inhibitory connectivity arises from a distance rule, where cell-to-cell connectivity is determined by how far away

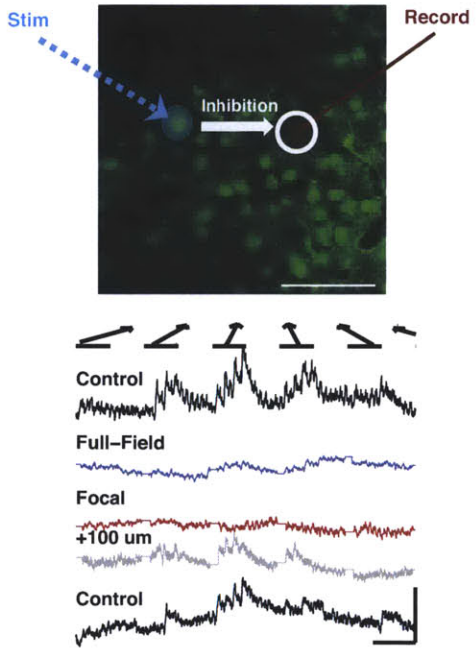

Figure 5.6. All-optical circuit mapping. Optical activation of one neuron (blue arrow) during targeted recording of another neuron (red arrow). Scale bar: 50μm. Calcium responses in neighboring neurons could be measured during the control condition (black), during full-field ChR2 activation (blue), during focal activation of the PV+ cell (red), or when the focal blue laser spot had been focused away from the PV+ cell (gray). Scale bars: 5sec, 20% dF/F.

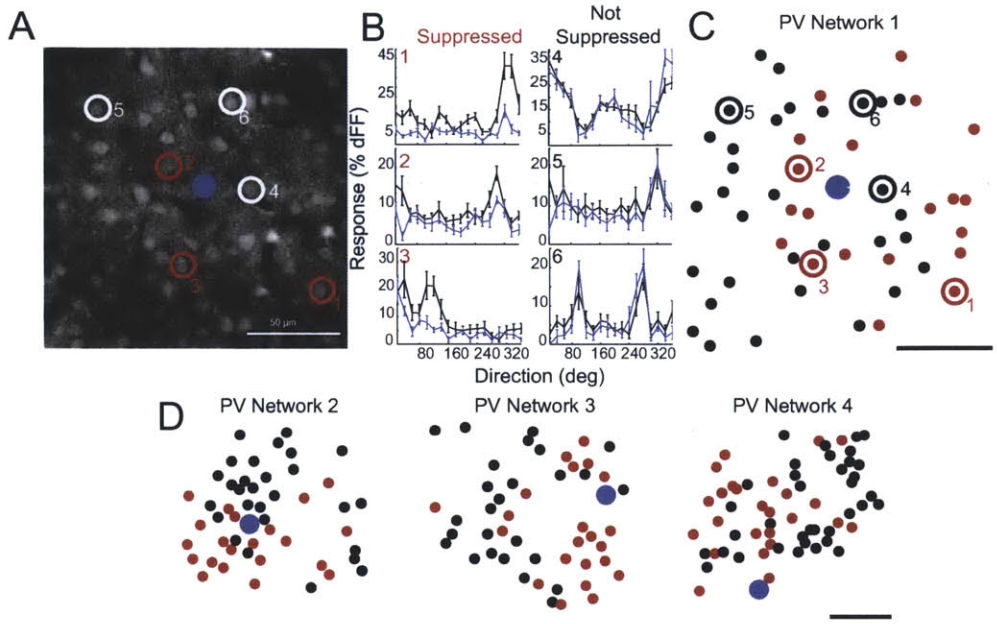

Figure 5.7 Mapping the functional influence of single targeted PV neurons on local networks. (A) Some cells that were significantly suppressed by PV activation (red, 1-3) which were clearly intermixed with other nearby cells that were not affected (white, 4-6). Scale bar: 50 μm. (B) Mean tuning curves for cells 1-6 comparing cell responses during control (black) or single PV cell activation (blue). Mean tuning curves for significantly suppressed cells 1-3 ("Suppressed", left), and unaffected cells 4-6 ("Not Suppressed", right). (C) Spatial distribution of all cells in the network that were either significantly suppressed (red) or not (black). Cells that were not suppressed were intermingled at a variety of distances with cells that were suppressed. Scale bar: 50 μm. (D) Spatial distributions of cells in three other networks where blue laser stimulation was focused on the PV cell indicated in blue. As in part C, red circles indicate significantly suppressed neurons.

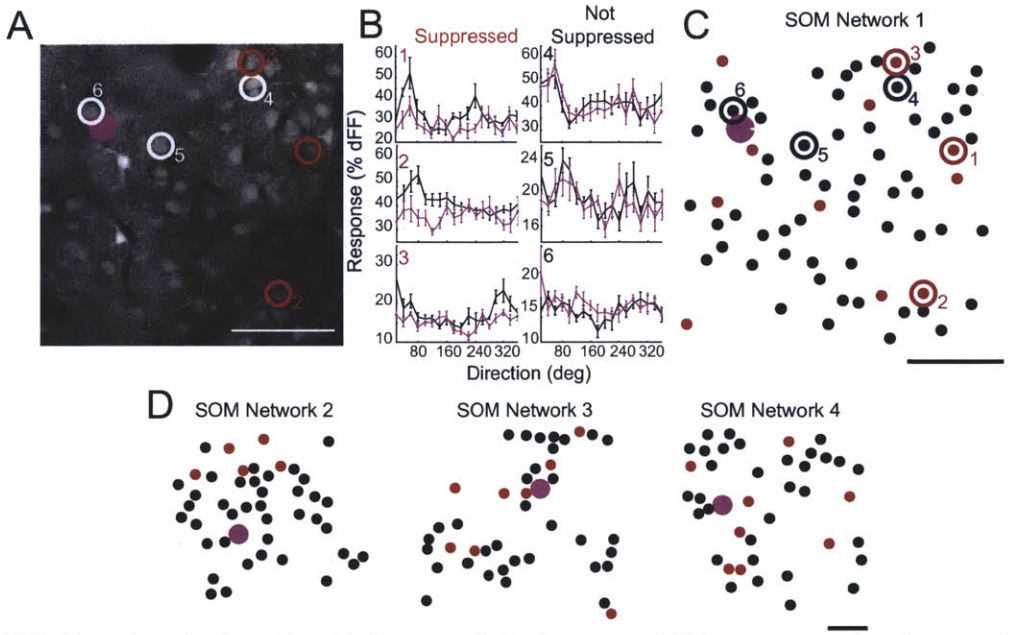

Figure 5.8. Mapping the functional influence of single targeted PV neurons on local networks. (A) In parallel experiments, the blue laser spot was focused on a specific SOM neuron (pink). Mapping the influence on neighboring cells again revealed some cells that were significantly suppressed (red, 1-3) which were clearly intermixed with other nearby cells that were not affected (white, 4-6). Scale bar: 50 μm. B. Mean tuning curves from three significantly suppressed neurons (left column) and three unaffected neurons (right column). Black lines indicate responses under control condition, pink lines indicate responses measured while the indicated SOM cell in H was targeted for activation. C. The spatial distribution of all significantly suppressed cells revealed a sparse and diffuse distribution of suppression. Scale bar: 50 μm. D. Spatial distributions of cells in three other networks where blue laser stimulation was focused on the SOM cell indicated in pink. Scale bar: 50 μm.

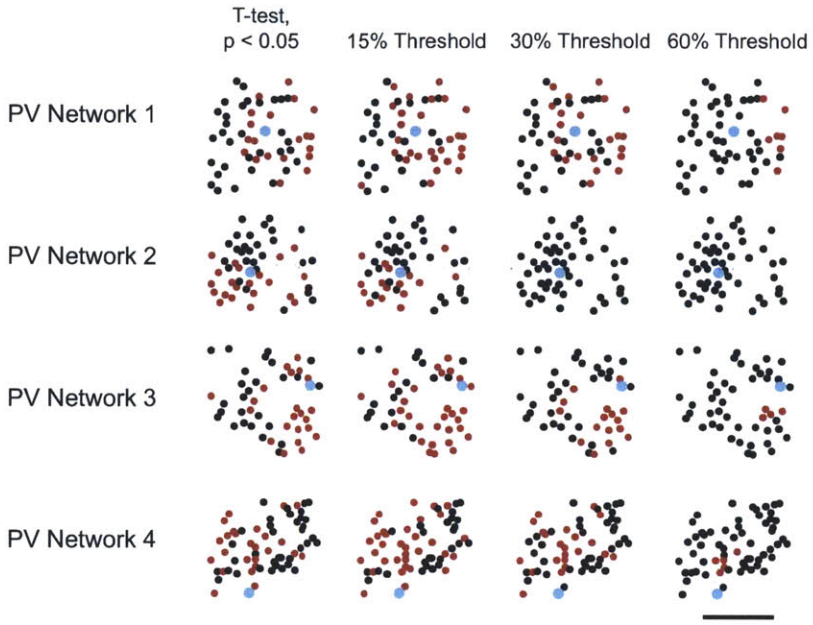

Figure 5.9. Heterogeneous mapping of PV cell influence remains with different thresholds of suppression. The original data in Figure 5.7 was acquired by activating a single cell in the network (colored blue, PV), and concurrently imaging the other cells' visual responses to quantify their suppression by the activated cell, to assess the spatial organization of sizeable suppression. In Figures 5.7-5.8, significantly suppressed cells were identified by paired t-tests, comparing responses at the preferred orientation +/- 20 degrees. Here, for comparison the same data are plotted for all networks measured comparing significantly suppressed cells (red) vs. non-suppressed cells (black) (left column), as well as when suppression is defined using different thresholds for the amount of suppression (%) rather than a significance test. We find that the heterogeneous spatial pattern of suppression, where neighboring cells can be either suppressed or not, remains regardless of the suppression definition that is employed. Scale bar: 50μm.

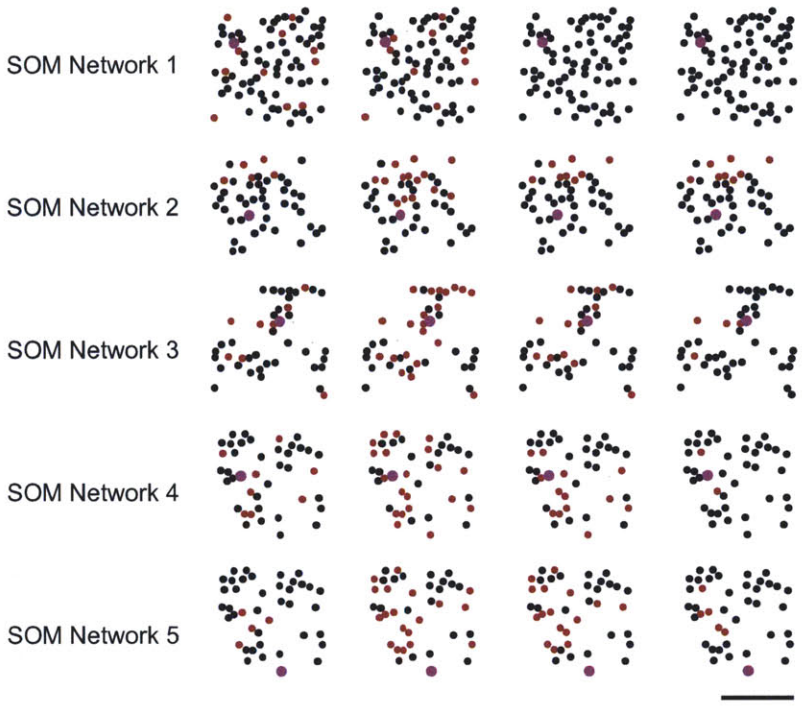

Figure 5.10. Heterogeneous mapping of SOM cell influence remains with different thresholds of suppression. The original data in Figure 5.8 was acquired by activating a single cell in the network (pink, SOM), and concurrently imaging the other cells' visual responses to quantify their suppression by the activated cell, to assess the spatial organization of sizeable suppression. In Figures 5.7-5.8, significantly suppressed cells were identified by paired t-tests, comparing responses at the preferred orientation +/- 20 degrees. Here, for comparison the same data are plotted for all networks measured comparing significantly suppressed cells (red) vs. non-suppressed cells (black) (left column), as well as when suppression is defined using different thresholds for the amount of suppression (%) rather than a significance test. We find that the heterogeneous spatial pattern of suppression, where neighboring cells can be either suppressed or not, remains regardless of the suppression definition that is employed. Scale bar: 50μm.

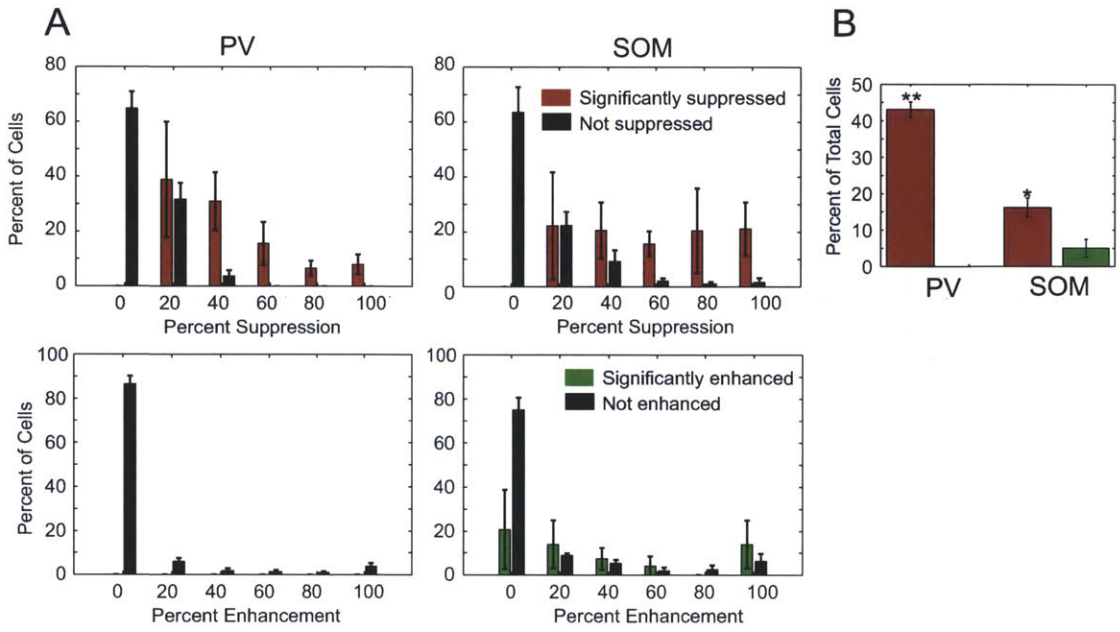

Figure 5.11. Disinhibitory effects were rare with focal activation of PV and SOM neurons. (A) For PV (left column) and SOM networks (right column), histograms showing the distribution of suppression (top) or enhancement (bottom) strengths for significantly affected (red, green bars) and unaffected neurons (black bars). As expected, significantly affected neurons tend to show more suppression or enhancement than unaffected neurons. (B) Significantly enhanced neurons were not found in any PV network, and were relatively rare in SOM networks. Significantly more neurons were suppressed by SOM neurons than were enhanced ($P<0.05$). Interestingly, PV neurons tended to suppress a larger number of neurons than SOM neurons did ($P<0.05$).

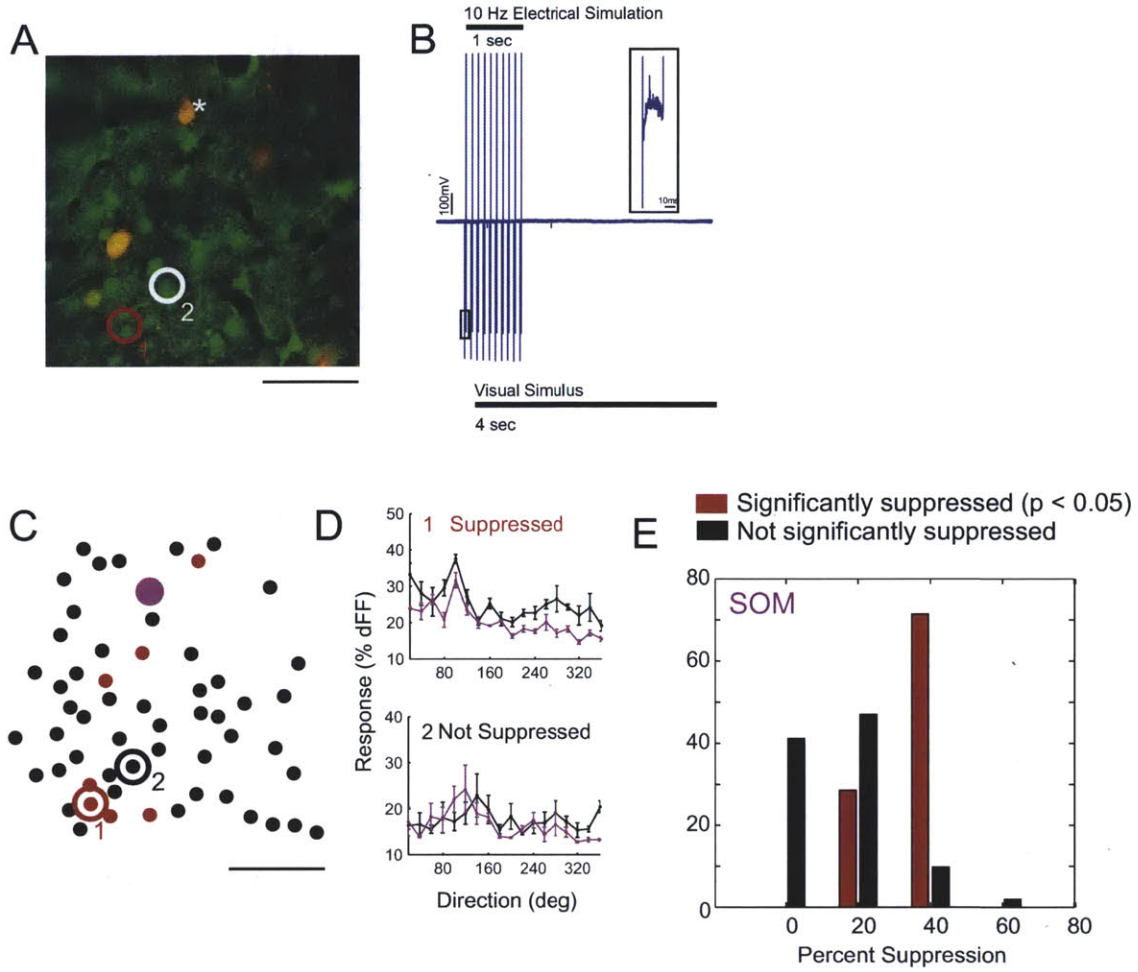

Figure 5.12. Targeted electrical stimulation of a SOM+ neuron shows its map of functional suppression. (A) A SOM neuron was loose-patched in a network loaded with calcium indicator. (B) The cell was stimulated electrically at 10 Hz with 10 pulses of 5 nA amplitude and 0.02 s width. This 10 Hz electrical stimulation was delivered to mimic the single cell blue spot stimulation of Figure 5, where the stimulation of the single SOM or PV cell was delivered starting 100 ms prior to each visual stimulus. As can be seen from the inset, approximately 1 spike per pulse was elicited. (C) The spatial distribution of significantly suppressed neurons (red) and unaffected neurons (black) is shown for the network in B. As for the blue laser spot stimulation in Figure 5, the suppressed cells are intermingled with unaffected cells. (D) An example of a significantly suppressed (top) and unaffected neuron (bottom) is shown. Black lines indicate the orientation tuning response in the control condition, and pink lines indicate the response when the SOM cell was electrically stimulated. (E) Histograms show the suppression strength of significantly suppressed (red bars) and unaffected neurons (black bars) when the SOM neuron is electrically stimulated. No cells showed an enhancement of response. Scalebars in A, C = 50 μm.

cells are from the inhibitory cell under consideration (Fino and Yuste, 2011; Packer and Yuste, 2011). We therefore examined whether the spatial pattern of suppression that we observed *in vivo* could be predicted by such a distance rule. We first compared the distribution of suppressed cells to the distribution of total cells within equally spaced distance bins from focally stimulated PV cells and stimulated SOM cells (Figure 5.13A). The distribution of suppressed cells was flat with distance from focally activated PV cells (distances<100μm, n = 4 networks, p = 0.20, r = -0.61), and from focally activated SOM cells (distances<100μm, n = 5 networks, p = 0.06, r = -0.56). We further examined the hypothesis that even if the proportion of connected cells remained constant within the local network, perhaps PV and SOM cells made stronger functional connections and thus more strongly suppressed nearby cells than those that were farther away. For each network, we plotted the suppression strength against each cell's distance from the PV or SOM cell (Figure5.13B). While individual networks could show small positive, negative, or flat relationships between suppression strength and distance, no significant relationship between suppression strength and distance was found for the pooled population of PV and SOM target cells (PV: p = 0.80, r = -0.03, 4 networks; SOM: p = 0.1, r = -0.28, 5 networks). Thus, individual PV and SOM neurons do not seem to target neurons along a distance gradient within their local network.

To better understand the mapping patterns of PV- and SOM-mediated suppression, we next compared the spatial pattern of suppression in each network ("actual suppression map", Figure 5.14A, left) to a theoretical "ordered" network predicted by implementing a monotonic distance function containing the measured suppression values in that network ("ordered distance model", Figure 5.14A, middle) or a theoretical network with a random distribution of suppression ("random model", Figure 5.14A, right). While some structure could be detected in each actual network, the coherence observed in all "actual networks" was significantly lower than that of the ordered networks, and more closely matched the random networks in all PV and SOM cases (Figure 5.14B). Examining the distribution of local coherence revealed that the actual networks were well within the confidence intervals of the randomized networks' coherence, but significantly different from the theoretical ordered network (Figure 5.14C). Thus, the local functional targeting of both inhibitory neuron subtypes cannot be described by a simple distance relationship.

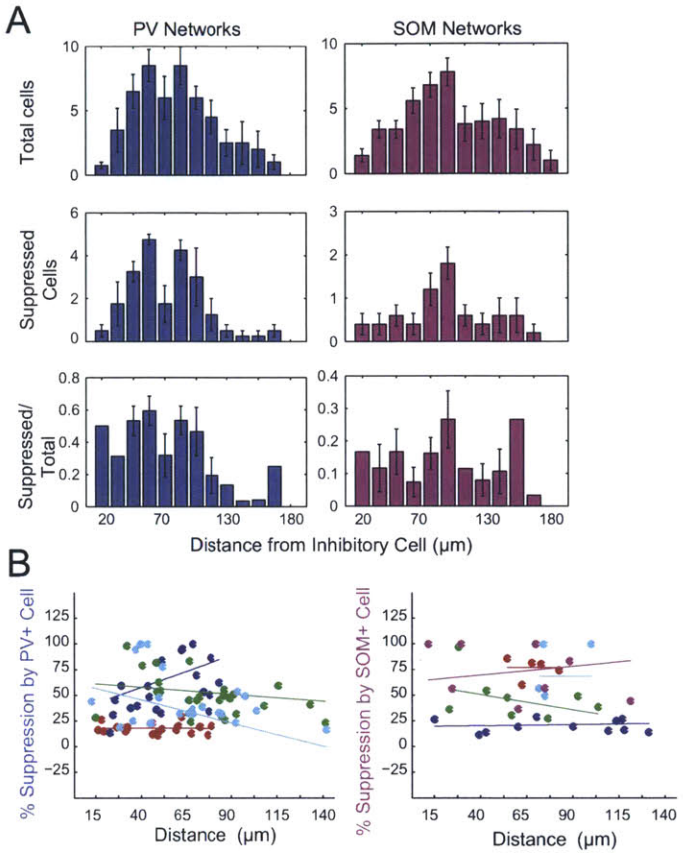

Figure 5.13. Distance analysis of the functional targeting by PV and SOM neurons. (A) (Top) Histograms showing the mean distribution of distances of all cells in the field of view from the stimulated PV cells (left, blue histogram, N=4 networks) or from the stimulated SOM cells (right, pink histogram, N=5 networks). (Middle) Histograms showing the distribution of distances of significantly suppressed cells from the stimulated PV or SOM cells. (Bottom) Histograms showing the proportion of suppressed cells to total cells binned by distance from the focally stimulated inhibitory cell. Considering only distances up to 100 μm, which excludes edge effects, the proportion of suppressed cells remains constant for PV (r=-0.61, P= 0.20) and SOM (r = -0.14, P= 0.79). At farther distances, where contaminating edge effects may skew results, the proportion of suppressed cells fell with distance from the PV cell (N=4 networks, r=-0.67, P<0.05) and tended to fall with distance from the SOM cell (N=5 networks, r=-0.56, P= 0.06). Error bars indicate s.e.m. (B) The amount of suppression in significantly suppressed cells is plotted against their distance from the stimulated PV cell (left) or SOM cell (right). Best fit lines are shown for each individual network. Networks surrounding stimulated PV neurons could show a positive (blue: r=0.51, P< 0.05), negative (cyan: r=-0.45, P< 0.05; green: r=-0.33, P= 0.14), or flat relationship (red, r=-0.06, P= 0.78) between suppression strength and distance. When all networks were pooled, no relationship between distance and suppression strength was found (r=-0.03, P= 0.80). Similarly, networks surrounding SOM neurons could show a weakly positive (pink: r=0.59, P= 0.41), weakly negative (green: r=-0.61, P= 0.08), or flat relationship (blue: r=-0.04, P= 0.92; red: r=-0.12, P= 0.85; cyan: r=-0.43, P= 0.25). When all SOM networks were pooled, no relationship was seen between suppression strength and distance from the SOM cell (r=-0.28, P= 0.1).

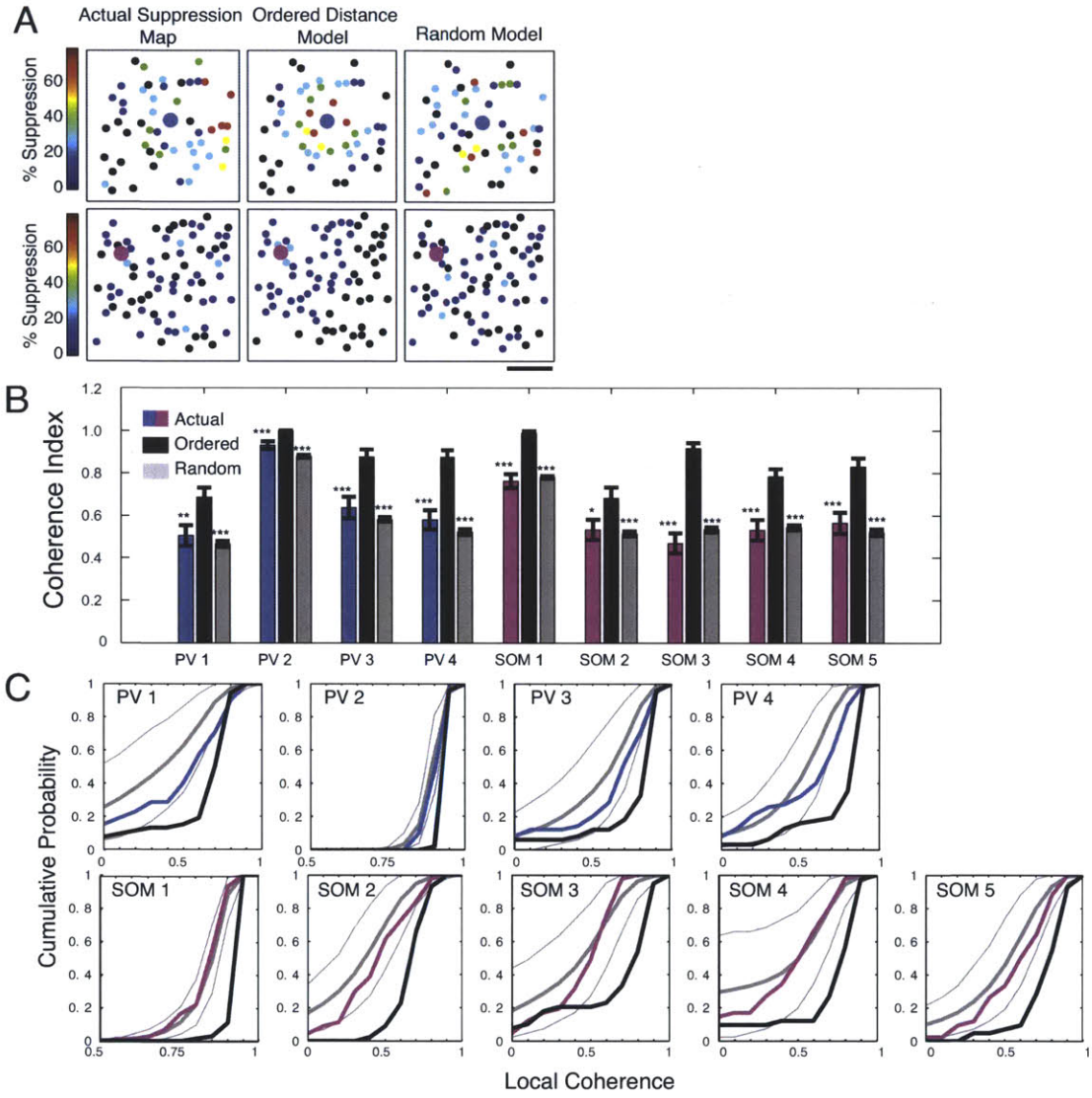

Figure 5.14. A distance model cannot explain the spatial organization of the influence of single PV or SOM cells on local networks. (A) The spatial distribution of suppression by PV (top row) or SOM (bottom row) cells was compared to an ordered distance model, where the original distribution of suppression strengths (left column) was rearranged according to a strict distance function (middle column) or randomly resampled without replacement (right column). Qualitatively, the actual measured suppression maps appeared similar to randomly organized maps. The examples shown are the PV1 and SOM1 networks shown in parts B-C. (B) In order to quantify the apparent differences between the actual suppression maps and ordered suppression maps, we calculated a coherence index for each cell: the distance to the nearest neighboring cell divided by the distance to the nearest cell with a similar level of suppression (within 10%). We then compared the distribution of actual coherence indices for each network to the ordered and random models. All networks examined showed significantly less coherence than ordered networks. (C) Ti further characterize the spatial organization of PV- and SOM-mediated suppression, we calculated the

coherence of suppression surrounding each neuron, which is equal to 1 – the mean difference of suppression strength between each cell and the cells within 40 μm. The cumulative density functions of the actual networks (PV: blue, SOM: pink), the ordered versions of these networks (black), and the random models of these networks (gray, thin lines are the 95% confidence interval boundaries) for all networks examined.

Given previous descriptions that inhibition impinging on cells is iso-oriented with excitation (Anderson et al., 2000; Mariño et al., 2005), or is unturned (Ringach et al., 2003; Xing et al., 2011), we asked whether there was any relationship between the preferred orientation of an inhibitory cell and the preferred orientations of its target neurons. We compared the tuning curves of focally activated PV or SOM neurons and the tuning of significantly suppressed cells (Figure 5.15A). For PV cells and networks (Figure 5.15B, left), the percentage of significantly suppressed cells sharing the preferred orientation (PO) of the source PV cell was significantly greater than the percentage of targeted cells preferring the source PV neuron's non-preferred orientation (nonPO) (Figure 5.15C, top, PO: 44.3±7.6%, nonPO: 20.4±4.8%, $P<0.05$, treating each network as a single observation; $N=210$ target cells from 4 PV networks). This preference toward targeting iso-oriented neurons was not evident when the preferred orientations were randomly resampled among the neurons in the network (Random PO: 35.1±4.0%, Random nonPO: 25.8±6.1%, $P=0.26$). For SOM cells and networks (Figure 5.15B, right), however, the orientation distribution of suppressed cells was more uniform, with no significant difference between the percentage of targeted cells at the preferred vs. non.-preferred orientations of the source SOM cells (Figure 6C, bottom, , PO: 13.5±3.8%, nonPO: 8.1±4.6%, $P=0.39$, treating each network as a single observation; $N=238$ target cells from 5 SOM networks). These results indicate that PV cells preferentially target other neurons that have similar preferred orientations, whereas SOM neurons appear to have a broader range of targets.

5.5 Discussion

In this study, we were able to selectively activate single inhibitory neurons *in vivo* while measuring responses in neighboring neurons with two-photon calcium imaging.

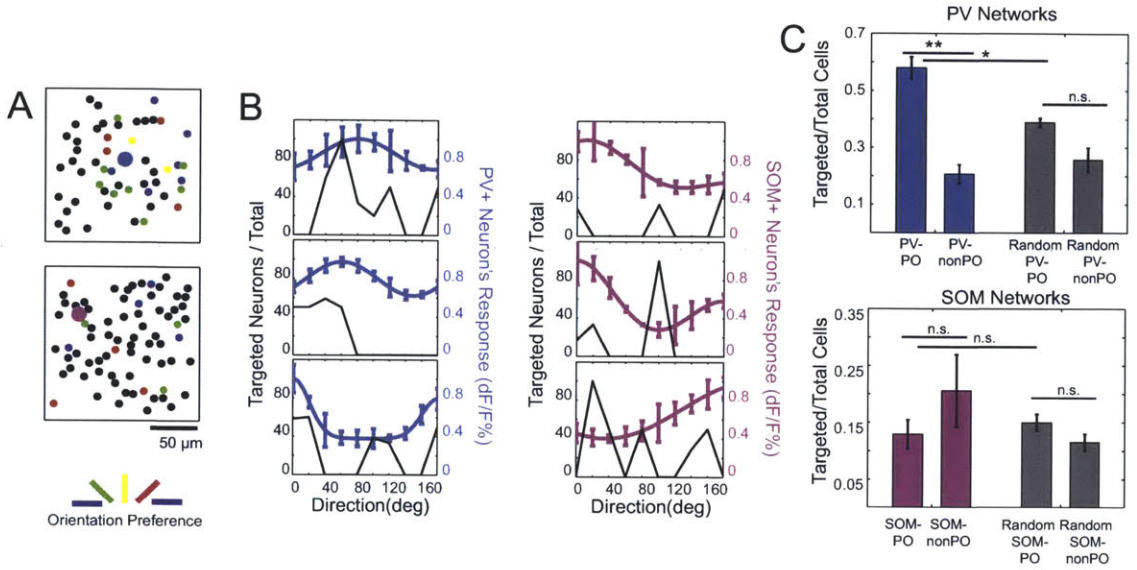

Figure 5.15. The relationship between the orientation preferences of PV and SOM neurons and their targets. (A) The orientation preferences of significantly suppressed cells are color-coded for the same example networks shown in the spatial analyses above. (B) For three example networks where targeted PV cells (left column) or SOM cells (right column) were stimulated, the proportion of neurons in the field of view with each preferred orientation that are significantly suppressed (black lines) are superimposed with the tuning response of the stimulated PV (blue lines) or SOM (pink lines) neurons. (C) Bar graphs show the mean proportion of neurons that matched the preferred orientation of stimulated PV (blue bars) or SOM (pink bars) neurons and the mean proportion of neurons that matched the orientation orthogonal to the preferred orientations of the stimulated inhibitory neurons. PV neurons tended to target a higher proportion of neurons that matched their preferred orientation than orthogonal orientations (paired t-test, $P < 0.05$), while SOM neurons targeted similar proportions ($P = 0.39$). Gray bars show the same comparison when the preferred orientations were randomly resampled among the neurons in the fields of view. In the randomly resampled networks, the difference in targeting of preferred and orthogonal orientations disappears in the PV neurons ($P = 0.26$).

Neither PV+ nor SOM+ inhibitory effects could be predicted by a simple distance function; the map of suppression was significantly less coherent than distance-ordered maps, and quantitatively similar to randomized maps. When we compared the orientation preference of stimulated inhibitory neurons to the preferences of cells that they functionally suppressed, we found that PV+ neurons were more likely to target cells with matching orientation preferences than orthogonal preferences, while SOM+ neurons targeted randomly with respect to orientation preference.

The blue laser spot was capable of highly precise activation of single cells when ChR2 was sparsely expressed across the cortex. We confirmed its specificity by performing cell-attached recordings from ChR2+ neurons and mapping the efficacy of the blue laser in eliciting spikes across the field of view, finding that the spike probability was very high when the spot was focused directly above the soma, but fell sharply as it moved away, even when the cell's processes were strongly expressing the construct (Figure 5.4). Furthermore, when two cells were in the same field of view, activating one cell had no effect on the other, suggesting that activation of inhibitory neurons was not spreading across the inhibitory population through gap junctions (Gibson et al., 1999). However, it is also possible that individual axon terminals could be activated in ChR2+ neurons that were not targeted, whose cell bodies were located outside of the field of view. While our control experiments suggest that such stimulation does not result in backpropagating action potentials, these terminals could have been stimulated to release GABA (or somatostatin) locally (Petreanu et al., 2007), thus inhibiting neurons that were not direct monosynaptic targets of the stimulated PV+ or SOM+ neuron. The sparse functional maps of PV+ and SOM+ cell influence suggest this phenomenon is not widespread with our stimulation protocol, but it must be acknowledged that while we were able to limit the activation of spiking in single cells, we were not necessarily activating only single cells.

Recent studies activating single PV (Packer and Yuste, 2011) and SOM (Fino and Yuste, 2011) neurons while recording IPSPs from pyramidal neurons *in vitro* have suggested that distance is the best predictor of an inhibitory to excitatory connection. At distances less than 50-100μm, the connection probability even approached 100% in these studies. Our results instead suggest that inhibitory neurons inhibit sparsely distributed targets; however, we do not rule out the possibility that these neurons form connections

according to a distance function. Perhaps in many cases these connections are not strong enough or numerous enough to functionally inhibit the target cell during an ongoing computation. The intact cortex processing visual information is in a dramatically different state than an acute slice *in vitro*, and perhaps only the strongest connections are capable of overtly affecting a target neuron's response.

Another recent *in vitro* study (Yoshimura and Callaway, 2005) showed that fast-spiking neurons, probably corresponding to PV+ cells, form specific, reciprocal connections of higher strength with pyramidal neurons with which they share common layer 4 inputs. Adapting inhibitory neurons, which may have primarily included SOM+ neurons, ignored this kind of fine-scale specificity and instead targeted nearby pyramidal neurons promiscuously (Yoshimura and Callaway, 2005). Our findings are in agreement with this distinction in the specificity with which PV and SOM neurons choose their targets; PV neurons preferentially targeted neurons with similar preferred orientations rather than orthogonal ones, while SOM neurons ignored the relative orientation preference of potential targets. These connections, particularly the random-like connections from SOM+ neurons, may not be static. Chronic experiments would allow us to determine the plastic nature of these functional inhibitory connections, and whether the patterns we have discovered are simply snapshots of a malleable inhibitory circuit, or a hard-wired connectome that remains fixed over time. Given the importance of inhibition in developmental experience-dependent plasticity (Hensch, 2005), the former may be a substrate for adult plasticity.

5.6 References

Anderson JS, Carandini M, Ferster D (2000) Orientation tuning of input conductance, excitation, and inhibition in cat primary visual cortex. J Neurophysiol 84:909–926.

Bock DD, Lee W-CA, Kerlin AM, Andermann ML, Hood G, Wetzel AW, Yurgenson S, Soucy ER, Kim HS, Reid RC (2011) Network anatomy and in vivo physiology of visual cortical neurons. Nature 471:177–182.

Dantzker JL, Callaway EM (2000) Laminar sources of synaptic input to cortical inhibitory interneurons and pyramidal neurons. Nature Publishing Group 3:701–707.

DeFelipe J, Fariñas I (1992) The pyramidal neuron of the cerebral cortex: morphological and chemical characteristics of the synaptic inputs. Prog Neurobiol 39:563–607.

Fino E, Yuste R (2011) Dense Inhibitory Connectivity in Neocortex. Neuron 69:1188–1203.
Gentet LJ, Avermann M, Matyas F, Staiger JF, Petersen CCH (2010) Membrane potential dynamics of GABAergic neurons in the barrel cortex of behaving mice. Neuron 65:422–435.
Gibson JR, Beierlein M, Connors BW (1999) Two networks of electrically coupled inhibitory neurons in neocortex. Nature 402:75–79.
Gil Z, Amitai Y (1996) Properties of convergent thalamocortical and intracortical synaptic potentials in single neurons of neocortex. J Neurosci 16:6567–6578.
Hensch TK (2005) Critical period plasticity in local cortical circuits. Nat Rev Neurosci 6:877–888.
Hippenmeyer S, Vrieseling E, Sigrist M, Portmann T, Laengle C, Ladle DR, Arber S (2005) A developmental switch in the response of DRG neurons to ETS transcription factor signaling. PLoS Biol 3:e159.
Hofer SB, Ko H, Pichler B, Vogelstein J, Ros H, Zeng H, Lein E, Lesica NA, Mrsic-Flogel TD (2011) Differential connectivity and response dynamics of excitatory and inhibitory neurons in visual cortex. Nat Neurosci 14:1045–1052.
Inoue T, Imoto K (2006) Feedforward inhibitory connections from multiple thalamic cells to multiple regular-spiking cells in layer 4 of the somatosensory cortex. J Neurophysiol 96:1746–1754.
Mariño J, Schummers J, Lyon DC, Schwabe L, Beck O, Wiesing P, Obermayer K, Sur M (2005) Invariant computations in local cortical networks with balanced excitation and inhibition. Nat Neurosci 8:194–201.
Packer AM, Yuste R (2011) Dense, Unspecific Connectivity of Neocortical Parvalbumin-Positive Interneurons: A Canonical Microcircuit for Inhibition? J Neurosci 31:13260–13271.
Petreanu L, Huber D, Sobczyk A, Svoboda K (2007) Channelrhodopsin-2-assisted circuit mapping of long-range callosal projections. Nature Publishing Group 10:663–668.
Ringach DL, Hawken MJ, Shapley R (2003) Dynamics of orientation tuning in macaque V1: the role of global and tuned suppression. J Neurophysiol 90:342–352.
Sun Q-Q, Huguenard JR, Prince DA (2006) Barrel cortex microcircuits: thalamocortical feedforward inhibition in spiny stellate cells is mediated by a small number of fast-spiking interneurons. J Neurosci 26:1219–1230.
Tamás G, Somogyi P, Buhl EH (1998) Differentially interconnected networks of GABAergic interneurons in the visual cortex of the cat. J Neurosci 18:4255–4270.
Taniguchi H, He M, Wu P, Kim S, Paik R, Sugino K, Kvitsani D, Fu Y, Lu J, Lin Y, Miyoshi G, Shima Y, Fishell G, Nelson SB, Huang ZJ (2011) A Resource of Cre Driver Lines for Genetic Targeting of GABAergic Neurons in Cerebral Cortex. Neuron 71:995–1013.
Xing D, Ringach DL, Hawken MJ, Shapley RM (2011) Untuned suppression makes a major contribution to the enhancement of orientation selectivity in macaque v1. J Neurosci 31:15972–15982.
Yoshimura Y, Callaway EM (2005) Fine-scale specificity of cortical networks depends on inhibitory cell type and connectivity. Nat Neurosci 8:1552–1559.
Yoshimura Y, Dantzker JLM, Callaway EM (2005) Excitatory cortical neurons form fine-scale functional networks. Nature 433:868–873.

Chapter 6: Discussion

This thesis has sought to further our understanding of how distinct inhibitory subtypes contribute to information processing within their local circuits. In the context of visual processing in V1, we asked four major questions: 1) What visual information are inhibitory subtypes carrying, 2) How do they obtain their response properties, 3) How does their activity affect visual processing in target cells, and 4) What are their targets?

6.1 What information are specific inhibitory cell classes carrying?

We found that, on average, parvalbumin-containing (PV+) neurons were broadly tuned for orientation, while somatostatin-containing (SOM+) neurons were very sharply selective for orientation. However, the PV+ population was bimodal; in addition to the large, broadly tuned group it included a smaller highly tuned group (Figure 2.2). Most strikingly, we found that SOM+ neurons had extremely low firing rates, even at the preferred orientation, and responded with a significant delay after the appearance of the visual stimulus, while PV+ neurons responded early in the stimulus presentation. SOM+ neurons were virtually silent when no visual stimulus was present, while PV+ neurons had a significantly higher spontaneous firing rate than other cells (Figure 2.11). Others have found a similar delay and low spontaneous firing rate in the SOM+ visual response in anesthetized mice (Ma et al., 2010).

These differences in the timing of PV+ and SOM+ responses are consistent with the properties of their excitatory synaptic inputs that have been measured *in vitro*. EPSCs in SOM+ neurons tend to have slower dynamics(Dumitriu et al., 2006), and PV+ neurons receive more excitatory inputs (Dumitriu et al., 2006). Though weak, excitatory synapses on SOM+ neurons are strongly facilitating, while synapses on PV+ neurons are depressing (Gupta et al., 2000; Fanselow et al., 2008). Thus SOM+ neurons are spontaneously silent *in vitro*, and require trains of inputs to elicit spikes – single stimulation pulses even of large amplitude cannot produce a spike, but with enough inputs they will fire reliably (Goldberg et al., 2004; Fanselow et al., 2008). Intriguingly, the firing properties of SOM+ neurons

seem different in the awake barrel cortex: instead of only firing weakly and with a delay to stimuli, they fire tonically in the absence of sensory stimuli, and are hyperpolarized by both involuntary and voluntary whisker stimulation (Gentet et al., 2012).

This brain-state-dependent difference in the pattern of activation in SOM+ neurons stresses the importance of studying these cell types in the awake brain. The pattern of activity in PV+ neurons may not be so different between the awake and anesthetized states, because feedforward drive comprises a larger portion of their inputs (Agmon and Connors, 1992; Dantzker and Callaway, 2000; Gonchar and Burkhalter, 2003), while SOM+ neurons are primarily driven by intracortical excitation (Dantzker and Callaway, 2000; Kapfer et al., 2007; Silberberg and Markram, 2007) and are strongly excited by acetylcholine (Fanselow et al., 2008). Therefore, because the successful activation of SOM+ neurons seems to require high firing rates from either top-down or lateral sources, lower cortical firing rates associated with anesthetics could drastically change the timing of these cells' responses with less of an effect on PV+ neurons. Furthermore, fentanyl anesthesia can affect acetylcholine levels, which may have further reduced excitability of SOM+ neurons in our study (Lapchak et al., 1989; Brown et al., 2010). It will be interesting and important to compare PV+ and SOM+ responses and functional impacts across brain states in future studies (Gentet et al., 2010; 2012).

It is also important to note that several recent studies have described the visual response properties of inhibitory neurons. While our study (Runyan et al., 2010) and others (Ma et al., 2010; Hofer et al., 2011; Zariwala et al., 2011) found that inhibitory neurons can be sharply tuned for orientation, some studies described only untuned or very broadly tuned inhibitory neurons (Sohya et al., 2007; Liu et al., 2009a; Kerlin et al., 2010). One possible reason for the discrepancy is the method employed for labeling inhibitory cell types. Studies that have selectively labeled the majority of the PV+ population have recorded highly tuned responses from a subset of these cells (Runyan et al., 2010; Hofer et al., 2011; Zariwala et al., 2011). Perhaps by recording from all PV+ neurons, the distribution of tuning can be more accurately described, and because the highly tuned PV+ cells are more rare than the broadly tuned PV+ cells, they are encountered less frequently. Second, no study using the GAD67-GFP (Δneo) transgene to label inhibitory neurons has reported tuned inhibitory neurons of any type (Sohya et al., 2007; Liu et al., 2009b; Kerlin

et al., 2010). These mice develop with deficient GABA levels (Tamamaki et al., 2003), which affects the development of inhibitory circuitry (Chattopadhyaya et al., 2007), and so perhaps the tuning of inhibitory neurons has not developed normally. Finally, inhibitory neurons express calcium binding proteins that buffer calcium, resulting in blunted calcium-related fluorescent changes. As we have shown (Figure 2.9), highly tuned PV+ neurons have lower firing rates than broadly tuned PV+ neurons, and single spikes in PV+ neurons produce calcium changes that are virtually undetectable with traditional raster scanning methods (Kerlin et al., 2010). Therefore, the highly tuned population of PV+ neurons may have been regarded as not responsive in many calcium imaging studies that used low-frequency raster scanning (1Hz) (Sohya et al., 2007; Kerlin et al., 2010).

6.2 How do inhibitory neurons obtain their response properties?

We initially assumed that in order for PV+ neurons to develop sharp orientation selectivity in the face of a less organized orientation map such as the rodent primary visual cortex, they must specifically sample inputs from neurons with specific preferred orientations, while avoiding nearby neurons with disparate tuning. However, recent studies have suggested that excitatory neurons simply form connections on the nearest inhibitory dendrite/neuron rather than selecting specific targets (Bock et al., 2011; Hofer et al., 2011). We found an unexpected but robust relationship between the selectivity of PV+ neuron responses and their dendritic structure, where highly tuned PV+ neurons had shorter dendrites and broadly tuned PV+ neurons had longer, more tortuous dendrites (Figure 3.3). Furthermore, PV+ neurons tended to match the average tuning of nearby neurons, and their selectivity was correlated to the local coherence of the orientation map – when the local network was more uniformly preferring the same orientation, the PV+ cell had sharper tuning (Figure 3.6). Taken together, these results suggest that inhibitory neurons can obtain higher selectivity by existing in a cluster of neurons with similar orientation selectivity, and also limiting the number of inputs that they sample.

While our results are in agreement with the recent findings on the strict distance-dependence of excitatory-to-inhibitory connection probability (Bock et al., 2011; Hofer et

al., 2011), they do call into question the often-quoted assumption that orientation preferences are uniformly randomly distributed across the mouse visual cortex (Ohki and Reid, 2007). Although well-defined orientation domains such as those present in the carnivore V1 obviously do not exist in the mouse, small local homogeneities may be enough to generate tuning in locally sampling interneurons. Blind electrode experiments have long anecdotally suggested that the organization of mouse V1 orientation preferences is not totally random (Dräger, 1975), and no quantitative study of the organization of orientation preferences at single cell resolution has yet been published, so some functional clustering of orientation preference does seem to be present in the mouse visual cortex.

6.3 How do inhibitory neurons affect sensory processing in their targets?

In order to determine the functional consequences of PV and SOM activity, we selectively stimulated PV+ and SOM+ inhibitory interneurons while measuring the orientation and contrast tuning curves of target cells. We found that, even though PV+ and SOM+ neurons were identically stimulated, their effects on target cells were distinct: PV+ neuron activation divisively normalized responses, while SOM+ neuron activation subtracted responses (Figures 4.3, 4.8). Thus PV+ neurons are capable of controlling response gain, while SOM+ neurons are capable of controlling stimulus-selectivity.

The spatial relationship between excitatory inputs and inhibitory inputs is one critical determining factor in the result of their interaction (Koch et al., 1983), and so an important source of the functional distinction between PV- and SOM-mediated inhibition is the anatomical targeting of their synapses: PV+ neurons target more of their synapses to the perisomatic region, while SOM+ neurons tend to form synapses on distal dendrites (Markram et al., 2004; Burkhalter, 2008). In hippocampal pyramidal neurons, for instance, IPSPs originating in the soma suppress repetitive firing, while dendritic IPSPs suppress the generation of calcium spikes in the dendrites (Miles et al., 1996). Furthermore, when a dendritic IPSP arrives simultaneously with an EPSP, it can offset the excitatory event, preventing it from summating with other EPSPs at the soma (Liu, 2004).

In addition to simple spatial effects of perisomatic vs dendritic inhibition, differences in the distribution of GABA receptor subunits across the pyramidal neuron could have a profound effect on the interaction between excitation and inhibition in a region-specific manner. For instance, $GABA_B$ receptor subunit activation causes K+ ion efflux through G-protein signaling, and thus a slow hyperpolarization of the cell ($E_{K+}\approx$-90mV) (Otis et al., 1993; Kaupmann et al., 1998), and the subcellular localization of these subunits are concentrated in dendrites of hippocampal pyramidal neurons (Kulik et al., 2003; 2006), while $GABA_A$ receptors and their $\alpha 2$ subunits are more concentrated in the perisomatic region (Nusser et al., 1996). However, in the visual cortex, both PV+ and PV- inhibitory axon terminals can be observed at synapses containing $GABA_B$ subunits (Gonchar et al., 2001), so it is unclear whether postsynaptic differences in receptor content could have contributed to the different functional impacts of PV and SOM activation in our study.

Finally, it is also possible that presynaptic differences between the PV+ and SOM+ neurons themselves could contribute to their distinct functional effects on target neurons. The number of synapses formed by each source cell on each target cell, as well as the strength of each synapse could affect the target cell; perisomatic synapses have been observed to have larger active zones with more synaptic vesicles and more mitochondria than inhibitory dendritic synapses (Miles et al., 1996). It is thus possible that the anatomical targeting, postsynaptic receptor aggregation, and presynaptic mechanisms are all important contributors to the functional effects of PV and SOM inhibition.

It is important to acknowledge that in our efforts to determine the impacts of PV+ and SOM+ neurons on their targets, we have artificially activated them identically. We forced both cell types to respond strongly to all orientations, and timed their responses with the appearance of visual stimuli. As demonstrated in Chapter 2 of this thesis, many PV+ and SOM+ neurons do not respond in this manner: PV+ neurons can be sharply tuned to respond to only specific orientations, and most SOM+ neurons have sharply tuned yet delayed responses. Our stimulation paradigm allowed us to determine the functional impacts when these cells do fire – and by activating both cell types identically, we could directly compare their effects. In future studies it will be imperative to suppress firing in SOM+ and PV+ neurons and therefore determine how they normally affect responses in

their targets. Suppression of PV+ and SOM+ neurons will have complicated effects on target responses, that depend on the tuning of the PV+ and SOM+ cells providing inhibition. Computational modeling studies, or even further experiments where PV+ and SOM+ neurons are activated in the ways compatible with our measurements in Chapter 2 – broadly tuned or sharply tuned PV+ neuron activation and sharply tuned and delayed SOM+ neuron activation - could further enhance our understanding of the functional impacts these cells have on target neuron responses.

Importantly, we have measured the effects of PV and SOM stimulation on real-time visual computations; however, these cell types are also likely to play distinct roles in plasticity. A major effect of dendritic inhibition is to limit the back-propagation of action potentials from the soma through the dendritic tree (Tsubokawa and Ross, 1996). If SOM+ neurons tend to be delayed in their responses to sensory stimuli (Figure 2.11, (Ma et al., 2010; but see Gentet et al., 2012), the regulation of synaptic plasticity could be one of their major roles. Furthermore, we have measured the impacts that PV+ and SOM+ neurons have when they are active – but as our measurements of PV+ and SOM+ neuron response properties show, the timing of PV+ and SOM+ neuron responses can differ (Chapter 2). Our work is an important step in determining what effects these cells can have on their targets, but optogenetic inactivation of PV+ and SOM+ neurons in future experiments will demonstrate what impacts these cell types do have on sensory processing in normal conditions.

6.4 Functional connectomics: What are the target cells of PV+ and SOM+ neurons?

We stimulated single PV+ and SOM+ neurons while monitoring the visual responses of neighboring neurons with calcium imaging in order to map the functional effects of single inhibitory neurons. We found that single inhibitory neurons of either cell class can have measurable effects on the visual responses of cells in the local network (Figures 5.7, 5.8), but that distance from the stimulated source cell could not predict whether a neuron would be functionally suppressed (Figures 5.13, 5.14). PV+ neurons tended to suppress

more neurons with similar orientation preferences, while SOM+ neurons did not show such a bias (Figure 5.15).

These results agree with a study that compared the inputs of unconnected and reciprocally connected fast-spiking neurons (FS, likely to be PV+) and pyramidal neurons in layers 2/3, which found that the amplitudes of IPSPs between reciprocally connected pairs were higher, and reciprocally connected pairs tended to share common excitatory inputs (Yoshimura and Callaway, 2005). Neurons that share the same excitatory inputs in visual cortex would be expected to have similar orientation preferences, as we have found that PV+ neurons and their functional targets often do (Figure 5.15). In the same study, it was found that adapting inhibitory neurons, likely to be SOM+, do not share excitatory inputs with their targets (Yoshimura and Callaway, 2005); indeed, we found that SOM+ neurons and their targets are less likely to share the same orientation preference than PV+ neurons and their targets (Figure 5.15).

Our results do not necessarily contradict recent work that showed PV+ and SOM+ neurons blanket the local network with nonspecific inhibition that simply decreases in probability with distance (Fino and Yuste, 2011; Packer and Yuste, 2011). First, these studies did not examine the distance-function of IPSP amplitude; it is possible that inhibitory neurons do in fact connect to all neurons according to a distance function but show specificity in the number of synaptic contacts or the synaptic strength on certain targets, as FS neurons do with reciprocally connected pyramidal neurons (Yoshimura and Callaway, 2005). We measured functional suppression of visual responses; it is possible that a single inhibitory synapse would not be able to suppress such activity, while such a connection would be detectable as a single IPSP in a whole-cell patch clamp recording *in vitro*. Perhaps such weak connections provide a scaffold on which inhibition can build, playing a role in plasticity.

6.5 Conclusion

It is convenient and tractable to consider two major classes of inhibitory interneurons – those that express the calcium binding protein parvalbumin (PV) and those that do not – rather than considering the ten, 30, or even 100 subgroups defined across molecular, physiological, and morphological dimensions (Markram et al., 2004; Krimer et al., 2005; Burkhalter, 2008; Helmstaedter et al., 2009). This clean molecular definition divides inhibitory neurons down the middle – roughly half of cortical inhibitory cells express PV, depending on the layer (Kubota et al., 1994; Kawaguchi and Kubota, 1997; Gonchar et al., 2007). Furthermore, these two classes correspond more or less with other important definitions of inhibitory cell types – fast-spiking vs. non-fast-spiking, and perisomatic-targeting vs. dendrite-targeting.

Indeed, when we selectively activated PV+ neurons and SOM+ neurons (a subgroup of the PV- inhibitory class, (Kubota et al., 1994; Kawaguchi and Kondo, 2002; Xu et al., 2010)), we found a distinction in their functional impacts on target cells: PV+ neurons control response gain, while SOM+ neurons control stimulus selectivity. However, our measurements of the response properties of PV+ and SOM+ inhibitory interneurons in the first chapter of this thesis highlighted the diversity within each of these two populations. Even within the PV+ population, there is remarkable diversity in the response timing, selectivity, and morphology of these cells. Going forward, it will be a challenge to refrain from oversimplifying the characteristics and functions of inhibitory subclasses, yet to also limit the ever-refined splitting of inhibitory cell classes that may limit our capacity to understand general principles of brain circuits.

6.6 References

Agmon A, Connors BW (1992) Correlation between intrinsic firing patterns and thalamocortical synaptic responses of neurons in mouse barrel cortex. J Neurosci 12:319–329.

Bock DD, Lee W-CA, Kerlin AM, Andermann ML, Hood G, Wetzel AW, Yurgenson S, Soucy ER, Kim HS, Reid RC (2011) Network anatomy and in vivo physiology of visual cortical neurons. Nature 471:177–182.

Brown EN, Lydic R, Schiff ND (2010) General anesthesia, sleep, and coma. N Engl J Med

363:2638–2650.
Burkhalter A (2008) Many specialists for suppressing cortical excitation. Front Neurosci 2:155–167.
Chattopadhyaya B, Di Cristo G, Wu CZ, Knott G, Kuhlman S, Fu Y, Palmiter RD, Huang ZJ (2007) GAD67-mediated GABA synthesis and signaling regulate inhibitory synaptic innervation in the visual cortex. Neuron 54:889–903.
Dantzker JL, Callaway EM (2000) Laminar sources of synaptic input to cortical inhibitory interneurons and pyramidal neurons. Nature Publishing Group 3:701–707.
Dräger UC (1975) Receptive fields of single cells and topography in mouse visual cortex. J Comp Neurol 160:269–290.
Dumitriu D, Cossart R, Huang J, Yuste R (2006) Correlation Between Axonal Morphologies and Synaptic Input Kinetics of Interneurons from Mouse Visual Cortex. Cerebral Cortex 17:81–91.
Fanselow EE, Richardson KA, Connors BW (2008) Selective, state-dependent activation of somatostatin-expressing inhibitory interneurons in mouse neocortex. J Neurophysiol 100:2640–2652.
Fino E, Yuste R (2011) Dense Inhibitory Connectivity in Neocortex. Neuron 69:1188–1203.
Gentet LJ, Avermann M, Matyas F, Staiger JF, Petersen CCH (2010) Membrane potential dynamics of GABAergic neurons in the barrel cortex of behaving mice. Neuron 65:422–435.
Gentet LJ, Kremer Y, Taniguchi H, Huang ZJ, Staiger JF, Petersen CCH (2012) Unique functional properties of somatostatin-expressing GABAergic neurons in mouse barrel cortex. Nat Neurosci.
Goldberg JH, Lacefield CO, Yuste R (2004) Global dendritic calcium spikes in mouse layer 5 low threshold spiking interneurones: implications for control of pyramidal cell bursting. J Physiol (Lond) 558:465–478.
Gonchar Y, Burkhalter A (2003) Distinct GABAergic targets of feedforward and feedback connections between lower and higher areas of rat visual cortex. J Neurosci 23:10904–10912.
Gonchar Y, Pang L, Malitschek B, Bettler B, Burkhalter A (2001) Subcellular localization of GABA(B) receptor subunits in rat visual cortex. J Comp Neurol 431:182–197.
Gonchar Y, Wang Q, Burkhalter A (2007) Multiple distinct subtypes of GABAergic neurons in mouse visual cortex identified by triple immunostaining. Frontiers in neuroanatomy 1:3.
Gupta A, Wang Y, Markram H (2000) Organizing principles for a diversity of GABAergic interneurons and synapses in the neocortex. Science 287:273–278.
Helmstaedter M, Sakmann B, Feldmeyer D (2009) L2/3 interneuron groups defined by multiparameter analysis of axonal projection, dendritic geometry, and electrical excitability. Cereb Cortex 19:951–962.
Hofer SB, Ko H, Pichler B, Vogelstein J, Ros H, Zeng H, Lein E, Lesica NA, Mrsic-Flogel TD (2011) Differential connectivity and response dynamics of excitatory and inhibitory neurons in visual cortex. Nat Neurosci 14:1045–1052.
Kapfer C, Glickfeld LL, Atallah BV, Scanziani M (2007) Supralinear increase of recurrent inhibition during sparse activity in the somatosensory cortex. Nature Publishing Group 10:743–753.
Kaupmann K, Schuler V, Mosbacher J, Bischoff S, Bittiger H, Heid J, Froestl W, Leonhard S,

Pfaff T, Karschin A, Bettler B (1998) Human gamma-aminobutyric acid type B receptors are differentially expressed and regulate inwardly rectifying K+ channels. Proc Natl Acad Sci USA 95:14991–14996.
Kawaguchi Y, Kondo S (2002) Parvalbumin, somatostatin and cholecystokinin as chemical markers for specific GABAergic interneuron types in the rat frontal cortex. J Neurocytol 31:277–287.
Kawaguchi Y, Kubota Y (1997) GABAergic cell subtypes and their synaptic connections in rat frontal cortex. Cereb Cortex 7:476–486.
Kerlin AM, Andermann ML, Berezovskii VK, Reid RC (2010) Broadly tuned response properties of diverse inhibitory neuron subtypes in mouse visual cortex. Neuron 67:858–871.
Koch C, Poggio T, Torre V (1983) Nonlinear interactions in a dendritic tree: localization, timing, and role in information processing. Proc Natl Acad Sci USA 80:2799–2802.
Krimer LS, Zaitsev AV, Czanner G, Kröner S, González-Burgos G, Povysheva NV, Iyengar S, Barrionuevo G, Lewis DA (2005) Cluster analysis-based physiological classification and morphological properties of inhibitory neurons in layers 2-3 of monkey dorsolateral prefrontal cortex. J Neurophysiol 94:3009–3022.
Kubota Y, Hattori R, Yui Y (1994) Three distinct subpopulations of GABAergic neurons in rat frontal agranular cortex. Brain Res 649:159–173.
Kulik A, Vida I, Fukazawa Y, Guetg N, Kasugai Y, Marker CL, Rigato F, Bettler B, Wickman K, Frotscher M, Shigemoto R (2006) Compartment-dependent colocalization of Kir3.2-containing K+ channels and GABAB receptors in hippocampal pyramidal cells. J Neurosci 26:4289–4297.
Kulik A, Vida I, Luján R, Haas CA, López-Bendito G, Shigemoto R, Frotscher M (2003) Subcellular localization of metabotropic GABA(B) receptor subunits GABA(B1a/b) and GABA(B2) in the rat hippocampus. J Neurosci 23:11026–11035.
Lapchak PA, Araujo DM, Collier B (1989) Regulation of endogenous acetylcholine release from mammalian brain slices by opiate receptors: hippocampus, striatum and cerebral cortex of guinea-pig and rat. Neuroscience 31:313–325.
Liu B-H, Li P, Li Y-T, Sun YJ, Yanagawa Y, Obata K, Zhang LI, Tao HW (2009a) Visual receptive field structure of cortical inhibitory neurons revealed by two-photon imaging guided recording. J Neurosci 29:10520–10532.
Liu B-H, Li P, Li Y-T, Sun YJ, Yanagawa Y, Obata K, Zhang LI, Tao HW (2009b) Visual receptive field structure of cortical inhibitory neurons revealed by two-photon imaging guided recording. J Neurosci 29:10520–10532.
Liu G (2004) Local structural balance and functional interaction of excitatory and inhibitory synapses in hippocampal dendrites. Nature Publishing Group 7:373–379.
Ma W-P, Liu B-H, Li Y-T, Huang ZJ, Zhang LI, Tao HW (2010) Visual representations by cortical somatostatin inhibitory neurons--selective but with weak and delayed responses. J Neurosci 30:14371–14379.
Markram H, Toledo-Rodriguez M, Wang Y, Gupta A, Silberberg G, Wu C (2004) Interneurons of the neocortical inhibitory system. Nat Rev Neurosci 5:793–807.
Miles R, Tóth K, Gulyás AI, Hájos N, Freund TF (1996) Differences between somatic and dendritic inhibition in the hippocampus. Neuron 16:815–823.
Nusser Z, Sieghart W, Benke D, Fritschy JM, Somogyi P (1996) Differential synaptic localization of two major gamma-aminobutyric acid type A receptor alpha subunits on

hippocampal pyramidal cells. Proc Natl Acad Sci USA 93:11939–11944.
Ohki K, Reid RC (2007) Specificity and randomness in the visual cortex. Curr Opin Neurobiol 17:401–407.
Otis TS, De Koninck Y, Mody I (1993) Characterization of synaptically elicited GABAB responses using patch-clamp recordings in rat hippocampal slices. J Physiol (Lond) 463:391–407.
Packer AM, Yuste R (2011) Dense, Unspecific Connectivity of Neocortical Parvalbumin-Positive Interneurons: A Canonical Microcircuit for Inhibition? J Neurosci 31:13260–13271.
Runyan CA, Schummers J, Van Wart A, Kuhlman SJ, Wilson NR, Huang ZJ, Sur M (2010) Response features of parvalbumin-expressing interneurons suggest precise roles for subtypes of inhibition in visual cortex. Neuron 67:847–857.
Silberberg G, Markram H (2007) Disynaptic inhibition between neocortical pyramidal cells mediated by Martinotti cells. Neuron 53:735–746.
Sohya K, Kameyama K, Yanagawa Y, Obata K, Tsumoto T (2007) GABAergic neurons are less selective to stimulus orientation than excitatory neurons in layer II/III of visual cortex, as revealed by in vivo functional Ca2+ imaging in transgenic mice. J Neurosci 27:2145–2149.
Tamamaki N, Yanagawa Y, Tomioka R, Miyazaki J-I, Obata K, Kaneko T (2003) Green fluorescent protein expression and colocalization with calretinin, parvalbumin, and somatostatin in the GAD67-GFP knock-in mouse. J Comp Neurol 467:60–79.
Tsubokawa H, Ross WN (1996) IPSPs modulate spike backpropagation and associated [Ca2+]i changes in the dendrites of hippocampal CA1 pyramidal neurons. J Neurophysiol 76:2896–2906.
Xu X, Roby KD, Callaway EM (2010) Immunochemical characterization of inhibitory mouse cortical neurons: three chemically distinct classes of inhibitory cells. J Comp Neurol 518:389–404.
Yoshimura Y, Callaway EM (2005) Fine-scale specificity of cortical networks depends on inhibitory cell type and connectivity. Nat Neurosci 8:1552–1559.
Zariwala HA, Madisen L, Ahrens KF, Bernard A, Lein ES, Jones AR, Zeng H (2011) Visual Tuning Properties of Genetically Identified Layer 2/3 Neuronal Types in the Primary Visual Cortex of Cre-Transgenic Mice. Front Syst Neurosci 4:1–16.